

Topical Review

# Experimental progress in $\text{Eu}(\text{Al,Ga})_4$ topological antiferromagnets

Tian Shang<sup>1,\*</sup>, Yang Xu<sup>1</sup>, Shang Gao<sup>2</sup>, Run Yang<sup>3</sup>, Toni Shiroka<sup>4,5</sup>, Ming Shi<sup>6</sup>

<sup>1</sup>Key Laboratory of Polar Materials and Devices (MOE), School of Physics and Electronic Science, East China Normal University, Shanghai 200241, China

<sup>2</sup>Department of Physics, University of Science and Technology of China, Hefei 230026, China

<sup>3</sup>Key Laboratory of Quantum Materials and Devices of Ministry of Education, School of Physics, Southeast University, Nanjing 211189, China

<sup>4</sup>Laboratory for Muon-Spin Spectroscopy, Paul Scherrer Institut, Villigen PSI, Switzerland

<sup>5</sup>Laboratorium für Festkörperphysik, ETH Zürich, CH-8093 Zürich, Switzerland

<sup>6</sup>Center for Correlated Matter and School of Physics, Zhejiang University, Hangzhou 310058, China

E-mail: tshang@phy.ecnu.edu.cn

**Abstract.** The non-trivial magnetic and electronic phases occurring in topological magnets are often entangled, thus leading to a variety of exotic physical properties. Recently, the  $\text{BaAl}_4$ -type compounds have been extensively investigated to elucidate the topological features appearing in their real- and momentum spaces. In particular, the topological Hall effect and the spin textures, typical of the centrosymmetric  $\text{Eu}(\text{Al,Ga})_4$  family, have stimulated extensive experimental and theoretical research. In this topical review, we discuss the latest findings regarding the  $\text{Eu}(\text{Al,Ga})_4$  topological antiferromagnets and related materials, arising from a vast array of experimental techniques. We show that  $\text{Eu}(\text{Al,Ga})_4$  represents a suitable platform to explore the interplay between lattice-, charge-, and spin degrees of freedom, and associated emergent phenomena. Finally, we address some key questions open to future investigation.

**Keywords:** topological Hall effect, topological spin textures, magnetic skyrmions, Weyl semimetal, antiferromagnet, charge density wave, spin density wave

Submitted to: *J. Phys.: Condens. Matter*

## 1. Introduction

In recent years, the topologically non-trivial magnetic and electronic structures have attracted an extraordinary attention [1–3]. Introducing magnetic order into topological materials promotes exotic topological phases. Unlike ferromagnets, the antiferromagnets offer far more interesting cases of magnetic topological band structures. These arise from the enormous number of possible spin configurations and provide several interesting situations and, in principle, unforeseen properties [4, 5].

Weyl semimetals represent one of the most interesting subclasses of topological materials. They are characterized by linearly dispersed electronic bands and often exhibit large Berry curvatures near the Fermi surface [6–8]. The Weyl-semimetal phase emerges only upon breaking the space inversion- or the time-reversal symmetry, the latter being realized either by applying an external magnetic field, or via intrinsic magnetic order or fluctuations [6–10]. In the magnetic topological materials, the non-trivial magnetic and electronic structures are strongly coupled, leading to a variety of exotic physical properties, such as the topological Hall effect (THE) or the anomalous Hall effect (AHE) [11–15], both suitable for spintronic or quantum devices [16, 17]. Due to their entanglement, the Weyl nodes and the associated Berry curvature can be effectively tuned by various external parameters, as e.g., the magnetic field [18, 19], chemical substitution [20], physical pressure [21, 22], or epitaxial strain [23].

Topologically non-trivial spin textures are very promising for the next generation of logic and memory devices [17, 24, 25]. Among the non-trivial spin textures, the magnetic skyrmions are the most renowned ones [26–39]. Yet, other types of spin textures have also been discovered or proposed [40], as e.g., hedgehogs [20, 41], hopfions [42], merons [18], and magnetic bubbles [43]. Magnetic skyrmions are chiral spin structures with a whirling configuration, typically in the nanoscale range. As topologically protected phases, they cannot be continuously deformed into other magnetic states. This robustness against external perturbations makes them perfect for spintronic devices [17, 24, 25]. In general, all these non-trivial spin textures can be stabilized by the Dzyaloshinskii-Moriya interactions (DMIs), often observed at the interfaces of thin films or in materials that lack an inversion symmetry [27–31, 44]. Conversely, magnetic materials with a centrosymmetric crystal structure that still can host magnetic skyrmions are rare. To date, only a few of such systems have been reported,

including  $\text{Gd}_2\text{PdSi}_3$  [32],  $\text{Gd}_3\text{Ru}_4\text{Al}_{12}$  [33],  $\text{GdRu}_2\text{Si}_2$  [34],  $\text{Fe}_3\text{Sn}_2$  [35],  $\text{EuCd}_2\text{As}_2$  [11, 45],  $\text{Mn}_4\text{Ga}_2\text{Sn}$  [46], and, very recently,  $\text{EuAl}_4$  [47, 48]. The last compound, belonging to the  $\text{BaAl}_4$  class, represents the topic of this review.

In centrosymmetric systems, skyrmions can be stabilized, for instance, by magnetic frustration (e.g., in  $\text{Gd}_3\text{Ru}_4\text{Al}_{12}$ ,  $\text{Gd}_2\text{PdSi}_3$ , and  $\text{Fe}_3\text{Sn}_2$ ) [33–36], or by the competition between the magnetic interactions and magnetic anisotropy (e.g., in  $\text{GdRu}_2\text{Si}_2$ ) [34]. Despite adopting the same crystal structure as  $\text{GdRu}_2\text{Si}_2$ , the magnetic anisotropy of  $\text{EuAl}_4$  is only moderate. Consequently, in  $\text{EuAl}_4$ , skyrmions should be stabilized by other mechanisms. For instance, the magnetic dipolar interactions were found to play a significant role in the formation of magnetic skyrmions in  $\text{Gd}_2\text{PdSi}_3$  [49]. In addition, a four-spin interaction, mediated by itinerant electrons, has been proposed as an important ingredient for the formation of skyrmions in centrosymmetric materials [36–38]. Not long ago, the chiral magnet  $\text{Co}_7\text{Zn}_7\text{Mn}_6$  was found to host a skyrmion phase far below the magnetic ordering temperature, where spin fluctuations are believed to be the key for stabilizing the magnetic skyrmions [39].  $\text{EuAl}_4$  also exhibits robust spin fluctuations against external magnetic field, which analogously might be crucial for the occurrence of the topological Hall effect and of possible skyrmions in it [50]. Compared to noncentrosymmetric systems, in centrosymmetric materials skyrmions exhibit the unique advantages of a tunable size and of spin helicity [51]. Nevertheless, the above mechanisms cannot account for all the cases where skyrmions are observed in centrosymmetric materials. Hence, their origin is not yet fully understood and requires further investigation.

In recent years, the Hall effect has become one of the most used methods to investigate magnetic materials. In general, the Hall effect involves the deflection of charge-carrier trajectories by the Lorentz force. In addition to an external magnetic field (the origin of the classical Hall effect), other sources can also act as an effective field, typically associated with a non-zero Berry curvature. In magnetic materials, the Hall resistivity  $\rho_{xy}$  can be expressed as  $\rho_{xy} = \rho_{xy}^{\text{O}} + \rho_{xy}^{\text{A}}$ , where  $\rho_{xy}^{\text{O}}$  and  $\rho_{xy}^{\text{A}}$  represent the ordinary- and the anomalous Hall resistivity, respectively. Usually, the AHE is observed in magnetic materials with a finite magnetization, such as ferro- or ferrimagnets. Here, it is due to an intrinsic Karplus-Luttinger mechanism, or to extrinsic mechanisms as the skew scattering and side jump [16]. In materials with Dirac- or Weyl points near the Fermi surface, a finite

$\rho_{xy}^A$  might arise from topologically non-trivial momentum-space features, a possibility attracting an intense research interest [11, 12, 14, 52–55]. For instance, the noncollinear antiferromagnets  $\text{Mn}_3\text{Sn}$ ,  $\text{Mn}_3\text{Ge}$ , and  $\text{Mn}_3\text{Ir}$  [13, 14, 56, 57], the nonmagnetic- TaAs, TaP and NbP [58, 59] and the magnetic GdPtBi Weyl semimetals [12], as well as the  $\text{Cd}_3\text{As}_2$  and  $\text{ZrTe}_5$  Dirac semimetals [53–55], all exhibit  $\rho_{xy}^A$  in a wide range of temperatures and magnetic fields. Very recently, the AHE has been theoretically proposed and experimentally observed in a new type of magnetic materials, namely, the altermagnets [60–63].

The  $\rho_{xy}^A$  term can be further split into two sub-terms (owing to their different origins),  $\rho_{xy} = \rho_{xy}^O + \rho_{xy}^{\text{AHE}} + \rho_{xy}^{\text{THE}}$ . Here,  $\rho_{xy}^{\text{AHE}}$  represents the *conventional* anomalous Hall term, mostly determined by the electrical resistivity and magnetization. The last term represents the *topology-* (THE) induced contribution. The topological Hall effect has been frequently used to search for and study the chiral spin textures in various materials. As opposed to the intrinsic AHE, which depends on the Berry curvature in *momentum* space, the THE is related to a Berry-phase accumulation in *real* space due to chiral spin textures [25]. When passing through chiral spin textures, such as skyrmions, charge carriers pick up an additional Berry phase and experience a local emergent magnetic field  $B_{\text{eff}}$ . The latter is proportional to the scalar spin chirality  $\chi_{ijk} = \mathbf{S}_i \cdot (\mathbf{S}_j \times \mathbf{S}_k)$ , with  $\chi_{ijk}$  the solid angle spanned by neighboring spins  $S_i$ ,  $S_j$ , and  $S_k$ , which becomes non-zero for non-coplanar spin textures. The transverse deflection of charge carriers interacting with  $B_{\text{eff}}$  results in the topological Hall resistivity  $\rho_{xy}^{\text{THE}}$ , whose amplitude is given by  $\rho_{xy}^{\text{THE}} = P \cdot R_0 \cdot (n_{\text{sk}} \cdot \Phi_0)$  [64, 65]. Here,  $P$  is the spin polarization of charge carriers,  $R_0$  is the Hall coefficient representing the effective charge density contributing to the THE (usually taken as the classical Hall coefficient),  $B_{\text{eff}} = n_{\text{sk}} \cdot \Phi_0$  is the emergent field associated with a given skyrmion density  $n_{\text{sk}}$ , and  $\Phi_0$  is the magnetic flux quantum.

Many other techniques have been successfully used to visualize and study the chiral spin textures, e.g., neutron scattering [31, 44, 48], magnetic resonant elastic x-ray scattering [32], magnetic force microscopy [65], magnetic exchange force microscopy [66], magnetic transmission x-ray microscopy [67, 68], Lorentz transmission electron microscopy [28, 46], spin-polarized low-energy electron microscopy [69], and scanning tunneling microscopy [70]. Even though such techniques can probe the topological spin textures, they cannot be used as information-reading tools in real devices. By contrast, the plain detection of THE is simple and can be easily realized in real applications, with big advantages compared to the large-scale or microscopic techniques. Unfortunately, most magnetic materials with chiral spin textures exhibit only weak topological transport signals, i.e.,  $\rho_{xy}^{\text{THE}} \lesssim 1 \mu\Omega\text{cm}$ . Clearly,

increasing the magnitude of  $\rho_{xy}^{\text{THE}}$  remains the key to viable topological spintronic devices and the most important challenge so far.

Exploring new magnetic skyrmion materials, especially those with a centrosymmetric crystal structure, is a hot topic which drives the ongoing research on topological spintronic devices. The discovery of a non-trivial band topology and large magnetoresistance (MR) in the prototype compound  $\text{BaAl}_4$  [71], as well as of THE in its magnetic counterpart  $\text{EuAl}_4$  [47], have stimulated intense interest in this family of materials. The  $\text{AAl}_4$  and  $\text{AGa}_4$  ( $A = \text{Ca}, \text{Sr}, \text{Ba},$  and  $\text{Eu}$ ) binary compounds exhibit a variety of physical properties, attributed to the presence of structural-, charge-, and magnetic order phase transitions. Similar to  $\text{BaAl}_4$ , also  $\text{BaGa}_4$  exhibits metallic behavior without undergoing any phase transitions, while  $\text{SrAl}_4$  shows a charge-density-wave (CDW) and a structural phase transition at  $T_{\text{CDW}} \sim 250 \text{ K}$  and  $T_S \sim 90 \text{ K}$ , respectively [72]. Both compounds are also expected to exhibit topological features, requiring further investigations. By replacing Ba (or Sr) with Eu, the  $4f$  electrons bring new intriguing aspects to the topology, as clearly illustrated by recent work on  $\text{EuAl}_4$  and  $\text{EuGa}_4$  [47, 48, 73].  $\text{EuAl}_4$  exhibits coexisting antiferromagnetic- (AFM) and CDW orders with onset temperatures  $T_N \sim 15.6 \text{ K}$  and  $T_{\text{CDW}} \sim 140 \text{ K}$  [47, 74–78] and undergoes a series of metamagnetic transitions in the AFM state [47, 76]. Topological Hall resistivity was observed in the  $\sim 1$ – $2.5 \text{ T}$  field range [47] and attributed to the formation of magnetic skyrmions [48]. Hence,  $\text{EuAl}_4$  represents a rare case, where magnetic skyrmions not only arise in a centrosymmetric structure, but also coexist with CDW order.  $\text{EuGa}_4$  is also an antiferromagnet (with  $T_N \sim 16.5 \text{ K}$ ), whose CDW order appears only under applied pressure (close to  $0.75 \text{ GPa}$ ), with  $T_{\text{CDW}}$  reaching  $\sim 175 \text{ K}$  at  $2.3 \text{ GPa}$  [75, 76, 79]. It also exhibits THE in the  $\sim 5$ – $7 \text{ T}$  field range in the AFM state, most likely also related to topological spin textures (awaiting experimental confirmation). Recently,  $\text{EuGa}_4$  was confirmed to be a magnetic Weyl nodal-ring semimetal, where the line nodes form closed rings near the Fermi level [73].

$\text{Eu}(\text{Al},\text{Ga})_4$  antiferromagnets represent one of the rare material classes to exhibit exotic physical properties originating from topological aspects in both the real- and momentum space. This topical review focuses mostly on recent experimental investigations of the  $\text{Eu}(\text{Al},\text{Ga})_4$  topological antiferromagnets and related materials. After this short introduction, in section 2, we briefly discuss the crystal structures and CDW order (including its possible mechanisms) in the  $\text{A}(\text{Al},\text{Ga})_4$  family of materials. Section 3 describes the magnetic and transport properties of  $\text{Eu}(\text{Al},\text{Ga})_4$  single crystals and the resulting magnetic phase diagrams. The topological Hall effect is also discussed in this section. In section 4, we summarize the neutron and synchrotron resonant x-ray scattering (RXS) results, aimed at determining the magnetic structures

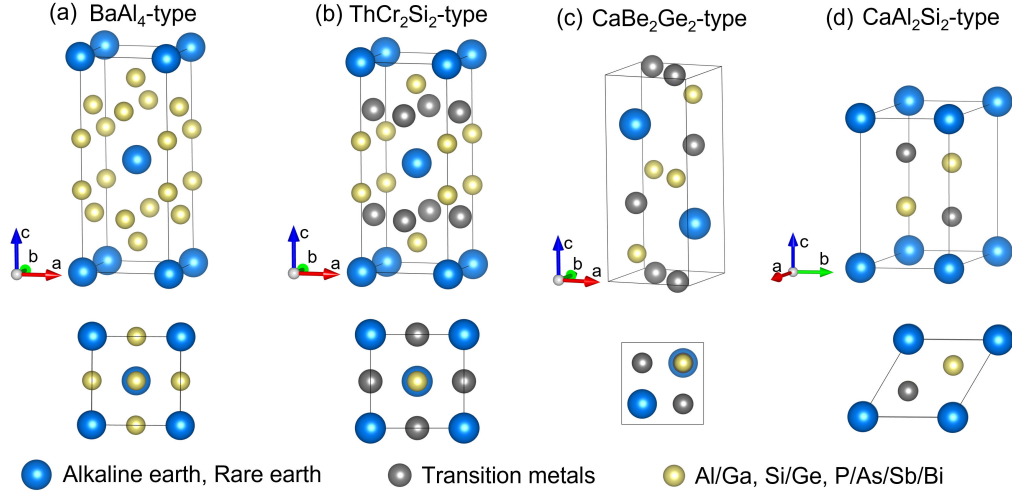


**Figure 1.** Summary of crystal structures related to the alkaline-earth and rare-earth-based  $AT_2X_2$  materials: (a)  $\text{BaAl}_4$ -type, (b)  $\text{ThCr}_2\text{Si}_2$ -type, (c)  $\text{CaBe}_2\text{Ge}_2$ -type, and (d)  $\text{CaAl}_2\text{Si}_2$ -type structure. At the bottom of each panel, we depict the crystal structures viewed along the  $c$ -axis. The coordinates of atoms in each crystal structure are listed in table 1.

in the AFM state, in particular, of magnetic skyrmions in  $\text{EuAl}_4$ . In section 5, we focus on the muon-spin rotation and relaxation ( $\mu\text{SR}$ ) study, in both the AFM and paramagnetic (PM) states of  $\text{Eu}(\text{Al},\text{Ga})_4$  single crystals, where strong and robust spin fluctuations have been found. In section 6, we review the current nuclear magnetic resonance (NMR) studies, able to detect both the magnetic and charge order. In the following section 7, the magneto-optical spectroscopy studies on  $\text{Eu}(\text{Al},\text{Ga})_4$  single crystals are discussed, to show the effects induced by CDW order. Before the final section, we discuss the electronic band topology investigated by the angle-resolved photoemission spectroscopy (ARPES) and quantum oscillations (QO). Finally, we conclude by outlining some possible future directions in this interesting field of research.

## 2. Crystal structure and charge-density-wave order

### 2.1. Crystal structure

There are mainly four different crystal structures that are related to the compounds with  $AT_2X_2$  stoichiometry. These structures exhibit pronounced chemical flexibility, the  $A$  site can be occupied by alkali metals, alkaline earth and rare-earth metals, first-column transition metals, actinide elements (e.g., U, Th, Pu); the  $T$  site can be occupied mostly by transition metals and  $p$ -block elements; and the  $X$  site can be occupied by  $p$ -block elements and some transition metals. In general, the  $AT_2X_2$  compounds adopt mainly four different crystal structures (see figure 1). The  $\text{BaAl}_4$ -,  $\text{ThCr}_2\text{Si}_2$ -, and  $\text{CaBe}_2\text{Ge}_2$ -type crystal structures are tetragonal, while the  $\text{CaAl}_2\text{Si}_2$ -type structure is trigonal. The  $\text{BaAl}_4$ - and  $\text{ThCr}_2\text{Si}_2$ -type structures share the high-symmetry space group  $I4/mmm$  (No. 139). When both Wyckoff sites  $4d$  (0,

0.5, 0.25) and  $4e$  (0, 0,  $z$ ) are occupied by the same atoms (see details in table 1), the compounds adopt a  $\text{BaAl}_4$ -type crystal structure [see figure 1(a)], e.g.,  $\text{AAl}_4$  and  $\text{AGa}_4$  ( $A = \text{Ca}, \text{Sr}, \text{Ba}, \text{and Eu}$ ) [80–86]. Note that, close to 443 K,  $\text{CaAl}_4$  was found to undergo a structural phase transition, from tetragonal- to monoclinic (space group  $C2/m$ , No. 12) [87]. In the  $\text{EuAl}_{4-x}\text{Ga}_x$  and  $\text{EuAl}_{4-x}\text{Zn}_x$  series of compounds, the Zn or Ga atoms replace the Al atoms both at the  $4d$  and  $4e$  sites [88, 89]. While in  $\text{AAl}_{4-x}\text{Si}_x$  or  $\text{AAl}_{4-x}\text{Ge}_x$  ( $A = \text{Sr}, \text{Ba}, \text{Eu}$ ) compounds, the Si or Ge atoms prefer to occupy only the  $4e$  site [80, 90]. These chemical substitutions can effectively tune the magnetic interactions in  $\text{EuAl}_4$ , yielding rich magnetic properties. For instance, the magnetic transition temperature increases from 16 K in  $\text{EuAl}_4$  to 25 K in  $\text{EuAl}_{2.75}\text{Zn}_{1.25}$  [47, 88]. The magnetic properties are discussed in detail in the following section.

As shown in figure 1(b), the  $\text{ThCr}_2\text{Si}_2$ -type structure represents a ternary variant of the  $\text{BaAl}_4$ -type structure, obtained by replacing two crystallographically unique Al sites ( $4d$  and  $4e$ ), which have distinct coordination environments for different atoms, e.g., Cr and Si (see details in table 1). The  $\text{ThCr}_2\text{Si}_2$ -type structure represents one of the most ubiquitous structural arrangements for ternary combinations of elements. It can also be viewed as a layered structure, where the Th-layer and CrSi blocks stack along the crystallographic  $c$ -axis. The  $\text{ThCr}_2\text{Si}_2$ -type  $AT_2X_2$  compounds exhibit a rich variety of electronic properties, including topological magnetic order, heavy-fermion features, quantum phase transition, unconventional and high- $T_c$  superconductivity (SC), as discussed in many detailed reviews [94–100]. As shown in figure 1(c), the  $\text{CaBe}_2\text{Ge}_2$ -type structure ( $P4/nmm$ , No. 129) is also an ordered ternary variant of the  $\text{BaAl}_4$  prototype. Compared with  $\text{ThCr}_2\text{Si}_2$ -type,  $\text{CaBe}_2\text{Ge}_2$  has a much lower symmetry, as clearly shown in the

**Table 1.** Atomic coordinates and site occupancy factors (SOF) of the four crystal structures shown in figure 1. We took  $\text{EuAl}_4$ ,  $\text{EuZn}_2\text{Si}_2$ ,  $\text{EuZn}_2\text{Sn}_2$ , and  $\text{EuAl}_2\text{Si}_2$  as typical examples of the  $\text{BaAl}_4$ -,  $\text{ThCr}_2\text{Si}_2$ -,  $\text{CaBe}_2\text{Ge}_2$ -, and  $\text{CaAl}_2\text{Si}_2$ -type structures, respectively. Data taken from Refs. [80, 91–93].

Structure: $\text{BaAl}_4$ -type		Space group: $I4/mmm$ , No. 139			
Atom	Wyckoff	$x$	$y$	$z$	SOF
Eu1	$2a$	0.00000	0.00000	0.00000	1
Al1	$4d$	0.00000	0.50000	0.25000	1
Al2	$4e$	0.00000	0.00000	0.38507	1

Structure: $\text{ThCr}_2\text{Si}_2$ -type		Space group: $I4/mmm$ , No. 139			
Atom	Wyckoff	$x$	$y$	$z$	SOF
Eu1	$2c$	0.00000	0.00000	0.00000	1
Zn1	$4d$	0.00000	0.50000	0.25000	1
Si1	$4e$	0.00000	0.00000	0.38560	1

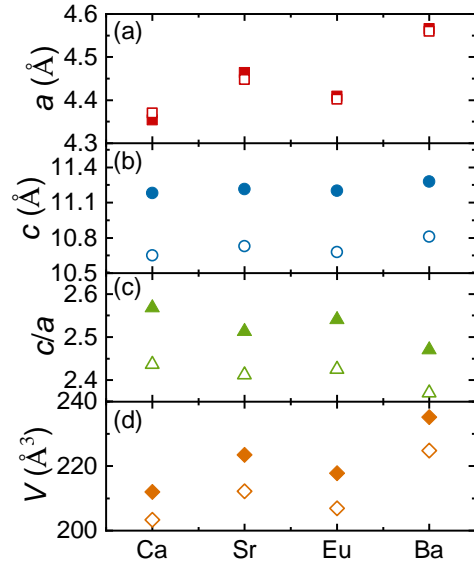
  

Structure: $\text{CaBe}_2\text{Ge}_2$ -type		Space group: $P4/nmm$ , No. 129			
Atom	Wyckoff	$x$	$y$	$z$	SOF
Eu1	$2c$	0.25000	0.25000	0.75271	1
Zn1	$2c$	0.25000	0.25000	0.36280	1
Zn2	$2a$	0.75000	0.25000	0.00000	1
Sn1	$2c$	0.25000	0.25000	0.13526	1
Sn2	$2b$	0.75000	0.25000	0.50000	1

Structure: $\text{CaAl}_2\text{Si}_2$ -type		Space group: $P\bar{3}m1$ , No. 164			
Atom	Wyckoff	$x$	$y$	$z$	SOF
Eu1	$1a$	0.00000	0.00000	0.00000	1
Al1	$2d$	0.33330	0.66670	0.63000	1
Si1	$2d$	0.33330	0.66670	0.26800	1

bottom panels, where the crystal structures viewed along the  $c$ -axis are presented. Although there are fewer  $\text{CaBe}_2\text{Ge}_2$ -type than  $\text{ThCr}_2\text{Si}_2$ -type compounds, these, too, exhibit a variety of interesting physical properties. The  $\text{CaAl}_2\text{Si}_2$ -type structure ( $P\bar{3}m1$ , No. 164) is plotted in figure 1(d), which can be viewed also as a layered structure. Although not a variant of the prototype  $\text{BaAl}_4$  structure, the  $\text{CaAl}_2\text{Si}_2$ -type compounds are the ideal platform for investigating novel phenomena. For instance, in  $\text{EuCd}_2\text{As}_2$ , strong magnetic fluctuations have been found far above the magnetic ordering temperature, which leads to a Weyl-semimetal state [10]. Unconventional contributions to the anomalous Hall and anomalous Nernst effects were observed both above and below the magnetic transition temperature of  $\text{EuCd}_2\text{As}_2$  and  $\text{EuZn}_2\text{As}_2$  [11, 101], indicating the existence of significant Berry curvatures. A colossal magnetoresistance (MR) due to the suppression of magnetic fluctuations has been reported in  $\text{EuCd}_2\text{P}_2$  [102]. It is worth mentioning that the  $\text{BaNiSn}_3$ -type structure ( $I4mm$ , No. 107) is



**Figure 2.** Lattice parameters of  $\text{AAl}_4$  (solid symbols) and  $\text{AGa}_4$  (open symbols) compounds, where  $A = \text{Ca}, \text{Sr}, \text{Eu}, \text{Ba}$ . Data taken from Refs. [80–86]. Note that, close to 443 K,  $\text{CaAl}_4$  undergoes a structural phase transition from tetragonal- to monoclinic (space group  $C2/m$ ) [87]. Here the lattice parameters of tetragonal  $\text{Ca}(\text{Al},\text{Ga})_4$  are presented.

also an ordered ternary variant of the  $\text{BaAl}_4$  prototype structure, which lacks an inversion center and has the lowest symmetry among these crystal structures.

It should be pointed out that, in this topical review, we focus mostly on the  $\text{A}(\text{Al},\text{Ga})_4$  ( $A = \text{Ca}, \text{Sr}, \text{Eu}, \text{Ba}$ ) compounds with  $\text{BaAl}_4$ -type structure. Compounds with other ordered ternary variants of the  $\text{BaAl}_4$  prototype (i.e., the  $\text{ThCr}_2\text{Si}_2$ -,  $\text{CaBe}_2\text{Ge}_2$ -, and  $\text{BaNiSn}_3$ -type structures), or with the  $\text{CaAl}_2\text{Si}_2$ -type structure will not be discussed further here. Figure 2 summarizes the lattice parameters of the  $\text{A}(\text{Al},\text{Ga})_4$  compounds. The ionic radius increases from  $\sim 1 \text{ \AA}$  of  $\text{Ca}^{2+}$  to  $\sim 1.35 \text{ \AA}$  of the  $\text{Ba}^{2+}$  ions, resulting in an expansion of the unit-cell volume [see figure 2(d)]. Thus, when moving from  $\text{Ca}(\text{Al},\text{Ga})_4$  to  $\text{Ba}(\text{Al},\text{Ga})_4$ , the  $a$ - and  $c$ -axes increase, while the  $c/a$  ratio decreases slowly. Note also that the  $a$ -axes are almost identical for  $\text{AAl}_4$  and  $\text{AGa}_4$ , while the  $c$ -axes of  $\text{AAl}_4$  are much larger than those of  $\text{AGa}_4$  [figure 2(a)-(b)]. The decrease of the  $c$ -axis lattice constant in  $\text{AGa}_4$  is most likely due to the suppression of the  $\text{Al-Ga}(\text{Al})\text{-Al}$  bond angle on increasing the Ga-content [89]. As a consequence, the electronic properties of  $\text{A}(\text{Al},\text{Ga})_4$  can be tuned by the  $\text{Al}/\text{Ga}$  substitution.

## 2.2. Charge-density-wave order

The  $\text{SrAl}_4$  and  $\text{EuAl}_4$  topological semimetals have been found to exhibit a CDW transition in a wide temperature range. Conversely,  $\text{CaAl}_4$ ,  $\text{BaAl}_4$ , as well as  $\text{AGa}_4$  ( $A = \text{Ca}, \text{Sr}, \text{Eu}, \text{Ba}$ ), exhibit a typical metallic behavior, without undergoing any CDW transition below room temperature [72]. The CDW order in  $\text{SrAl}_4$  and  $\text{EuAl}_4$ , with  $T_{\text{CDW}} \sim 243$  and 140 K, respectively, is

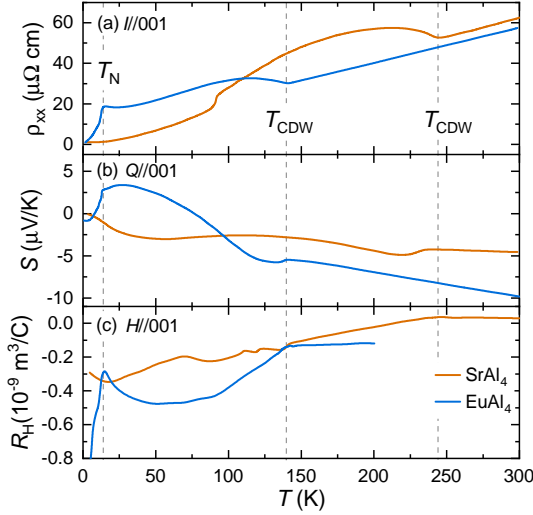


**Figure 3.** Temperature dependence of the electrical resistivity  $\rho_{xx}(T)$  (a), thermoelectric power  $S(T)$  (b), and Hall coefficient  $R_{\text{H}}(T)$  (c) for  $\text{SrAl}_4$  and  $\text{EuAl}_4$ , respectively. The dashed lines mark the charge-density-wave- and antiferromagnetic transitions. Data were taken from Refs. [72, 74, 76].

clearly reflected in their temperature-dependent electrical resistivity  $\rho_{xx}(T)$  [see figure 3(a)]. The distinct anomalies at  $T_{\text{CDW}}$  and  $T_{\text{N}}$  are also reflected in the temperature-dependent thermoelectric power  $S(T)$  and Hall coefficient  $R_{\text{H}}(T)$  [see figure 3(b)-(c)]. The enhanced resistivity due to a partial gap opening at the Fermi surface below  $T_{\text{CDW}}$  is a typical feature of the CDW materials. The CDW order also leads to a decrease in the carrier density that is proportional to  $1/R_{\text{H}}$ . In  $\text{SrAl}_4$ , there is also another anomaly in the resistivity at  $T_{\text{S}} \sim 90$  K, showing a significant hysteresis [figure 3(a)] [72]. Such a first-order transition is most likely attributed to a change of the crystal structure, from tetragonal ( $I4/mmm$ ) to monoclinic ( $C2/m$ ), as observed also in  $\text{CaAl}_4$  at  $T_{\text{S}} \sim 443$  K [87]. It could be interesting to search for possible critical phenomena related to such a structural phase transition in  $\text{SrAl}_{4-x}\text{Ga}_x$  or  $\text{Sr}_{1-x}\text{Ba}_x\text{Al}_4$ . In fact, substituting Al with Si suppresses the structural phase transition at  $T_{\text{S}}$ , allowing superconductivity to emerge, with a  $T_{\text{c}}$  of 2.1 and 2.6 K in  $\text{SrAl}_{1.5}\text{Si}_{0.5}$  and  $\text{SrAl}_2\text{Si}_2$ , respectively [86]. Differently from  $\text{SrAl}_4$ ,  $\text{EuAl}_4$  exhibits an additional antiferromagnetic order at  $T_{\text{N}} \sim 15.6$  K, and undergoes a series of metamagnetic transitions in the AFM state in an applied magnetic field [figure 3(a)] [47, 76].

Figure 4 summarizes the CDW ordering temperature  $T_{\text{CDW}}$  versus the unit cell volume and external physical pressure. As the unit cell volume decreases, the  $T_{\text{CDW}}$  decreases as well. The substitution of Al with Ga further decreases the unit cell volume [see details in figure 2(c)] and, in  $\text{EuAl}_2\text{Ga}_2$ ,  $T_{\text{CDW}}$  is suppressed down to 50 K [89]. Upon further increasing the Ga-content, the CDW order disappears. In figure 4(a),  $\text{BaAl}_4$  with  $V = 235 \text{ \AA}^3$  (not shown) is located at the left of  $\text{SrAl}_4$ . Although no

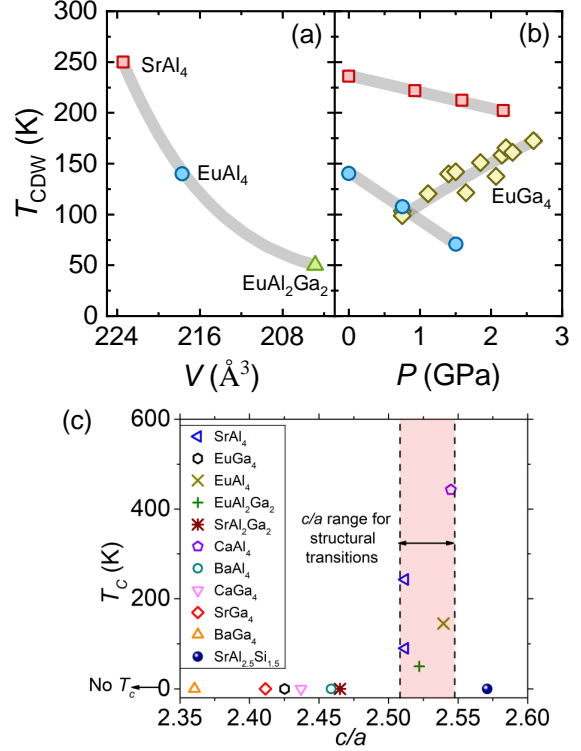


**Figure 4.** (a) Summary of charge-density-wave ordering temperature  $T_{\text{CDW}}$  versus unit-cell volume for  $\text{A}(\text{Al,Ga})_4$ . (b) The pressure-dependent  $T_{\text{CDW}}$  for  $\text{SrAl}_4$ ,  $\text{EuAl}_4$ , and  $\text{EuGa}_4$ , respectively. Data were taken from Refs. [72, 76, 89]. (c)  $T_{\text{CDW}}$  vs.  $c/a$  ratio for  $\text{A}(\text{Al,Ga})_4$ , which was reproduced from Ref. [103].

CDW transition has been detected in  $\text{BaAl}_4$  below room temperature [72], according to the  $T_{\text{CDW}}(V)$  plot, if  $\text{BaAl}_4$  has a CDW transition, its  $T_{\text{CDW}}$  might be above 400 K, a circumstance requiring further investigation.  $T_{\text{CDW}}$  is also very sensitive to external physical pressure, being linearly suppressed by it, reaching 70 K at 1.5 GPa in  $\text{EuAl}_4$  and 200 K at 2.2 GPa in  $\text{SrAl}_4$ , respectively [72]. In  $\text{EuAl}_4$ , the CDW transition becomes invisible when the external pressure exceeds 2.2 GPa [76]. Unlike the  $\text{AAl}_4$  compounds,  $\text{EuGa}_4$  shows an opposite pressure-dependent  $T_{\text{CDW}}$ . At ambient pressure,  $\text{EuGa}_4$  undergoes only an AFM transition at  $T_{\text{N}} \sim 16$  K [72, 76, 89]. At  $P = 0.75$  GPa, however, also a CDW order appears at  $T_{\text{CDW}} \sim 104$  K [figure 4(b)] [76]. Upon a further increase of pressure, the CDW order moves to higher temperatures, with  $T_{\text{CDW}}$  reaching  $\sim 172$  K at  $P = 2.6$  GPa. Interestingly, a CDW seems to occur only for  $2.51 < c/a < 2.54$  [figure 4(c)]. It is not yet clear why  $\text{EuGa}_4$  exhibits a different pressure-dependent  $T_{\text{CDW}}$  compared with  $\text{SrAl}_4$  and  $\text{EuAl}_4$ . Although the mechanism of CDW in  $\text{A}(\text{Al,Ga})_4$  is not yet fully understood, a clear discrepancy in the Fermi surfaces of  $\text{EuGa}_4$  and  $\text{EuAl}_4$ , might account for their different pressure-dependent  $T_{\text{CDW}}$ s [73, 75, 78, 79].

Since the localized  $4f$  electrons of Eu atoms are well below the Fermi level [78], the CDW order is mainly attributed to the orbitals of Al atoms. This is in good

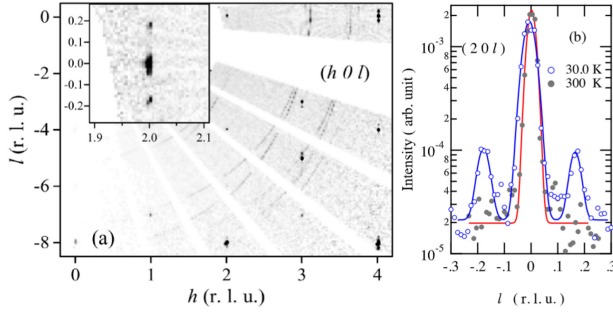


**Figure 5.** (a) Neutron scattering intensity map of the reciprocal  $(h,0,l)$  plane collected at 30 K for  $\text{EuAl}_4$ . The inset shows an enlarged map around  $(2,0,0)$ . (b) A cut along  $(0,0,l)$  direction across the nuclear peak at  $\mathbf{Q} = (2,0,0)$  at 30 K ( $T < T_{\text{CDW}}$ ) and 300 K ( $T > T_{\text{CDW}}$ ). Figures were reproduced from Ref. [104].

agreement with the observed CDW transition at  $T_{\text{CDW}} = 243$  K of  $\text{SrAl}_4$ , which has no  $4f$  electrons [72]. The CDW state has been investigated by Kaneko *et al.* using single-crystal time-of-flight neutron scattering [104]. Below  $T_{\text{CDW}}$ , additional superlattice peaks appear close to the nuclear Bragg peaks [see figure 5(b)]. Such superlattice peaks are then split along the  $(00l)$  direction [see enlarged plot in the inset of figure 5(a)]. Figure 5(b) shows a cross-sectional profile along the  $(00l)$  direction through the  $(2,0,0)$  Bragg peak, measured above and below  $T_{\text{CDW}}$ . According to the Gaussian fits, the satellites appear at  $l \sim 0.19$ . Thus, the CDW order in  $\text{EuAl}_4$  is characterized by structural satellite peaks with an incommensurate wave vector  $\mathbf{q}_{\text{CDW}} = (0, 0, \delta)$ , with  $\delta \sim 0.19$  at 30 K. Note that the  $\delta$  value changes with temperature.

By using synchrotron radiation, Shimomura and Ramakrishnan *et al.* further confirmed the CDW order in  $\text{EuAl}_4$  via single-crystal x-ray diffraction. Satellite peaks, characterized by an incommensurate wave vector  $\mathbf{q}_{\text{CDW}} = (0, 0, \delta)$  with  $\delta \sim 0.18$ , appear below 145 K [see figure 6(a)] [77, 105], thus confirming the occurrence of a CDW order. As the temperature decreases, the satellite peaks grow and shift slightly to lower  $\delta$  values, while persisting even in the AFM state. Curiously, as the temperature drops from  $T_{\text{CDW}}$  to  $T_{\text{N}}$ ,  $\delta$  not only decreases monotonically, but it also exhibits an inflection at  $T_{\text{N}}$  [figure 6(b)]. The latter implies a sizable coupling between the magnetic- and charge orders in  $\text{EuAl}_4$ .

Structural refinements indicate that the symmetry of the incommensurately modulated crystal structure is orthorhombic [105], while both the lattice and atomic coordinates of the basic structure remain tetragonal in the CDW-ordered state. Very recently, Korshunov *et al.* found that both tetragonal and orthorhombic modulations are compatible with the x-ray data [106]. In the CDW-ordered state, the satellite peaks are absent along the  $(00l)$  direction, while they show up either upon increasing the in-plane component (i.e.,  $h$  or  $k$ ) or on decreasing the out-of-plane component  $l$  [104]. Such features indicate

that structural modulations arise mostly from the atomic displacements within the  $ab$ -plane. Moreover, the Al2-Al2 and Al1-Al2 distances are hardly modulated, while the Al1-Al1 distance shows the largest modulation (see details on the Al1 and Al2 atoms in table 1) [105]. The strong modulation of Al1-Al1 distance suggests that the CDW occurs on the layers of Al1 atoms.

Now we discuss the possible mechanisms for the formation of CDW order in  $\text{BaAl}_4$ -type materials. The traditional view of CDW order comes from the Peierls' instability with a perfect Fermi surface nesting (FSN) in a 1D system to induce a Kohn anomaly or soft phonon mode, which results in a structural phase transition at low temperature [107]. The charge-density modulation is usually accompanied by a periodic lattice distortion or a modulation of the atomic positions. The modulation wave vector can be commensurate or incommensurate with respect to the crystal structure. For example, the modulation vector of  $\text{EuAl}_4$  is  $\mathbf{q}_{\text{CDW}} = (0, 0, \delta)$ , with  $\delta \sim 0.18$ , thus, its CDW order is incommensurate. Recently, the strong electron-phonon coupling has been proposed as the mechanism at the origin of CDW in 2D and 3D materials [108–110]. According to de Haas–van Alphen and ARPES experiments, as well as to electronic band-structure calculations, a substantial nesting of the Fermi surface is not evident in  $\text{EuAl}_4$  [75, 76, 78]. Nakamura and Kobata *et al.* claimed that the Dirac-like dispersion of the valence and conduction bands form Fermi surface shells resulting in an imperfect FSN along the  $\Gamma$ -Z direction in the  $\text{AAl}_4$  ( $A = \text{Sr}, \text{Eu}, \text{Ba}$ ) compounds, but not in  $\text{AGa}_4$  [75, 76, 78]. In the Al compounds (here, in  $\text{SrAl}_4$  and  $\text{EuAl}_4$ ), a large electron-phonon coupling at small  $q$ -vectors has been found in the transverse acoustic mode along the  $\Gamma$ -Z direction, whose softening is thought to provide the driving force for the CDW. However, as this softening is absent in  $\text{BaAl}_4$ , the origin of CDW order in  $\text{BaAl}_4$ -type materials is most likely the strong electron-phonon coupling interaction. This might explain the absence of a CDW order in the other closely related isostructural and isovalent compounds. Note that, since in  $\text{EuAl}_4$  the CDW order is coupled to the AFM order (see details below), such coupling adds further complexity to the origins of the spin- and charge order.

### 3. Magnetic and transport properties

#### 3.1. Magnetic phase diagrams of $\text{EuAl}_4$ and $\text{EuGa}_4$

In the  $\text{Eu}(\text{Al},\text{Ga})_4$  family of compounds, the spectroscopic and neutron/resonant x-ray studies designated to find topological features in both the momentum- and real space were motivated by the observation of a topological Hall effect [47, 111, 112]. The transport studies, in turn, were inspired by basic magnetic property characterizations which found possible magnetic ground states, suitable for hosting these topological features. Echoing this logic, in

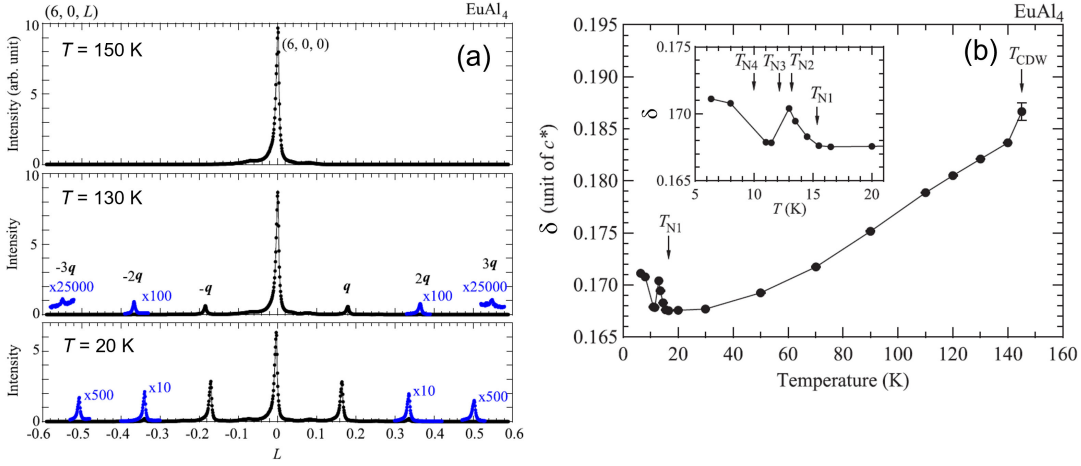


**Figure 6.** Synchrotron x-ray diffraction profiles along the  $c^*$  direction passing through the  $(6,0,0)$  collected at 150 K ( $T > T_{\text{CDW}}$ ), 130 K and 20 K ( $T < T_{\text{CDW}}$ ). The satellite peaks denoted by  $\pm nq$  are characterized by the modulation wave vector  $\mathbf{q}_{\text{CDW}} = (0,0,\delta)$  with  $\delta \sim 0.18$ . (b) Temperature dependence of the  $\delta$  value in  $\mathbf{q}_{\text{CDW}} = (0,0,\delta)$ . The inset shows an enlarged view at low temperatures. Figures were reproduced from Ref. [77].

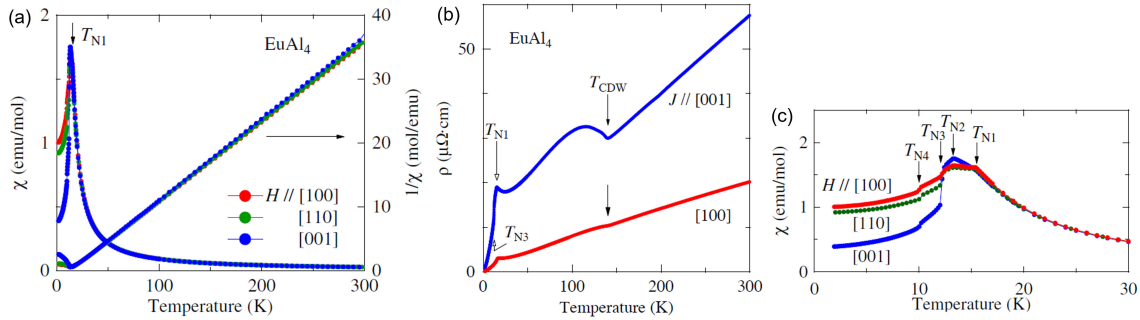


**Figure 7.** Temperature dependence of the magnetic susceptibility  $\chi(T)$  (a) and electrical resistivity  $\rho_{\text{xx}}(T)$  (b) of an  $\text{EuAl}_4$  single crystal. (c) Enlarged plot of  $\chi(T)$  at low temperature, with the arrows indicating the various AFM transitions of the  $\text{Eu}^{2+}$  ions. Arrows in (b) indicate the first AFM transition at  $T_{\text{N1}} \sim 15.4$  K and the CDW transition at  $T_{\text{CDW}} \sim 140$  K. The magnetic susceptibility was collected in a magnetic field  $\mu_0 H = 1$  T, applied both parallel ( $H \parallel [001]$ ) and perpendicular ( $H \parallel [100]$  or  $H \parallel [110]$ ) to the  $c$ -axis. Electrical resistivity was measured in a zero-field condition, with the electric current applied both parallel ( $J \parallel [001]$ ) and perpendicular ( $J \parallel [100]$ ) to the  $c$ -axis. Figures reproduced from Ref. [76].

this section, we first discuss the magnetic phase diagrams of the  $\text{Eu}(\text{Al,Ga})_4$  family, followed by discussions of the transport properties and their implications on the topological aspects. Note that, regarding the magnetic properties, only basic characterizations will be included here for the purpose of establishing the magnetic phase diagram. A detailed description of the microscopic spin textures is discussed in a later section.

The temperature-dependent magnetic susceptibility  $\chi(T)$  and the longitudinal electrical resistivity  $\rho_{\text{xx}}(T)$  up to room temperature, are summarized in figure 7 and figure 8 for  $\text{EuAl}_4$  and  $\text{EuGa}_4$ , respectively [76, 79]. While the low- $T$   $\chi(T)$  and  $\rho_{\text{xx}}(T)$  collected under various magnetic fields applied along the  $c$ -axis and within the  $ab$ -plane are summarized in figure 9 and figure 10 for  $\text{EuAl}_4$  and  $\text{EuGa}_4$ , respectively [47, 111]. In  $\text{EuAl}_4$ , four successive antiferromagnetic transitions can be identified at  $T_{\text{N1}} \sim 15.4$  K,  $T_{\text{N2}} \sim 13.2$  K,  $T_{\text{N3}} \sim 12.2$  K, and  $T_{\text{N4}} \sim 10$  K in the  $\chi(T)$  [see figure 7(c)]. These transition temperatures are consistent between the

various studies [47, 75, 76], and are clearly reflected also in the thermal expansion coefficient and the heat-capacity data [113], implying a robust magnetic order against crystal defects in  $\text{EuAl}_4$ . By contrast,  $\text{EuGa}_4$  exhibits only one AFM transition at  $T_{\text{N}} \sim 16.5$  K [see figure 8]. These transitions are also evident in the  $\rho_{\text{xx}}(T)$  curves and show a similar field dependence for both  $H \parallel ab$  and  $H \parallel c$ , i.e., the AFM transitions shift toward lower temperature as the magnetic field increases (figure 9 and figure 10). Though the  $\chi(T)$  shows a negligible anisotropy in the paramagnetic (PM) state, this is significant in  $\rho_{\text{xx}}(T)$  [see figures 7(b) and 8(b)]. In both compounds, the negligible bifurcation of the zero-field-cooling- and field-cooling magnetic susceptibilities confirms the AFM nature of the magnetic transitions [47, 75, 76, 111, 112].

Field-dependent electrical resistivity  $\rho_{\text{xx}}(H)$  and magnetization  $M(H)$  collected at various temperatures, covering both the AFM- and PM states, are summarized in figure 11 and figure 12 for  $\text{EuAl}_4$  and  $\text{EuGa}_4$ , respectively [47, 111]. At  $T = 2$  K,  $\text{EuAl}_4$  undergoes three



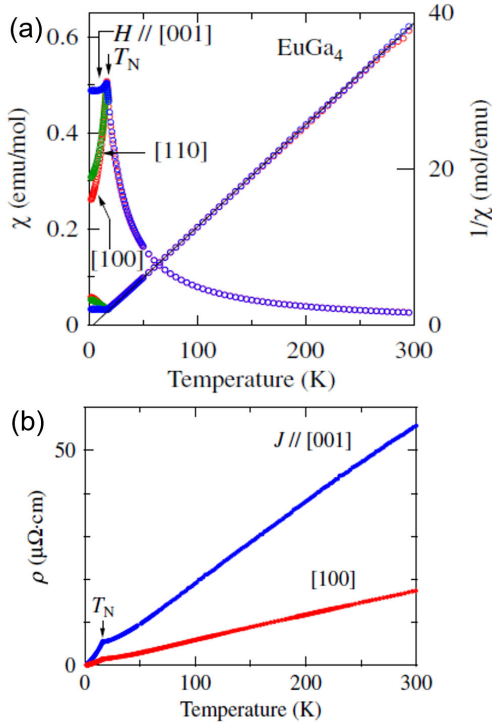


**Figure 8.** Temperature dependence of the magnetic susceptibility  $\chi(T)$  (a) and electrical resistivity  $\rho_{xx}(T)$  (b) of an  $\text{EuGa}_4$  single crystal. The magnetic susceptibility was collected by applying the magnetic field both parallel ( $H \parallel [001]$ ) and perpendicular ( $H \parallel [100]$  or  $H \parallel [110]$ ) to the  $c$ -axis. The electrical resistivity was measured in zero-field condition with the electric current applied both parallel ( $J \parallel [001]$ ) and perpendicular ( $J \parallel [100]$ ) to the  $c$ -axis. The arrows indicate the AFM transition at  $T_N \sim 16.5$  K. Figures reproduced from Ref. [79].

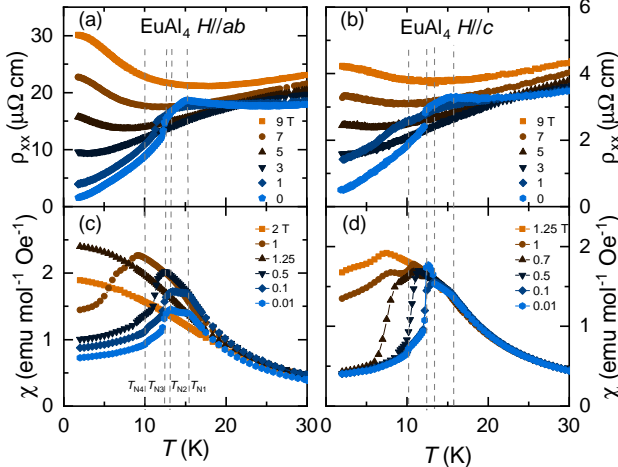


**Figure 9.** Temperature dependence of the electrical resistivity  $\rho_{xx}(T)$  collected under various magnetic fields applied within the  $ab$ -plane (a) and along the  $c$ -axis (b) for  $\text{EuAl}_4$ . Temperature dependence of the magnetic susceptibility  $\chi(T)$  collected under various magnetic fields applied within the  $ab$ -plane (c) and along the  $c$ -axis (d) for  $\text{EuAl}_4$ . The dashed lines mark the AFM transitions for  $\chi(T)$  collected in a field of 0.01 T. Data in panels (b) and (d) were taken from Ref. [47], while data in panels (a) and (c) are original.

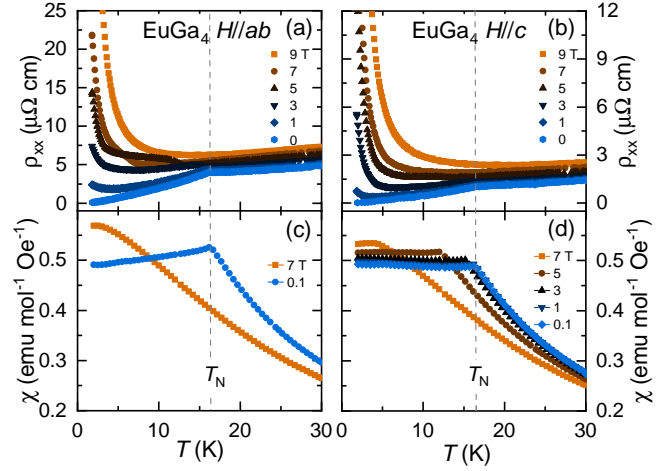


**Figure 10.** Temperature dependence of the electrical resistivity  $\rho_{xx}(T)$  collected under various magnetic fields applied within the  $ab$ -plane (a) and along the  $c$ -axis (b) for  $\text{EuGa}_4$ . Temperature dependence of the magnetic susceptibility  $\chi(T)$  collected under various magnetic fields applied within the  $ab$ -plane (c) and along the  $c$ -axis (d) for  $\text{EuGa}_4$ . The dashed lines mark the AFM transitions for  $\chi(T)$  collected in a field of 0.1 T. Data in panels (b) and (d) were taken from Ref. [111], while data in panels (a) and (c) are original.

metamagnetic transitions at  $\mu_0 H_{c1} \sim 0.8$  T,  $\mu_0 H_{c2} \sim 1.1$  T, and  $\mu_0 H_{c3} \sim 1.5$  T, before saturating at  $\mu_0 H_{c4} \sim 2.1$  T (values for  $H \parallel c$ ). These metamagnetic transitions occur at slightly different critical fields for  $H \parallel ab$  (figure 13). The  $H_{c1}$  shows up only at  $T > 4$  K for  $H \parallel ab$ .  $\text{EuGa}_4$  exhibits a significantly different field response compared with  $\text{EuAl}_4$ . For  $H \parallel ab$ , only a saturation field can be identified, with an onset slightly above  $\sim 7.2$  T (at 1.3 K), which is suppressed to  $\sim 5.3$  T at 12 K [79]. While for  $H \parallel c$ , three transitions at  $\mu_0 H_{c1} \sim 3.8$  T,  $\mu_0 H_{c2} \sim 5.6$  T, and  $\mu_0 H_{c3} \sim 7.1$  T can be tracked in  $\rho_{xx}(H)$  at  $T = 2$  K, with  $H_{c3}$  close to the saturation field in  $M(H)$ . Zhang *et al.* proposed that the transitions at  $H_{c1}$  and  $H_{c2}$ , missed in previous reports, might correspond to metamagnetic transitions, similar to those in  $\text{EuAl}_4$  [111]. Different from  $\text{EuAl}_4$ , these metamagnetic transitions do not show up in the magnetization data (figure 12), a fact requiring further investigation. In both compounds, the saturation magnetization ( $M_s \sim 6.8 \mu_B$  for  $\text{EuAl}_4$  and  $M_s \sim 6.9 \mu_B$  for  $\text{EuGa}_4$ ) is consistent with  $7.0 \mu_B$ , the expected value for  $\text{Eu}^{2+}$  ions with  $J = 7/2$ . Another prominent feature in  $\rho_{xx}(H)$  of  $\text{EuGa}_4$  is the large, non-saturating magnetoresistance, which is discussed further on in this section.

To summarize briefly, three observations can be made from the comparison between the magnetic properties of  $\text{EuAl}_4$  and  $\text{EuGa}_4$  single crystals. (1) The  $M(H)$  of  $\text{EuAl}_4$  shows three metamagnetic transitions, with a clear hysteresis in the AFM state [47], while the magnetization of  $\text{EuGa}_4$  shows only a smooth saturation. Such difference might hint at possible different origins of the transport anomalies, as will be discussed later in this section. (2)

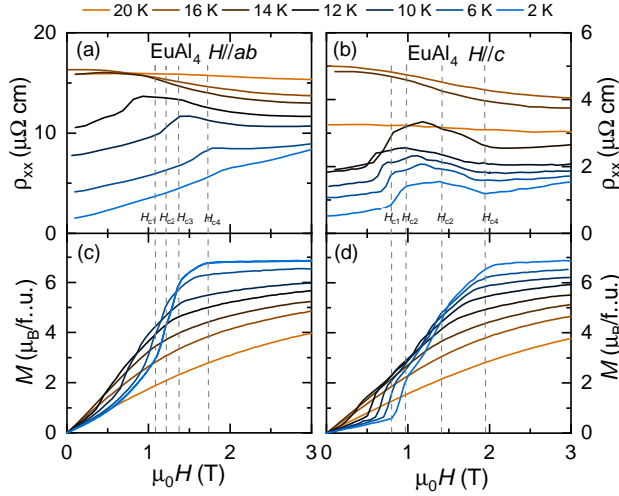


**Figure 11.** Field-dependent electrical resistivity  $\rho_{xx}(H)$  collected at various temperatures, with the magnetic field applied within the  $ab$ -plane (a) and along the  $c$ -axis (b), for  $\text{EuAl}_4$ . Field-dependent magnetization  $M(H)$  collected at various temperatures, with the magnetic fields applied within the  $ab$ -plane (c) and along the  $c$ -axis (d), for  $\text{EuAl}_4$ . Dashed lines mark the saturation field ( $H_{c4}$ ) and the three critical fields ( $H_{c1}$ ,  $H_{c2}$ , and  $H_{c3}$ ), where  $\text{EuAl}_4$  undergoes metamagnetic transitions (magnetization data at 2 K). Data in panels (b) and (d) were taken from Ref. [47], while data in panels (a) and (c) are original.

For both compounds,  $M(H)$  shows a sublinear behavior in the PM state, suggesting the presence of distinct magnetic fluctuations near the AFM order, as will be discussed in the  $\mu\text{SR}$  section. (3) For both compounds,  $\chi(T)$  and  $M(H)$  measured with  $H \parallel ab$  and  $H \parallel c$  show only moderate differences, pointing to a weak magnetic anisotropy. The latter has important implications regarding the mechanism of the formation of topological spin textures, as will be discussed later in this section.

The magnetic phase diagrams of  $\text{EuAl}_4$  and  $\text{EuGa}_4$ , as established from the aforementioned datasets for  $H \parallel ab$  and  $H \parallel c$ , are summarized in figure 13 and figure 14, respectively. For  $\text{EuAl}_4$ , the magnetic phase diagrams in the AFM state are almost identical for both field orientations and type of measurements. Conversely, for  $\text{EuGa}_4$ , evidence about possible metamagnetic transitions is only visible in the electrical-resistivity data with an out-of-plane field. For an in-plane field, the  $T_N$  of  $\text{EuGa}_4$  is smoothly suppressed to lower temperature, without undergoing any metamagnetic transitions. We also note that, in  $\text{EuAl}_4$ , additional magnetic phases have been identified at  $T < 6$  K and  $1.3$  T  $< H < 1.8$  T through heat-capacity- and dilatometry measurements in a magnetic field applied along the  $c$ -axis [113].

### 3.2. Large magnetoresistance in $\text{EuAl}_4$ and $\text{EuGa}_4$

As already mentioned above, the MR reaches  $\sim 800\%$  and  $\sim 7 \times 10^4\%$  at  $T = 2$  K in a field of 9 T in  $\text{EuAl}_4$  and  $\text{EuGa}_4$ , respectively [figure 11, 12, and 15(a)]. Such

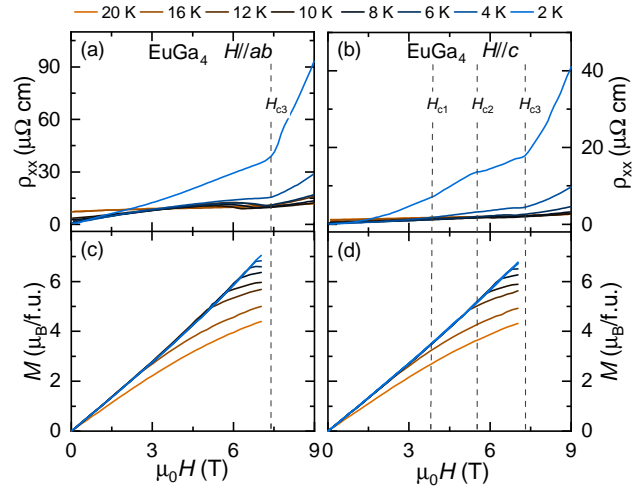


**Figure 12.** Field-dependent electrical resistivity  $\rho_{xx}(H)$  collected at various temperatures, with the magnetic fields applied within the  $ab$ -plane (a) and along the  $c$ -axis (b), for  $\text{EuGa}_4$ . Field-dependent magnetization  $M(H)$  collected at various temperatures, with the magnetic fields applied within the  $ab$ -plane (c) and along the  $c$ -axis (d), for  $\text{EuGa}_4$ . Dashed lines mark the transitions at  $H_{c1}$ ,  $H_{c2}$ , and  $H_{c3}$ , for resistivity data collected at 2 K. For  $H \parallel ab$ , only  $H_{c3}$  can be identified. Data in panels (b) and (d) were taken from Ref. [111], while data in panels (a) and (c) are original.

values are comparable to the “extremely large MR” of the nonmagnetic  $\text{BaAl}_4$  [71], the latter representing a record among the  $\text{BaAl}_4$ -type materials. Recently, Lei *et al.* extended the measurement temperature- and magnetic-field range of  $\text{EuGa}_4$  and found that its MR reaches  $\sim 5 \times 10^5\%$  at  $\mu_0 H = 40$  T, with no signs of saturation [73]. While comparable to the MR of nonmagnetic semimetals, the MR of  $\text{EuGa}_4$  is the largest among the topological magnetic semimetals [figure 15(c)]. It was also shown that, in the AFM state, the MR is well described by a quadratic field dependence (i.e.,  $H^2$ ) for  $H \leq 3.5$  T, while it levels off as the field tends towards its saturation value, a scenario typical of uncompensated semimetals [figure 15(b)]. Upon further increasing the magnetic field (up to the spin-polarized state), the MR shows an abrupt upturn. Then, it keeps increasing without saturating.

Let us now discuss the mechanisms underlying the large MR, especially that of  $\text{EuGa}_4$ . The large MR of the nonmagnetic  $\text{BaAl}_4$  and its comparable value in  $\text{EuAl}_4$  and  $\text{EuGa}_4$ , exclude the magnetic  $\text{Eu}^{2+}$  ions from the causes of MR. This is also corroborated by the fact that the MR of neither  $\text{EuAl}_4$  nor  $\text{EuGa}_4$  exhibit clear anomalies at the AFM transition temperature [figure 15(a)]. Field-induced spin fluctuations can also be excluded since, even in the spin-polarized state, where fluctuations are usually suppressed, the MR of both  $\text{EuAl}_4$  and  $\text{EuGa}_4$  continues to increase [47, 73]. Further, since the  $\text{Eu}^{2+}$  ions form a perfect square lattice (figure 1), magnetic frustrations should be absent and, hence, play no significant role. In nonmagnetic semimetals, two scenarios, one including

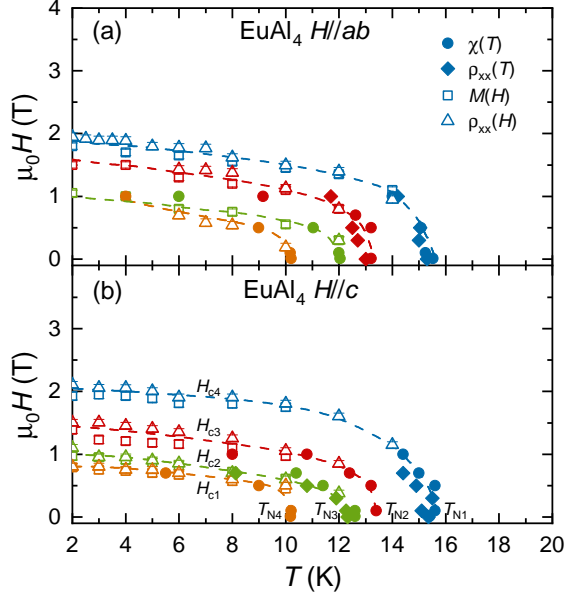


**Figure 13.** Magnetic phase diagram of an  $\text{EuAl}_4$  single crystal, with the field applied in the  $ab$ -plane (a) and along the  $c$ -axis (b). The critical temperatures ( $T_{N1}$  to  $T_{N4}$ ) are determined from  $\chi(T, H)$  (circles) and  $\rho_{xx}(T, H)$  (diamonds), while the critical fields ( $H_{c1}$  to  $H_{c4}$ ) are determined from  $M(H, T)$  (squares) and  $\rho_{xx}(H, T)$  (triangles). The dashed lines are guides to the eyes. Data in panel (a) are original, while data in panel (b) were taken from Ref. [47].

the charge compensation and another the guiding-center motion of charge carriers, are often proposed to explain the observed large MR [114]. The latter mechanism is usually relevant in topological semimetals with a linear dispersion, e.g., a Dirac spectrum. Charge compensation is not achieved in  $\text{BaAl}_4$  [71], but de Haas–van Alphen studies and electronic band-structure calculations suggest its potential realization in the PM state of  $\text{EuGa}_4$  [73, 75]. In the AFM state of  $\text{EuGa}_4$ , the very large MR hinders the accurate determination of the carrier type and density from the Hall resistivity. Considering the comparable MR of nonmagnetic  $\text{BaAl}_4$  (with a Dirac dispersion), the MR of  $\text{EuGa}_4$  can most likely be attributed to its non-trivial topological electronic bands. Taking into account the above factors, together with the anomalous transverse transport (to be discussed in the next subsection), Zhang *et al.* proposed that the interesting features in the MR of  $\text{EuGa}_4$  (i.e., a large nonsaturating value and anomalies at metamagnetic transitions) may result from a combination of charge compensation, non-trivial band topology, and topological spin textures [111]. Recently, Lei *et al.* argued that the charge compensation scenario is inconsistent with the non-saturating MR at a magnetic field up to 40 T, and that the extremely large MR of  $\text{EuGa}_4$  is a consequence of the Weyl nodal rings close to the Fermi level, protected by a mirror symmetry in the spin-polarized state [73]. The symmetry analysis shows that the AFM state of  $\text{EuGa}_4$ , with or without moment canting, does not provide the required protection for the existence of Weyl nodal-ring

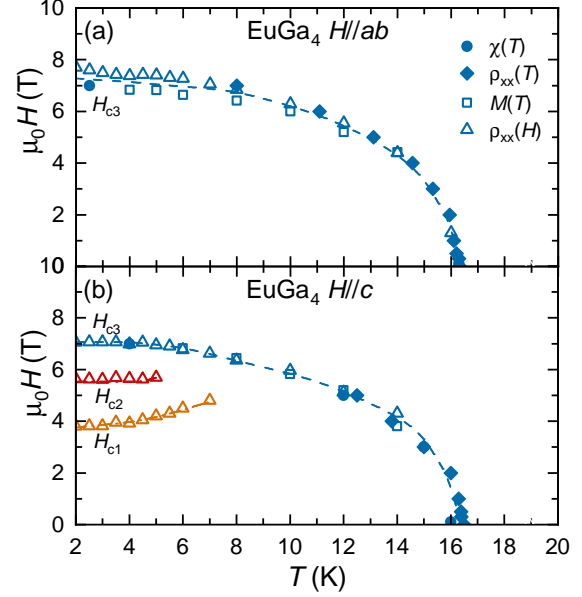


**Figure 14.** Magnetic phase diagram of an  $\text{EuGa}_4$  single crystal, with the field applied in the  $ab$ -plane (a) and along the  $c$ -axis (b). The critical temperatures  $T_N$  are determined from  $\chi(T, H)$  (circles) and  $\rho_{xx}(T, H)$  (diamonds), while the critical fields ( $H_{c1}$  to  $H_{c3}$ ) are determined from  $M(H, T)$  (squares) and  $\rho_{xx}(H, T)$  (triangles). The dashed lines are guides to the eyes. Data in panel (a) are original, while data in panel (b) were taken from Ref. [111].

states, and the recovery of mirror symmetry  $m_z$  in the spin-polarized state is necessary. This means that a field-induced topological phase transition, accompanying the AFM state to the spin-polarized state, must take place. Such transition explains also the upturn in MR upon entering the spin-polarized state.

Finally, we discuss the MR of  $\text{EuGa}_4$  within a theoretical framework that attempts to address the large non-saturating MR observed in many nonmagnetic semimetals [114]. In this framework, the monotonic increase of electrical resistivity at large fields and low temperatures, the small Hall angle (i.e.,  $\rho_{xy} \ll \rho_{xx}$ ), as well as the superlinear MR, all seem to suggest that  $\text{EuGa}_4$  is closer to the “trivial” semimetals, where the large MR stems merely from charge compensation instead of linear dispersion, inconsistent with a non-trivial band topology. However, the field-dependent Hall resistivity  $\rho_{xy}(H)$  of  $\text{EuGa}_4$  shows complex features at low temperatures (see next subsection), in contradiction with the behavior expected from “trivial” semimetals. Clearly, although appealing, the above theoretical framework cannot account for all the subtleties of the MR of  $\text{EuGa}_4$ .

### 3.3. Topological Hall effect in $\text{EuAl}_4$ and $\text{EuGa}_4$

We now turn to the transverse transport properties, embodied in the Hall resistivity  $\rho_{xy}$ . Recently, Shang *et al.* and Zhang *et al.* investigated in detail the Hall resistivity of  $\text{EuAl}_4$  and  $\text{EuGa}_4$  [47, 111]. Their field-dependent Hall-

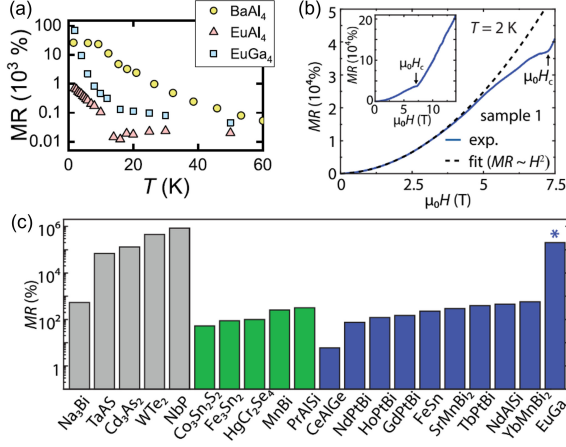


**Figure 15.** Giant MR in  $\text{BaAl}_4$ -type materials. (a) Temperature dependence of MR of  $\text{EuAl}_4$ ,  $\text{EuGa}_4$ , and  $\text{BaAl}_4$  single crystals in a field of 9 T. (b) MR of  $\text{EuGa}_4$  measured at 2 K. The arrow indicates the saturation field; the dashed line is a fit to  $H^2$ . Inset: MR data up to 14 T. (c) Comparison of the MR for various non-magnetic (gray) and magnetic (FM in green, AFM in blue) semimetals. Panels (a) were reproduced from Ref. [111], while panels (b) and (c) were reproduced from Ref. [73].

resistivity data  $\rho_{xy}(H)$ , collected at various temperatures with  $H \parallel ab$  and  $H \parallel c$ , are summarized in figure 16. In both cases, in the AFM state,  $\rho_{xy}(H)$  exhibits a hump-like anomaly for  $H \parallel c$  [panels (b) and (d)]. Such a hump is reminiscent of the topological Hall resistivity  $\rho_{xy}^{\text{THE}}$  arising from topological spin textures, e.g., magnetic skyrmions [20, 32, 41–43, 64, 115–120]. As mentioned in the introduction, the measured  $\rho_{xy}(H)$  can be decomposed into three components,  $\rho_{xy}^{\text{O}}$ ,  $\rho_{xy}^{\text{AHE}}$ , and  $\rho_{xy}^{\text{THE}}$ . Here,  $\rho_{xy}^{\text{O}}$  is the ordinary Hall effect, while  $\rho_{xy}^{\text{AHE}}$  represents the conventional anomalous Hall term, mostly determined by the electrical resistivity and magnetization. Finally,  $\rho_{xy}^{\text{THE}}$  represents the unconventional anomalous Hall term, also known as the topological Hall term, closely related to the Berry curvature in the real- and momentum space. Real-space Berry curvature is often carried by topological spin textures, with the most notable example being skyrmions in noncentrosymmetric MnSi and related compounds [64, 115–117]. The momentum-space Berry curvature, instead, underlies the famous quantum anomalous Hall effect and is nowadays often invoked to explain the anomalous Hall responses of noncollinear antiferromagnets and magnetic Weyl semimetals [11, 12, 14, 56, 121, 122].

The topological Hall resistivity is distinct from the ordinary and anomalous Hall resistivity, the latter two being proportional to the applied magnetic field  $H$  and magnetization  $M(H)$ , respectively [16]. Experimentally,  $\rho_{xy}^{\text{THE}}(H)$  can be identified as the residual between the measured Hall resistivity  $\rho_{xy}(H)$  and a fit to the ordinary and anomalous Hall resistivities, namely  $\rho_{xy}^{\text{fit}}(H) = R_0 H + R_S M(H)$ , where  $R_0$  and  $R_S$  are the ordinary and anomalous Hall coefficients. The anomalous Hall resistivity  $\rho_{xy}^{\text{AHE}}$  can be described as a combined linear- and quadratic

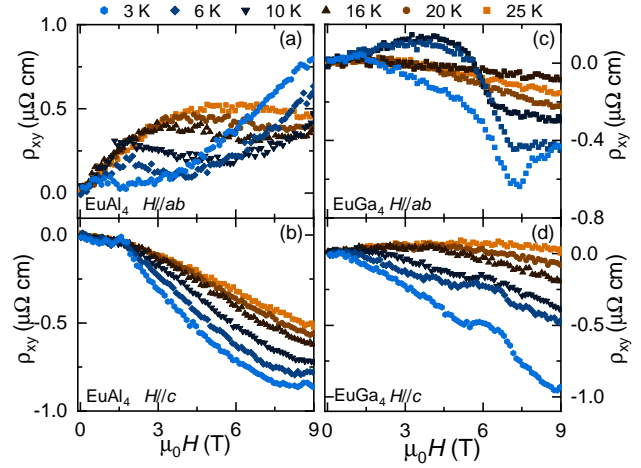


**Figure 16.** Field dependence of the Hall resistivity  $\rho_{xy}(H, T)$  of  $\text{EuAl}_4$  collected at various temperatures with the applied magnetic fields in the  $ab$ -plane (a) and along the  $c$ -axis (b). The analogous results for  $\text{EuGa}_4$  are shown in panels (c) and (d). Data in panels (a) and (c) are original, while data in panels (b) and (d) were taken from Refs. [47, 111].

dependence on the longitudinal electrical resistivity [i.e.,  $a\rho_{xx}(H) + b\rho_{xx}^2(H)$ ], corresponding to the skew scattering and side-jump mechanisms, respectively [16]. In most metallic compounds,  $\rho_{xx}(H)$  is relatively small. Consequently, modeling their  $\rho_{xx}(H)$  with  $R_S = a\rho_{xx}(H) + b\rho_{xx}^2(H)$ , or simply with  $R_S = \text{constant}$  has a negligible influence on the estimated  $\rho_{xy}^{\text{THE}}$ .

In  $\text{Eu}(\text{Al},\text{Ga})_4$  single crystals, owing to their multiband nature and giant MR, the decomposition procedure mentioned above is not straightforward. Their multiband nature is evident in the nonlinear behavior of  $\rho_{xy}(H)$  at large fields (figure 16), similar to that of nonmagnetic  $\text{BaAl}_4$  [71]. Since the multiband effect is more evident for  $H \parallel ab$ , the field-dependent  $\rho_{xy}(H)$  shows complex features [figure 16(a) and (c)], both preventing the estimation of the topological term. In what follows, we focus mostly on the case  $H \parallel c$ . To circumvent the multiband effect, Shang *et al.* and Zhang *et al.* subtracted a polynomial background from the measured  $\rho_{xy}(H)$ , to obtain a hump-like anomaly  $\Delta\rho_{xy}$  [see insets in figure 17(a) and (b)] [47]. In  $\text{EuAl}_4$ , the obtained  $\Delta\rho_{xy}$  is most prominent at temperatures below  $T_{N3}$  and in the field range between  $H_{c3}$  and  $H_{c4}$  [see figure 17(a) and (c)]. While, in  $\text{EuGa}_4$ ,  $\Delta\rho_{xy}$  is clearly observed below 10 K between  $H_{c2}$  and  $H_{c3}$  [see figure 17(b) and (d)]. The convenience of such decomposition procedure, however, comes at a price: the complexity is transferred to the interpretation of  $\Delta\rho_{xy}$ , as the relation between  $\Delta\rho_{xy}$  and  $\rho_{xy}^{\text{THE}}$  is complex.  $\Delta\rho_{xy}$  may indeed contain the  $\rho_{xy}^{\text{THE}}$  contribution, but it may also contain that from  $\rho_{xy}^{\text{AHE}}$ , or even  $\rho_{xy}^{\text{O}}$ . By using the different functional forms that  $\rho_{xy}^{\text{AHE}}$  may take — which depend on the specific mechanism underlying the conventional anomalous Hall effect, i.e.,

intrinsic, side-jump, or skew scattering — Shang *et al.* showed that the extracted  $\Delta\rho_{xy}$  may correspond to  $\rho_{xy}^{\text{THE}}$ , or to the lower/upper limit of it [47]. Considering the region where a finite  $\Delta\rho_{xy}$  shows up in the phase diagram [figure 17(c) and (d)], a topological Hall effect arising from the topological spin textures was inferred, although a trivial origin cannot be fully excluded [47, 111].

Since the centrosymmetric  $\text{EuAl}_4$  does not host conventional Dzyaloshinskii-Moriya interactions, for long thought to be the key to the formation of topological spin textures like skyrmions [27–31, 44], the appearance of a topological Hall effect in  $\text{EuAl}_4$  immediately raised the interest of the scientific community. The recent discovery of magnetic skyrmions in the Gd-based intermetallics with a centrosymmetric crystal structure, including  $\text{Gd}_2\text{PdSi}_3$ ,  $\text{Gd}_3\text{Ru}_4\text{Al}_{12}$ , and  $\text{GdRu}_2\text{Si}_2$ , stimulated the search for new mechanisms of skyrmion formation beyond the conventional ones [32–34]. In centrosymmetric magnetic materials, skyrmions can be stabilized by magnetic frustration, or by the competition between magnetic interactions and anisotropies [36]. As discussed above, the magnetic anisotropy of  $\text{EuAl}_4$  is moderate. Shang *et al.* thus speculated that, if skyrmions indeed exist in  $\text{EuAl}_4$ , they might be stabilized by the latter mechanism, similar to  $\text{GdRu}_2\text{Si}_2$  having the same crystal structure [34, 47]. Indeed, by using small-angle neutron and resonant elastic x-ray scattering, Takagi *et al.* identified square- and rhombic lattices of magnetic skyrmions in  $\text{EuAl}_4$  [48] (see details in the next section). As shown in figure 18, a square lattice of skyrmions exists between the phase boundaries that would correspond to the  $H_{c2}$  and  $H_{c3}$  defined in the magnetic phase diagram, while a rhombic lattice of skyrmions is found between  $H_{c1}$  and  $H_{c2}$  (figure 17). These distinctive topological magnetic phases are accompanied by a multistep reorientation of the magnetic modulation vector. The skyrmions in  $\text{EuAl}_4$  are argued to be stabilized by the interplay between the Ruderman-Kittel-Kasuya-Yosida (RKKY) interaction and the frustrated itinerant interactions [48, 123].

By comparing the magnetic phase diagrams in figures 17 and 18, slight differences can be identified. Skyrmion lattices are evident in the field region between  $H_{c1}$  and  $H_{c3}$ , while  $\Delta\rho_{xy}$  is most prominent between  $H_{c3}$  and  $H_{c4}$ , where the spin state is a double-Q vortex lattice described by the superposition of two sinusoidally-modulated in-plane spin components (see details in the next section) [48]. Such discrepancy cannot be attributed to the sample dependence since, in the work of Takagi *et al.*,  $\rho_{xy}(H)$  exhibit a hump-like anomaly in a field range comparable to that in the work of Shang *et al.* [figure 17(a) and figure 18(b)] [47, 48]. However, this discrepancy is plausible considering the following arguments. First, as discussed above,  $\Delta\rho_{xy}$  may not be identical to the topological Hall term  $\rho_{xy}^{\text{THE}}$ , but rather an approximate measure of it. Second, similar to  $\text{BaAl}_4$ , momentum-space

Berry curvature sources may also play a role in  $\text{EuAl}_4$ , acting in conjunction with topological spin textures in the AFM state. Third, it has been proposed that, in addition to the different Hall-resistivity terms mentioned above, there is a so-called chiral Hall effect related to the noncollinear magnetism, which exists in one-dimensional magnetic textures, such as domain walls and spin spirals [124]. This effect may provide a sizable contribution to the total  $\rho_{xy}$  as well, bringing in additional complexities.

### 3.4. Magnetotransport properties of substituted $\text{Eu}(\text{Al},\text{Ga})_4$

We discuss now briefly the magnetic and transport properties of substituted  $\text{Eu}(\text{Al},\text{Ga})_4$  single crystals. Moya *et al.* investigated an  $\text{Eu}(\text{Ga}_{1-x}\text{Al}_x)_4$  series of crystals with  $x = 0.15, 0.24, 0.31, 0.39, 0.50, 0.58, 0.71,$  and  $0.90$  [112, 125]. They found evidence of a topological Hall effect for  $x \geq 0.5$ , indicative of the emergence of non-coplanar spin textures (figure 19). At intermediate compositions ( $0.24 < x < 0.39$ ), although the magnetization and longitudinal-resistivity data reveal multiple magnetic orders, the Hall resistivity varies smoothly with field. Hence, the topological term is weak or negligible. On the Ga-rich side, e.g.  $x = 0.15$ , only one magnetic phase transition could be detected. In the spin-polarized state, a large anomalous Hall effect was found for all compositions and attributed to the appearance of Weyl nodes generated by the field-induced spin splitting of a Dirac point. Figure 19 presents some representative magnetic phase diagrams for  $\text{Eu}(\text{Ga}_{1-x}\text{Al}_x)_4$  single crystals. Consistent with the previous discussion, these results clearly reveal the coexistence of real- and momentum-space topology in a single series of materials, in this case, in  $\text{Eu}(\text{Ga}_{1-x}\text{Al}_x)_4$ .

Wang *et al.* studied the effects of Si and Cu substitution on the magnetism of  $\text{EuAl}_4$  [127]. They found that Cu or Si doping enhances the ferromagnetic interaction and that, upon Cu substitution, the direction of easy magnetization changes from the  $ab$ -plane to the  $c$ -axis. Multiple metamagnetic transitions were found in  $\text{EuAl}_{3.35}\text{Si}_{0.65}$  for  $H \parallel c$ , while  $\text{EuAl}_{3.82}\text{Cu}_{0.18}$  shows ferromagnetic features for both  $H \parallel c$  and  $H \parallel ab$ . It is interesting to check if the Si or Cu substitution could tune the topological features in real- and momentum space.

## 4. Neutron and synchrotron resonant x-ray diffraction

Considering the large neutron-absorption cross section of Eu nuclei, inelastic neutron scattering experiments are challenging. Nevertheless, elastic neutron scattering experiments have been successfully performed on  $\text{Eu}(\text{Al},\text{Ga})_4$  single crystals to solve their spin textures [48, 104, 126]. To mitigate the neutron absorption, a relatively high incident neutron energy was employed for the measurements, and the samples were cut or polished into a slab shape with a typical thickness of  $\sim 0.2\text{--}0.6$  mm.

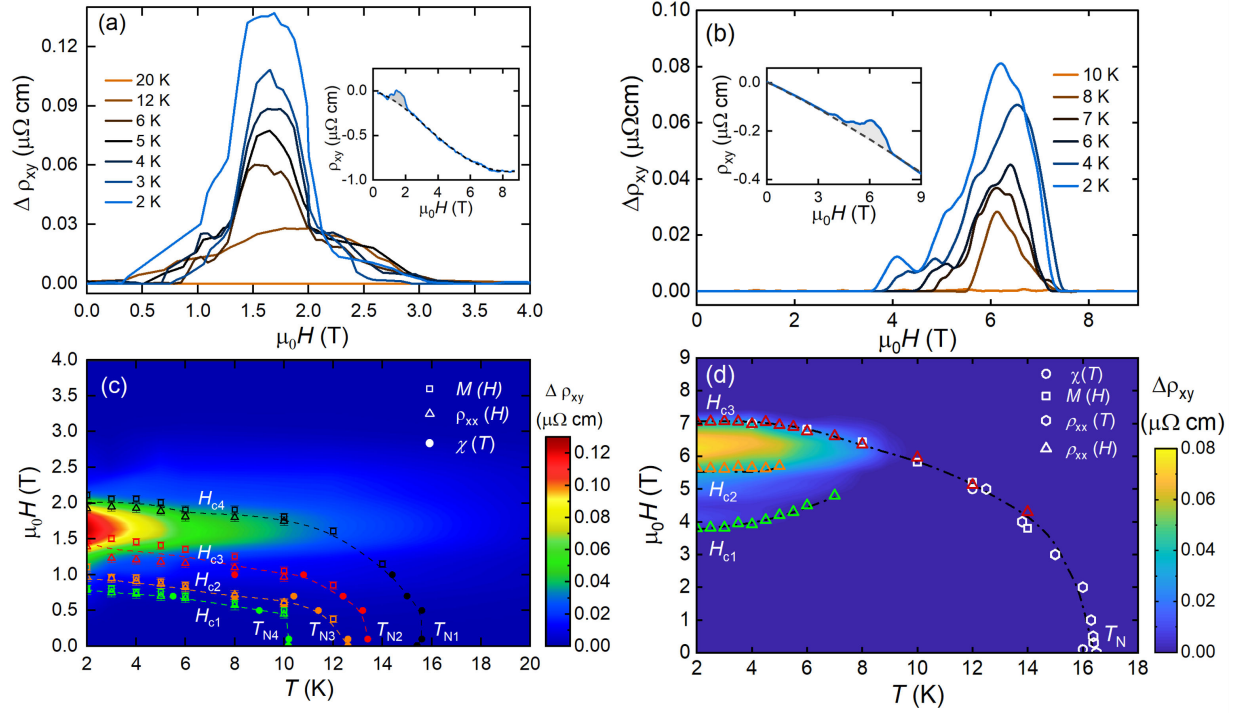


**Figure 17.** Field dependence of the extracted Hall resistivity  $\Delta\rho_{xy}(H)$  of  $\text{EuAl}_4$  (a) and  $\text{EuGa}_4$  (b) at various temperatures. Insets show the  $\rho_{xy}(H)$  data at 2 K of  $\text{EuAl}_4$ , with the dashed lines being polynomial fits. Magnetic phase diagram of  $\text{EuAl}_4$  (c) and  $\text{EuGa}_4$  (d), with the field applied along the  $c$ -axis. The background color in panels (c) and (d) represents the magnitude of  $\Delta\rho_{xy}(H)$  at various temperatures. Figures were reproduced from Refs. [47, 111].

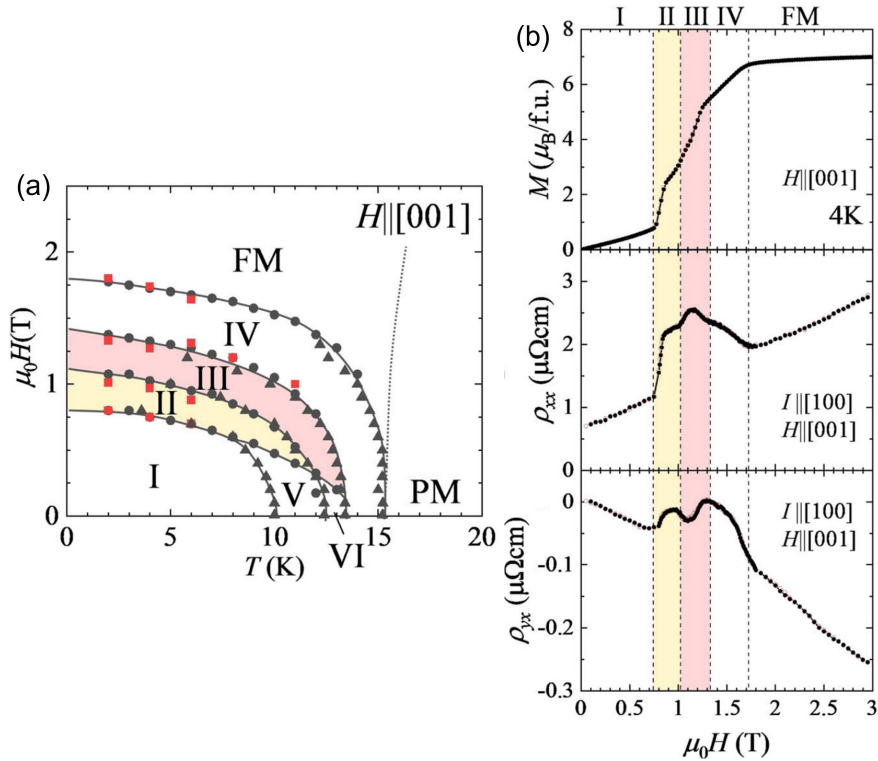


**Figure 18.** Magnetic phase diagram of  $\text{EuAl}_4$  for  $H \parallel c$ . Regions II and III correspond to a rhombic and a square skyrmion lattice, respectively. (b) Magnetic-field dependence of the magnetization, longitudinal resistivity, and Hall resistivity collected at 4 K. Figures were reproduced from Ref. [48].

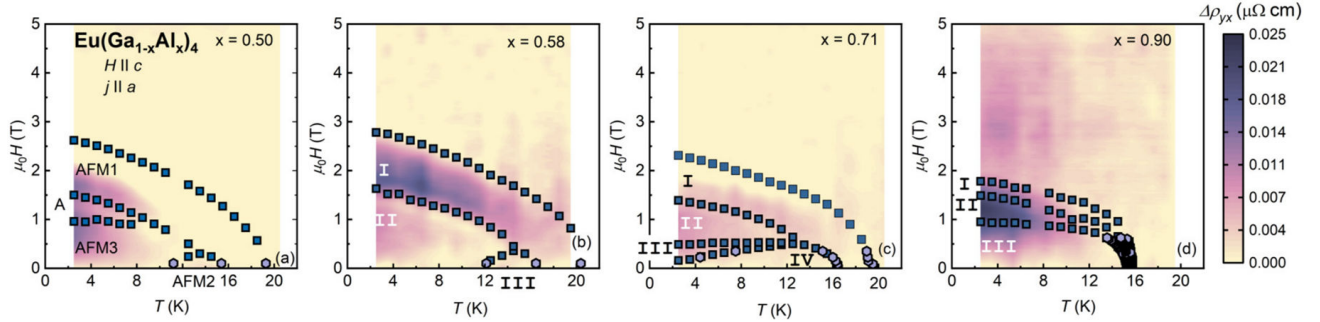


**Figure 19.** Magnetic phase diagrams of  $\text{Eu}(\text{Ga}_{1-x}\text{Al}_x)_4$  single crystals, with the field applied along the  $c$ -axis. The background color represents the magnitude of  $\Delta\rho_{yx}(H)$  at various temperatures. Figures were reproduced from Ref. [112].

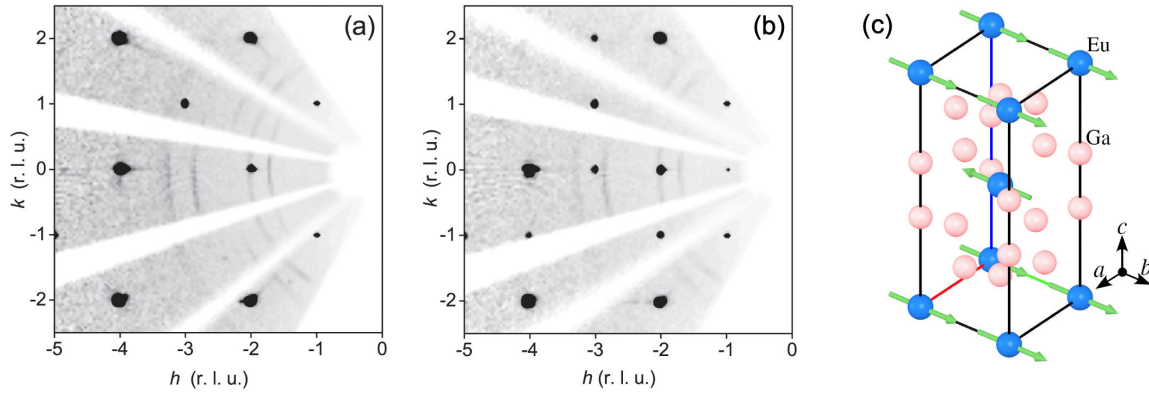


**Figure 20.** Neutron diffraction intensities of  $\text{EuGa}_4$  in the  $(h\ k\ 0)$  reciprocal lattice plane collected at 30 K (a) and 4.5 K (b). (c) Magnetic structure of  $\text{EuGa}_4$  as determined by single-crystal neutron diffraction measurements. Figures were reproduced from Ref. [126].

Since  $\text{EuGa}_4$  exhibits only one AFM transition, we first discuss the magnetic structure of  $\text{EuGa}_4$ . Consistent with the magnetic- and transport properties of  $\text{EuGa}_4$  single crystal (see section 3), the zero-field magnetic structure is rather simple. Comparing the neutron diffraction intensities collected above and below  $T_N$  [figure 20(a)-(b)], magnetic Bragg peaks indexed by a propagation vector  $\mathbf{q} = (0, 0, 0)$  were identified in the AFM phase [126]. After the absorption correction, neutron diffractions could be described by an A-type AFM magnetic structure, with the moments aligned ferromagnetically in the  $ab$ -plane, but stacked antiferromagnetically along the  $c$ -axis [figure 20(c)]. The temperature evolution of the ordered magnetic moment follows a scaled Brillouin function with  $S = 7/2$ , consistent with the zero orbital angular momentum of the  $\text{Eu}^{2+}$  ions.

Different from  $\text{EuGa}_4$ , richer phase transitions have been observed in  $\text{EuAl}_4$ . The CDW order below  $T \sim 140$  K has been confirmed also by neutron diffraction. Figure 5 presents the neutron diffraction intensity map for  $\text{EuAl}_4$  in the  $(h, 0, l)$  reciprocal lattice plane measured at 30 K. Satellite peaks indexed by  $\mathbf{q}_{\text{CDW}} = (0, 0, 0.19)$  were observed below  $T_{\text{CDW}}$ , indicating the development of a CDW superstructure along the  $c$ -axis. The details regarding the CDW order can be found in section 2; in this section we focus only on the magnetic order.

The successive magnetic transitions occurring at low temperature were also observed by Kaneko *et al.* through neutron diffraction measurements [104]. Figure 21 summarizes the temperature evolution of the diffraction patterns in the  $(h, k, 4)$  reciprocal lattice plane. At  $T = 4.3$  K ( $T < T_{N4}$ , phase IV) and 11.5 K ( $T_{N4} < T < T_{N3}$ , phase III), magnetic Bragg peaks appear at  $\mathbf{q}_1 = (\delta_1, 0, 0)$ , where  $\delta_1$  varies from 0.194(5) to 0.17(1) with increasing temperature. Upon heating the sample to  $T = 12.5$  K ( $T_{N3} < T < T_{N2}$ , phase II) and 13.5 K ( $T_{N2} < T < T_{N1}$ , phase I), magnetic Bragg peaks appear at  $\mathbf{q}_2 = (\delta_2, \delta_2, 0)$ , where  $\delta_2 = 0.085(4)$  and 0.086(4) for 12.5 and 13.5 K, respectively. No visible change in  $\delta_2$  was found at  $T_{N2}$  beyond experimental accuracy. By contrast, a clear peak shift was observed between 4.3 and 11.5 K through  $T_{N4}$ . Since no higher-order harmonics were observed, it was proposed that a transition from an amplitude-modulated-type to an equal-moment type structure may explain the transitions at  $T_{N2}$  and  $T_{N4}$ . The magnetic transition temperatures  $T_{N1}$  to  $T_{N4}$  are summarized in figure 21(e). Note that, a quantitative analysis of neutron diffraction data is rather difficult owing to the strong wavelength-dependent neutron absorption. Further neutron diffraction experiments on  $\text{Eu}(\text{Al,Ga})_4$  single crystals with isotope substitution will be necessary to reveal their magnetic structures.

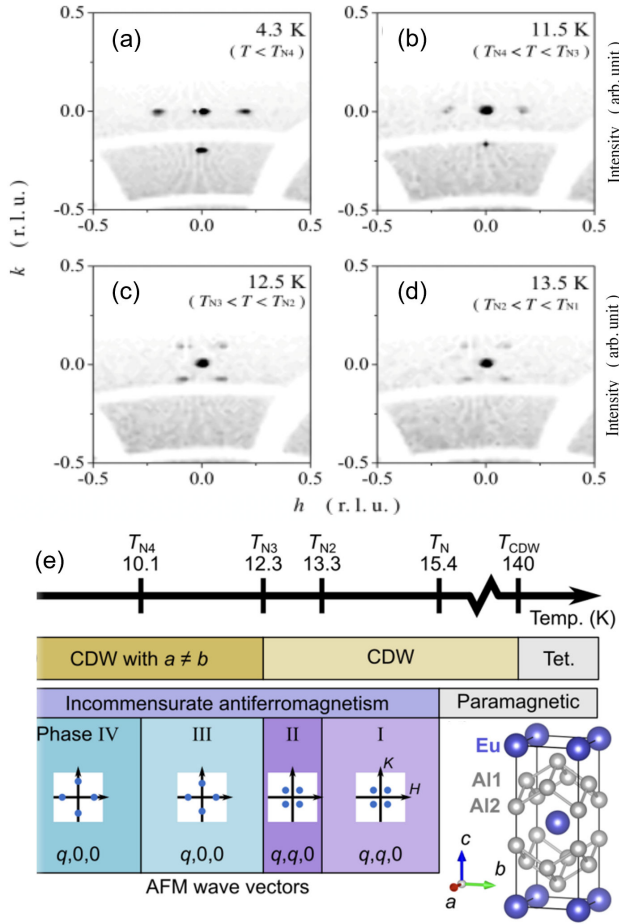


**Figure 21.** Neutron diffraction intensity maps of  $\text{EuAl}_4$  in the  $(h k 4)$  reciprocal lattice plane measured at (a) 4.3 K, (b) 11.5 K, (c) 12.5 K, and (d) 13.5 K. (e) Summary of the low-temperature phases of an  $\text{EuAl}_4$  single crystal. Figures reproduced from Refs. [104, 113].

Recent resonant elastic x-ray scattering (REXS) measurements in  $\text{EuAl}_4$  found similar results to the single-crystal neutron diffraction studies, but Vibhakar *et al.* found also additional magnetic propagation vectors with  $q = (0.175, 0, 0)$  and  $(0, 0.178, 0)$  below  $T_{N2}$  [i.e., phase II in figure 21(e)] [128]. According to the new REXS data, the magnetic structures of all four different AFM phases of  $\text{EuAl}_4$  are single- $k$  rather than multi- $k$  structures. In phase I ( $T_{N2} < T < T_{N1}$ ), the Eu moments form a spin-density-wave (SDW) order, where the moments are oriented in the  $ab$ -plane and perpendicular to the  $q$  vector (figure 21). In phase II ( $T_{N3} < T < T_{N2}$ ), another SDW order develops, with the moments aligned along the  $c$ -axis, which coexists with the first SDW order. Upon further decreasing the temperature, in phase III ( $T_{N4} < T < T_{N3}$ ), a magnetic helix structure with a single chirality is stabilized. Finally, in phase IV ( $T < T_{N4}$ ), the chirality of the magnetic helix structure is reversed, but the crystal remains a single chiral domain. As shown in figure 22, when cooling the  $\text{EuAl}_4$  crystal from phase III to phase IV, the sign of difference in

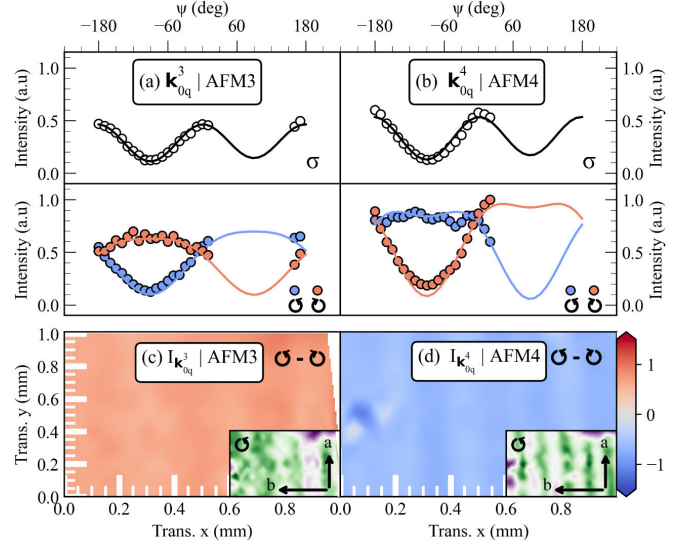


**Figure 22.** Scattered intensity from the  $k_{0q}$  satellite of the  $(0,0,8)$  reflection collected as a function of azimuth in the phase-III at 10.6 K (a) and in phase-IV at 7 K (b). Here,  $k_{0q}^3$  and  $k_{0q}^4$  are defined similarly to  $q_1 = (\delta_1, 0, 0)$  in figure 21. Data were collected using the incident light with linear horizontal ( $\sigma$ ), circular left (CL,  $\zeta$ ), circular right (CR,  $\ominus$ ) polarization, respectively. Maps showing the variation in the difference in intensity of the  $k_{0q}$  satellite collected with incident CL and CR light at 10.6 K in phase-III (c) and at 7 K in phase-IV (d). Insets show only the maps of the CL light. Figures were reproduced from Ref. [128].

intensity reverses, demonstrating the opposite magnetic chirality of these two AFM phases. Further group-theory analysis suggests that, for  $T < T_{N3}$ , the symmetry is reduced to a polar monoclinic one, which is necessary to explain the observed asymmetry in the chiral states of the magnetic helix and the spin chiral reversal [128].

The chiral reversal between phase III and IV was further confirmed by recent circular-dichroism (CD) measurements of the Bragg peaks via resonant magnetic x-ray scattering (XRMS). CD XRMS is a direct experimental probe of chiral electronic orders. Miao *et al.* performed CD XRMS on an  $\text{EuAl}_4$  single crystal in its different magnetic phases [129]. At  $T = 5$  K, the  $I(Q)^{\text{CR}}$  and  $I(Q)^{\text{CL}}$  are almost identical, resulting in a zero asymmetry of CD [ $F(Q) \sim 0$ ] [figure 23(a)-(b)]. Upon increasing the temperature to 9 K (phase IV), a giant CD at both  $q_{\text{SDW}}$  and  $-q_{\text{SDW}}$  emerges, implying that the helical SDW below  $T_{N4}$  is chiral, with a spin chirality  $\chi = 1$  [figure 23(c)-(d)]. In phase III ( $T = 11$  K), the CD changes sign, which indicates a spontaneous chirality flipping from  $\chi = 1$  to  $\chi = -1$  [figure 23(e)-(f)]. The chiral density is back to nearly zero upon warming up the sample to phase II. These results are highly consistent with the REXS data shown in figure 22.

When applying the magnetic field along the  $c$ -axis,  $\text{EuAl}_4$  undergoes a series of metamagnetic transitions, and a topological Hall resistivity appears between such transitions (figure 17), indicating the presence of possible topological spin textures in  $\text{EuAl}_4$ . To clarify this issue, Takagi *et al.* performed small-angle neutron scattering



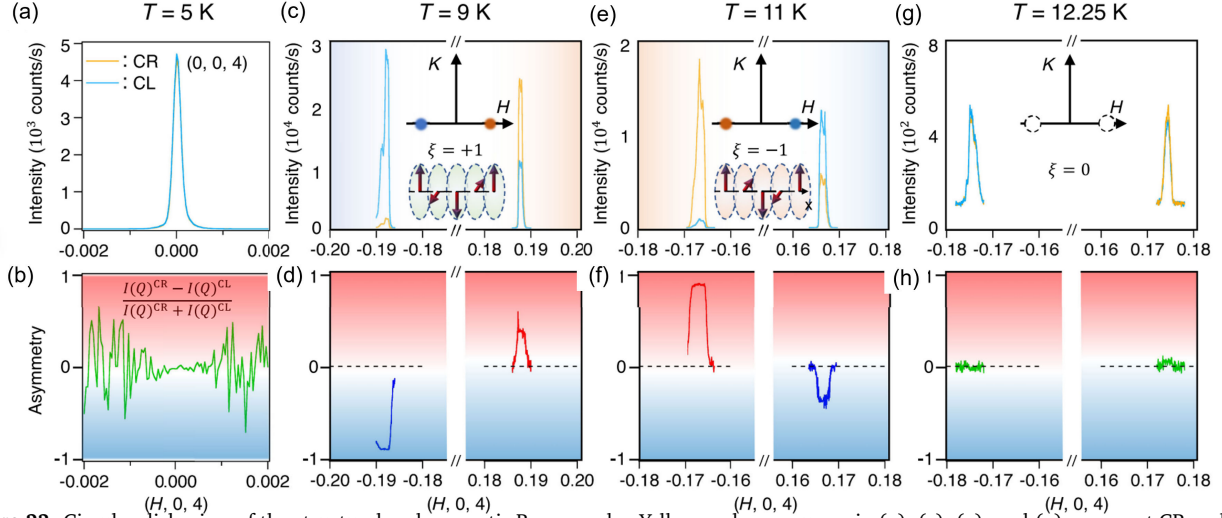


**Figure 23.** Circular dichroism of the structural and magnetic Bragg peaks. Yellow and cyan curves in (a), (c), (e), and (g) represent CR and CL incident photon polarizations, respectively. Red, green, and blue curves in (b), (d), (f), and (h) represent positive, zero, and negative asymmetry of the CD  $F(Q)$ . The definition of  $F(Q)$  is shown in panel (b), where  $I(Q)^{\text{CR}}$  and  $I(Q)^{\text{CL}}$  represent the x-ray intensities obtained under a CR and CL incident photon energy, respectively. Figures were reproduced from Ref. [129].

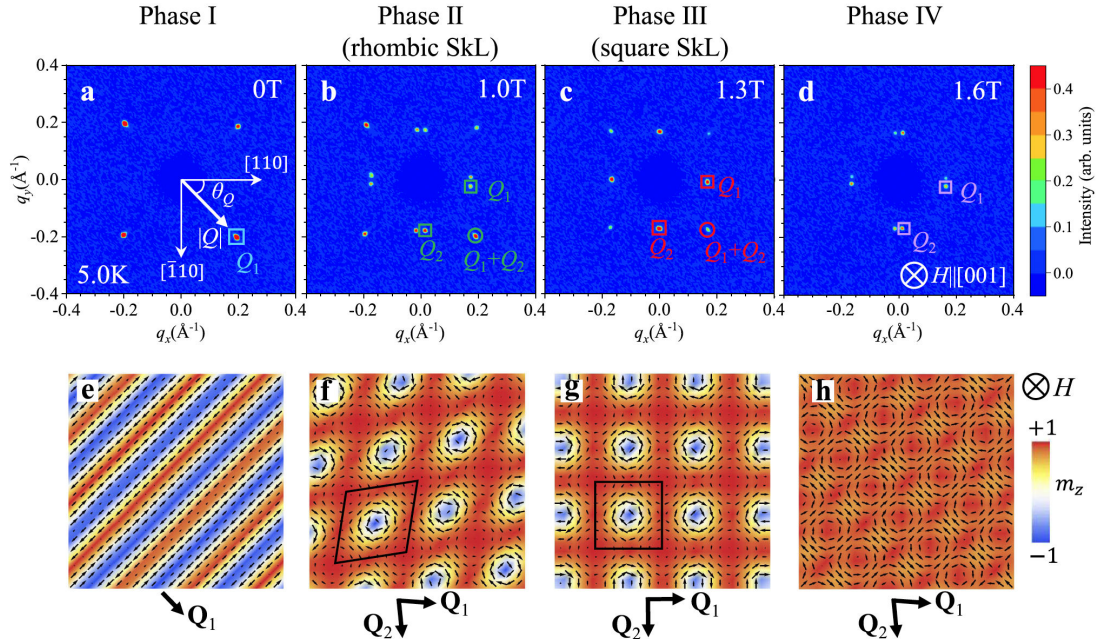


**Figure 24.** Magnetic-field dependence of SANS patterns for  $\text{EuAl}_4$ . (a)-(d) Typical patterns collected at  $T = 5$  K under various magnetic fields for  $H \parallel c$ . (e)-(h) Schematics of the screw, rhombic skyrmion lattice, square skyrmion lattice, and vortex-lattice spin textures, respectively. Each phase is characterized by distinctive orientations of the fundamental magnetic-modulation vectors  $Q_1$  and  $Q_2$ . Background color represents the out-of-plane component of the local magnetic moment  $m_z$ . Here, phases I-IV are defined differently from those in Fig. 18. Figures were reproduced from Ref. [48].

(SANS) measurements in the different magnetic phases of an  $\text{EuAl}_4$  single crystal (figure 24) [48]. The SANS patterns were collected at  $T = 5$  K, in an applied magnetic field of 0, 1.0, 1.3, and 1.6 T, corresponding to the phases I to IV in figure 18. Note that, the numbering of the various phases in Refs. [104, 113, 128] is reversed with respect to Ref. [48]. In the absence of a magnetic field, the fundamental modulation vector is  $Q_1 = (0.19, 0, 0)$ , and

the polarization analysis confirms the helical spin texture [figure 24(e)], consistent with REXS results [128]. In a 1.0 T field, the fundamental modulation vector changes to  $(0.073, 0.097, 0)$ , leading to pairs of magnetic Bragg peaks due to the domain effect. Surprisingly, strong  $Q_1 + Q_2$  reflections have been observed along the (100) direction, which was also confirmed through REXS [48]. The existence of  $Q_1 + Q_2$  reflections reveals the double-Q

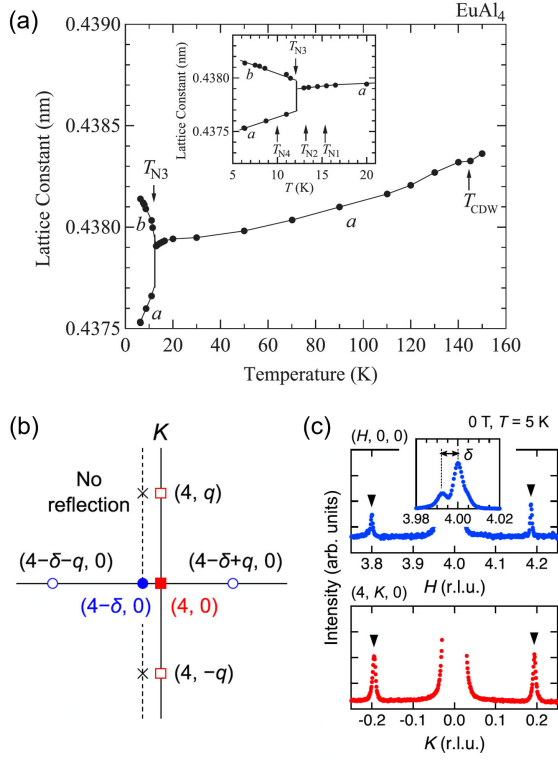


**Figure 25.** (a) Lattice constants vs. temperature determined via synchrotron x-ray diffraction measurements. (b) Schematic plots of the observed fundamental- and magnetic Bragg reflections on the scattering plane at  $T = 5$  K in zero field. (c) Intensity profiles of the  $(h, 0, 0)$  and  $(4, k, 0)$  scans at  $T = 5$  K in zero field. The inset enlarges the splitting of the fundamental  $(400)$  reflection. Figures were reproduced from Refs. [77, 130].

character of the spin textures, in contrast to the single- $Q$  structure in the absence of a magnetic field. A polarization analysis of the SANS data confirms that both  $Q_1$  and  $Q_2$  modulations are of helical character, as in the zero-field case. Since the modulation vectors  $Q_1$  and  $Q_2$  are not perpendicular to each other, the spin textures can be represented as a rhombic skyrmion lattice [figure 24(f)]. By further increasing the magnetic field to 1.6 T, the spin textures remain double- $Q$ , leading to a square lattice of magnetic skyrmions in phase III [figure 24(g)] and vortices in phase IV [figure 24(h)], respectively. Consequently, the presence of magnetic skyrmions leads to a THE in  $\text{EuAl}_4$ .

Although a complete understanding of the rich electronic phases of  $\text{EuAl}_4$  is not yet available, recent x-ray diffraction experiments suggest a sizable spin-lattice coupling, which plays an important role in determining the various spin textures in  $\text{EuAl}_4$  [77, 130]. Shimomura *et al.* performed non-resonant synchrotron x-ray diffraction measurements in a wide temperature range in  $\text{EuAl}_4$ . Except for the anomaly at  $T_{\text{CDW}}$ ,  $\text{EuAl}_4$  exhibits a tetragonal-orthorhombic structural transition at  $T_{\text{N3}}$ , where the unit cell is compressed and elongated along the  $a$ - and  $b$ -axis, respectively [see figure 25(a)].

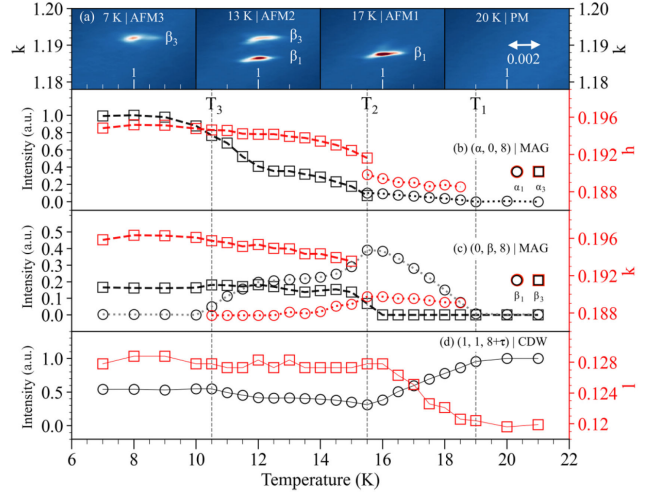


**Figure 26.** (a) Reciprocal space maps centered about the  $(1, 1+\beta, 8)$  reflection in the  $hk$  plane collected in the PM, AFM1, AFM2, and AFM3 phases. Temperature dependence of the normalized integrated intensity and the magnitude of the propagation vector of (b)  $(\alpha, 0, 8)$ , (c)  $(0, \beta, 8)$ , and (d)  $(1, 1, 8+\tau)$  reflections. Figure was reproduced from Ref. [131].

However, no structural anomaly could be detected at the other magnetic transitions (i.e., at  $T_{\text{N1}}$ ,  $T_{\text{N2}}$ , and  $T_{\text{N4}}$ ). The magnetic structure of  $\text{EuAl}_4$  changes significantly at  $T_{\text{N3}}$ , from a SDW to a helix, while the change is moderate at  $T_{\text{N2}}$  and  $T_{\text{N4}}$ . Although the mechanism underlying the lattice distortion at  $T_{\text{N2}}$  is not yet fully understood, it has a huge impact on the spin textures. Gen *et al.* performed RXS experiments on  $\text{EuAl}_4$  at  $T = 5$  K [figure 25(b)-(c)] [130]. In the absence of a magnetic field, the magnetic modulation vectors are parallel to the elongated  $b$ -axis. The rhombic- and square skyrmion phases were found to possess a  $\sim 0.1\%$  and  $\sim 0.03\%$  orthorhombic distortion in the  $ab$  plane, respectively, implying a sizable coupling between the spins and lattice in  $\text{EuAl}_4$ .

Vibhakar *et al.* performed high-resolution resonant x-ray and neutron scattering studies on a  $\text{EuAl}_2\text{Ga}_2$  single crystal [131]. Similar to the  $\text{EuAl}_4$  case, also in  $\text{EuAl}_2\text{Ga}_2$ , the CDW order ( $T_{\text{CDW}} = 50$  K) and the AFM orders (at  $T_{\text{N1}} = 19.5$  K,  $T_{\text{N2}} = 15$  K,  $T_{\text{N3}} = 11$  K) coexist [125]. The magnetic orders are denoted as AFM1 ( $T_{\text{N1}} < T < T_{\text{N2}}$ ), AFM2 ( $T_{\text{N3}} < T < T_{\text{N2}}$ ), and AFM3 ( $T < T_{\text{N3}}$ ), respectively. The magnetic propagation vectors of  $\text{EuAl}_2\text{Ga}_2$  share some common features with  $\text{EuAl}_4$ . For instance, the intensity of CDW order is significantly reduced below  $T_{\text{N1}}$  and it becomes almost temperature-independent below  $T_{\text{N2}}$  (figure 26). Clearly, the formation of magnetic order suppresses the CDW order, demonstrating that the two electronic orders are in competition [131]. Similar results have been found also in pure  $\text{EuAl}_4$  [129], where the CDW couples strongly with the SDW and displays a rare commensurate-to-incommensurate transition at the chirality flipping temperature. Note that, the CDW order is formed by

the *itinerant* electrons of Al atoms, while the *localized* 4*f* electrons of Eu atoms are responsible for the magnetic orders in  $\text{Eu}(\text{Al,Ga})_4$ . If the onset of the magnetic order polarizes the itinerant electronic density, it could destabilize the CDW order. Another mechanism for the coupling between the SDW and CDW orders involves lattice strain. The magnetic order renormalizes the CDW order through the magnetoelastic coupling. This is clearly illustrated in figure 25(a), where the structural distortion appears at  $T_{\text{N}3}$  in  $\text{EuAl}_4$ . These observations suggest a strong coupling between the localized 4*f* electrons and itinerant electrons in  $\text{Eu}(\text{Al,Ga})_4$ , and a theoretical modeling for the spin correlations in  $\text{Eu}(\text{Al,Ga})_4$  should consider the perturbations caused by the lattice distortion and/or charge order, which might also play a significant role in the formation of the skyrmion lattice.

### 5. Muon-spin rotation and relaxation

During the past decades, muon-spin rotation, relaxation, and resonance (known as  $\mu\text{SR}$ ), has become one of the most powerful methods to study the quantum materials at a microscopic level. Due to the large muon magnetic moment ( $\mu_\mu = 8.89 \mu_{\text{N}}$ ) and almost 100% spin-polarized muon beams, muons can sense extremely small internal fields ( $\sim 10^{-2}$  mT), and thus, probe local magnetic fields of either nuclear or electronic nature. In addition, since the muon is an elementary spin-1/2 particle, it acts as a purely magnetic probe, i.e., free of quadrupole interactions. All these features make  $\mu\text{SR}$  an ideal technique for investigating the intrinsic magnetic properties of materials in the absence of external fields. Depending on the reciprocal orientation of the external magnetic field  $B$  with respect to the initial muon-spin direction  $S$ , in a  $\mu\text{SR}$  experiment, two different configurations are possible: i) In transverse field (TF)  $\mu\text{SR}$  the externally applied field  $B$  is perpendicular to  $S$  and the muon spin precesses around  $B$ ; ii) In a longitudinal field (LF) configuration the applied field is parallel to  $S$ , generally implying only a relaxing  $\mu\text{SR}$  signal. In the absence of external magnetic fields, both configurations can be used to conduct zero-field (ZF)- $\mu\text{SR}$  measurements. In a weak transverse-field (wTF)- $\mu\text{SR}$ , where the applied magnetic field is relatively weak (i.e., a few millitesla), one can determine the temperature evolution of the magnetic volume fraction, as well as the magnetic ordering temperature. As for the ZF- and LF- $\mu\text{SR}$ , they can be used to study the temperature evolution of the magnetically ordered phase and the dynamics of spin fluctuations. Here, we outline briefly only the basics of the  $\mu\text{SR}$  technique and direct the reader to other references for more detailed information [132–139].

Zhu *et al.* performed systematic  $\mu\text{SR}$  measurements on both  $\text{EuAl}_4$  and  $\text{EuGa}_4$  single crystals. Figure 27 summarizes the wTF- $\mu\text{SR}$  results. In the PM state (i.e., at

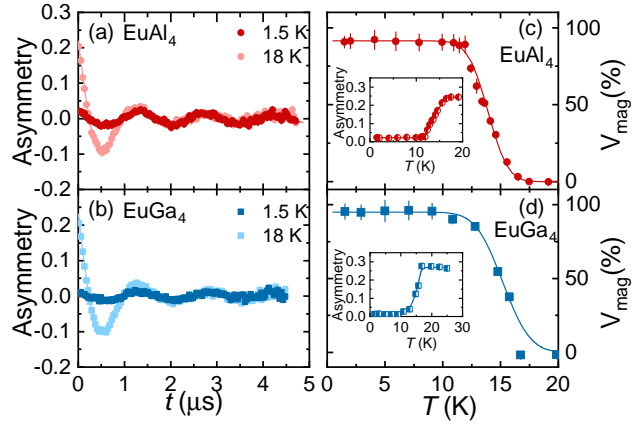


**Figure 27.** wTF- $\mu\text{SR}$  spectra of (a)  $\text{EuAl}_4$  and (b)  $\text{EuGa}_4$  single crystals, collected in the AFM (1.5 K) and PM (18 K) states in a weak transverse field of 5 mT. The solid lines represent fits to  $A_{\text{wTF}}(t) = A_{\text{NM}} \cos(\gamma_\mu B_{\text{int}} t + \phi) \cdot e^{-\lambda t}$  (see details in Ref. [50]). Temperature-dependent magnetic volume fraction for (c)  $\text{EuAl}_4$  and (d)  $\text{EuGa}_4$ . The insets show the wTF- $\mu\text{SR}$  asymmetry  $A_{\text{NM}}$  vs temperature. Data were taken from Ref. [50].

18 K), a weak transverse field of 5 mT leads to oscillations [figure 27(a)-(b)]. In the long-range ordered AFM state (i.e., at 1.5 K), the applied field is much smaller than the internal field. As a consequence, upon entering the AFM state, muon spins precess with frequencies that reflect the internal fields at the muon-stopping sites rather than the weak applied field. Normally, the magnetic order leads to a very fast muon-spin depolarization in the first tenths of  $\mu\text{s}$ . In the PM state, instead, all the implanted muons precess at the same frequency  $\gamma_\mu B_{\text{int}}$ , determined by the external magnetic field. As the temperature approaches  $T_{\text{N}}$ , only the muons implanted in the remaining PM or non-magnetic (NM) phase precess at the frequency  $\gamma_\mu B_{\text{int}}$ , here reflected in a reduced oscillation amplitude. The PM (or NM) sample fraction is determined by the oscillation amplitude. In both  $\text{EuAl}_4$  and  $\text{EuGa}_4$ ,  $A_{\text{NM}}$  starts to decrease near the onset of AFM order [see insets in figure 27(c)-(d)]. The determined magnetic volume fraction  $V_{\text{mag}}$ , 91% for  $\text{EuAl}_4$  and 95% for  $\text{EuGa}_4$ , indicate a fully magnetically ordered state at low temperature. The transition temperatures  $T_{\text{N}}$  can also be tracked from  $V_{\text{mag}}(T)$ . Their onsets at  $\sim 16.5$  K and  $\sim 16.7$  K for  $\text{EuAl}_4$  and  $\text{EuGa}_4$  [figure 27(c)-(d)], are in very good agreement with the magnetic susceptibility and electrical resistivity data (see details in section 3).

As for the ZF- $\mu\text{SR}$  spectra, both crystals show typical features of magnetically ordered materials (figure 28) [136–139]. In the PM state, the  $\mu\text{SR}$  spectra still exhibit a relatively fast muon-spin depolarization ( $\sim 2 \mu\text{s}^{-1}$ ), implying the existence of strong spin fluctuations. In  $\text{EuAl}_4$  and  $\text{EuGa}_4$ , the nuclear moments lead only to a small muon-spin relaxation rate, with typical values of less than  $0.1 \mu\text{s}^{-1}$  [140]. The  $\mu\text{SR}$  spectra in the AFM state ( $T \leq T_{\text{N}}$ ) are characterized by highly damped oscillations [see insets in figure 28(a)-(b)], superimposed

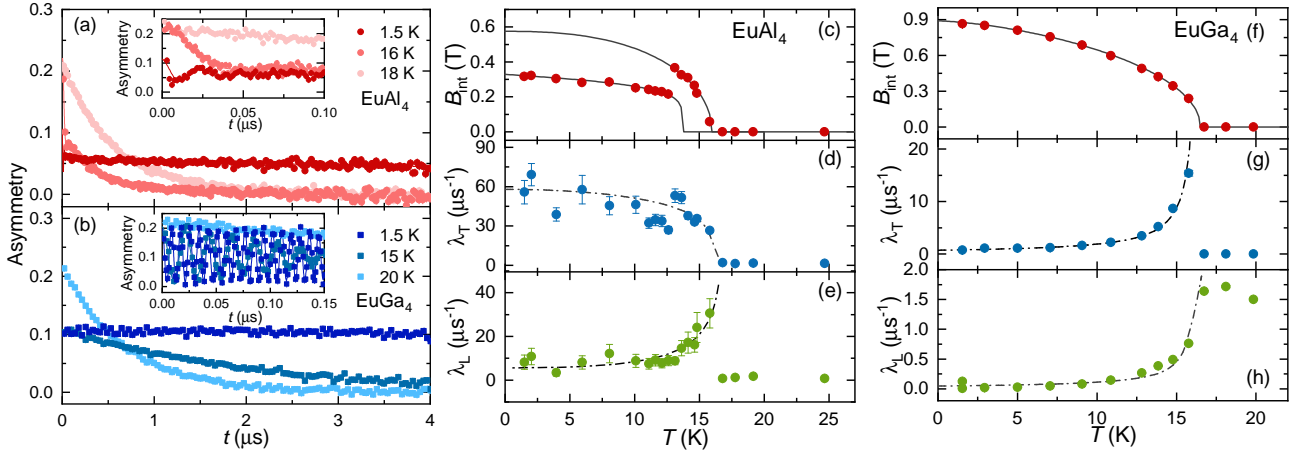


**Figure 28.** Representative ZF- $\mu$ SR spectra collected in a transverse muon-spin configuration at temperatures covering both the PM and AFM states of  $\text{EuAl}_4$  (a) and  $\text{EuGa}_4$  (b), respectively. Insets highlight the short-time spectra, illustrating the coherent oscillations caused by the long-range AFM order. Temperature dependence of the internal field  $B_{\text{int}}(T)$  (c), transverse muon-spin relaxation rate (known also as damping rate)  $\lambda_T(T)$  (d), and longitudinal muon-spin relaxation rate  $\lambda_L(T)$  (e) for  $\text{EuAl}_4$ , as derived from ZF- $\mu$ SR analysis. The analogous results for  $\text{EuGa}_4$  are shown in panels (f)-(h). The solid lines through the data represent fits to the theoretical models reported in Ref. [50], while the dash-dotted lines are guides to the eyes. Data were taken from Ref. [50].

on a slowly decaying relaxation, observable only at long times. There are two nonequivalent muon-stopping sites in  $\text{EuAl}_4$ , while a single muon-stopping site is sufficient to describe the ZF- $\mu$ SR spectra in  $\text{EuGa}_4$ . In  $\text{EuAl}_4$ , muons stopping at the second site do not undergo any precession, but show only a slow longitudinal relaxation, with a similar temperature dependence to  $\lambda_L(T)$  [figure 28(e)].

$\text{EuAl}_4$  and  $\text{EuGa}_4$  show rather different temperature-dependent  $B_{\text{int}}(T)$  [figure 28(c) and (f)]. Since  $B_{\text{int}}$  is directly proportional to the magnetic moment, the evolution of  $B_{\text{int}}$  reflects that of the magnetic structure. According to neutron scattering studies (see details in section 4), in  $\text{EuAl}_4$ , the magnetic  $q$ -vector changes from  $\mathbf{q}_1 = (0.085, 0.085, 0)$  at  $T_N = 13.5$  K to  $\mathbf{q}_2 = (0.170, 0, 0)$  at 11.5 K and slightly to  $\mathbf{q}_3 = (0.194, 0, 0)$  at 4.3 K [104]. Therefore, the drop of  $B_{\text{int}}$  at  $\sim 13$  K is attributed to a change in magnetic structure from  $q_1$  to  $q_2$ . The modification of magnetic structure from  $q_2$  to  $q_3$  with the magnetic moments pointing at the same direction is too tiny to have a measurable effect on  $B_{\text{int}}$ . Unlike  $\text{EuAl}_4$ , the AFM structure of  $\text{EuGa}_4$  is rather simple [with a single magnetic vector,  $\mathbf{q} = (0, 0, 0)$ , down to 2 K] [126], leading to a monotonic decrease in  $B_{\text{int}}(T)$  as the temperature increases. The significantly different internal field values are most likely attributed to the different muon-stopping sites or to different magnetic structures in  $\text{EuAl}_4$  and  $\text{EuGa}_4$ . Further theoretical calculations, including the determination of the muon-stopping sites and of hyperfine fields, might be helpful to better appreciate the differences between  $\text{EuAl}_4$  and  $\text{EuGa}_4$ .

Figure 28(d)-(e) and (g)-(h) summarize the transverse and longitudinal  $\mu$ SR relaxation rates,  $\lambda_T(T)$  and  $\lambda_L(T)$ . The transverse relaxation rate  $\lambda_T$  is a measure of the width of the static magnetic field distribution at

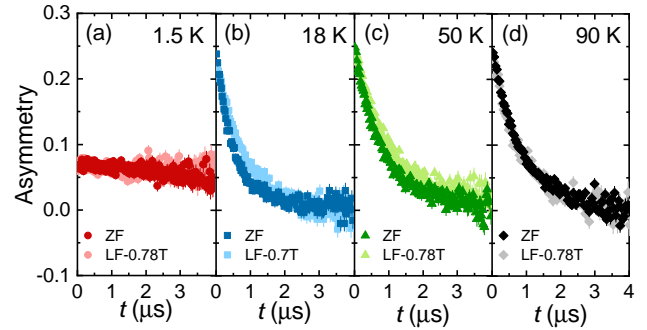


**Figure 29.** LF- $\mu$ SR time-domain spectra collected at 1.5 K (a), 18 K (b), 50 K (c), and 90 K (d) in an applied magnetic field of 0 and 0.7 or 0.78 T for  $\text{EuAl}_4$ .  $\text{EuGa}_4$  exhibit similar LF- $\mu$ SR results [50]. The applied magnetic field is parallel to the muon-spin direction. Data in panels (a)-(c) were taken from Ref. [50], while data in panel (d) are original.

the muon-stopping site and is also affected by dynamical effects, as e.g., spin fluctuations. The longitudinal relaxation rate  $\lambda_L$  is determined solely by spin fluctuations.  $\text{EuAl}_4$  and  $\text{EuGa}_4$  exhibit completely different  $\lambda_T(T)$  in the AFM state. In  $\text{EuAl}_4$  [figure 28(d)],  $\lambda_T$  is zero in the PM state, to become increasingly prominent as the temperature decreases below  $T_N$ . Such a large  $\lambda_T$  at  $T \ll T_N$  is unusual for an antiferromagnet and implies an increasingly inhomogeneous distribution of local fields in the AFM state of  $\text{EuAl}_4$ . The enhanced local-field distribution is most likely related to the complex spatial arrangement of the Eu magnetic moments in  $\text{EuAl}_4$ , where the magnetic propagation vector is incommensurate with the crystal lattice [104]. By contrast, in  $\text{EuGa}_4$  [figure 28(g)],  $\lambda_T(T)$  follows the typical behavior of materials with a long-range (anti)ferromagnetic order [132–134], i.e., diverging at  $T_N$  and continuously decreasing at  $T < T_N$ . Such  $\lambda_T(T)$

suggests a very homogeneous distribution of local fields, consistent with the commensurate magnetic propagation vector in  $\text{EuGa}_4$  [126].  $\text{EuAl}_4$  and  $\text{EuGa}_4$  exhibit a similar temperature-dependent  $\lambda_L(T)$  [figure 28(e) and (h)], which diverges near  $T_N$ , followed by a significant drop at  $T < T_N$ , indicating that spin fluctuations are the strongest close to the onset of the AFM order. In  $\text{EuAl}_4$ , at  $T < T_N$ ,  $\lambda_L$  is hundreds of times larger than in  $\text{EuGa}_4$ , thus suggesting much stronger spin fluctuations in the AFM state of  $\text{EuAl}_4$  than in  $\text{EuGa}_4$ . Conversely, in the PM state, both  $\text{EuAl}_4$  and  $\text{EuGa}_4$  exhibit similar  $\lambda_L$  values, i.e., comparable spin fluctuations at  $T > T_N$ .

The vigorous spin fluctuations in both crystals are further reflected in the LF- $\mu$ SR data (figure 29). Over a wide temperature range, the  $\mu$ SR spectrum in a  $\sim 0.8$ -T longitudinal field is mostly identical to that collected at zero field. This invariance suggests that, in  $\text{EuAl}_4$  and  $\text{EuGa}_4$ , the muon spins cannot be decoupled by the field and, hence, that spin fluctuations survive even in a field close to 1 T. Most interestingly, the muon spins cannot be decoupled not only in the AFM, but also in the PM state. Hence, in these materials, spin fluctuations persist well above the AFM transition. The strong spin fluctuations revealed by both ZF- $\mu$ SR and LF- $\mu$ SR might be crucial for understanding the origin of the topological Hall effect and of the magnetic skyrmions in  $\text{EuAl}_4$  and  $\text{EuGa}_4$ .

We briefly mention here that the  $\mu$ SR technique can also be used to investigate the magnetic skyrmions. Since most of the skyrmion phases appear in a field range not easily accessible by standard  $\mu$ SR instruments, to date, only a handful of results have been reported, where LF- $\mu$ SR is used to study skyrmion-hosting compounds. These include  $\text{GaV}_4(\text{S},\text{Se})_8$  [141],  $\text{Cu}_2\text{OSeO}_3$  [142], and the Co-Zn-Mn alloy [39, 142], whose skyrmion phases are stabilized by a relatively small field ( $< 0.1$  T). At the same time, in many newly discovered skyrmion-hosting systems, such as  $\text{GdRu}_2\text{Si}_2$ ,  $\text{Gd}_3\text{Ru}_4\text{Al}_{12}$ , or the  $\text{EuAl}_4$  and  $\text{EuGa}_4$  studied here, [33, 34, 47, 111], the critical field required to stabilize the skyrmion phase is larger than 1 T. By using transverse-field  $\mu$ SR in  $\text{GdRu}_2\text{Si}_2$ , with fields applied either along the  $c$ - or the  $a$ -axis, Huddart *et al.* found that the magnetic phases can be distinguished via their different muon response, thus providing additional evidence for the skyrmion and meron-lattice phases [143]. The muon-spin relaxation rates extracted from LF- $\mu$ SR measurements in the skyrmion phases of  $\text{Cu}_2\text{OSeO}_3$  and  $\text{GaV}_4(\text{S},\text{Se})_8$  are  $\sim 0.2$ – $0.8 \mu\text{s}^{-1}$ , similar to those of  $\text{Eu}(\text{Al},\text{Ga})_4$  (figure 28). All these skyrmion compounds exhibit similar temperature-dependent muon-spin relaxation rates  $\lambda_L(T)$ , with an enhanced and broadened peak in  $\lambda_L(T)$  at temperatures just below the critical temperature. Since also in longitudinal magnetic fields the muon-spin relaxation rate increases upon entering the skyrmion phase, this provides another method for identifying the magnetic skyrmions. In  $\text{EuAl}_4$  and  $\text{EuGa}_4$ , which host no skyrmion phase in

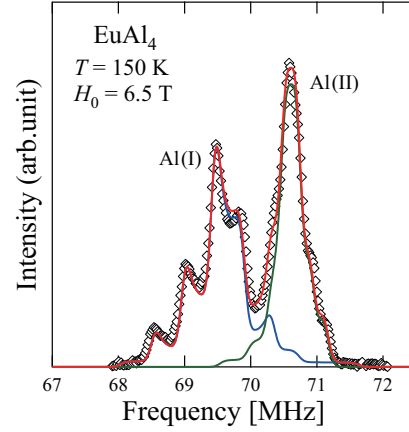


**Figure 30.**  $^{27}\text{Al}$  NMR spectra for the Al(I) and Al(II) sites in  $\text{EuAl}_4$  at 150 K. The solid lines are theoretical fits accounting for the quadrupole interactions of the Al nuclei. Figure was reproduced from Ref. [144].

zero field, the relaxation rates diverge at  $T_N$ , followed by a significant drop at  $T < T_N$ . Such drop is due to the slowing down of spin fluctuations, a typical feature of the magnetically ordered materials. A similar behavior is observed in  $\text{Co}_{10}\text{Zn}_{10}$  [142], a parent compound of the Co-Mn-Zn alloys, which lacks any skyrmion phases. According to magnetic-, transport- and neutron measurements (see sections 3 and 4), the skyrmion phase exists in a field range  $\sim 1$ – $2.5$  T in  $\text{EuAl}_4$  and  $\sim 4$ – $7$  T in  $\text{EuGa}_4$ . Further temperature-dependent  $\mu$ SR measurements at high magnetic fields would be an interesting pursue.

## 6. Nuclear magnetic resonance

In view of the complementarity of NMR to  $\mu$ SR regarding the time scale, probe site, and/or spin, NMR has successfully been used to investigate the intermetallic  $\text{Eu}(\text{Al},\text{Ga})_4$  compounds and their equivalents. Below we review briefly the main outcome of such studies, with particular regard to the magnetic and electronic properties.

The nucleus of choice in these studies was the spin- $5/2$   $^{27}\text{Al}$ . Although more demanding, also  $^{153}\text{Eu}$  ( $I = 5/2$ ) and  $^{69,71}\text{Ga}$  ( $I = 3/2$ ) have been used. Since all these nuclei have  $I > 1/2$ , their nonzero quadrupole interactions provide complementary information to  $\mu$ SR. Further, since the Al (Ga) atoms occupy two crystallographically inequivalent sites in the  $\text{BaAl}_4$ -type structure (i.e., 4d and 4e in Table 1), in principle, they can give rise to two distinct sets of NMR lineshapes.

In metallic alloys containing magnetic ( $\text{Eu}^{2+}$ ) ions embedded in a metallic (Al) matrix, the electronic properties are often determined by the physics of the RKKY oscillations [145–147]. Essentially, these are the spin-density equivalent of charge-density (Friedel) oscillations [148]. Both phenomena reflect the fact that an electric (magnetic) impurity in a metal is asymptotically screened in a non-exponential oscillatory

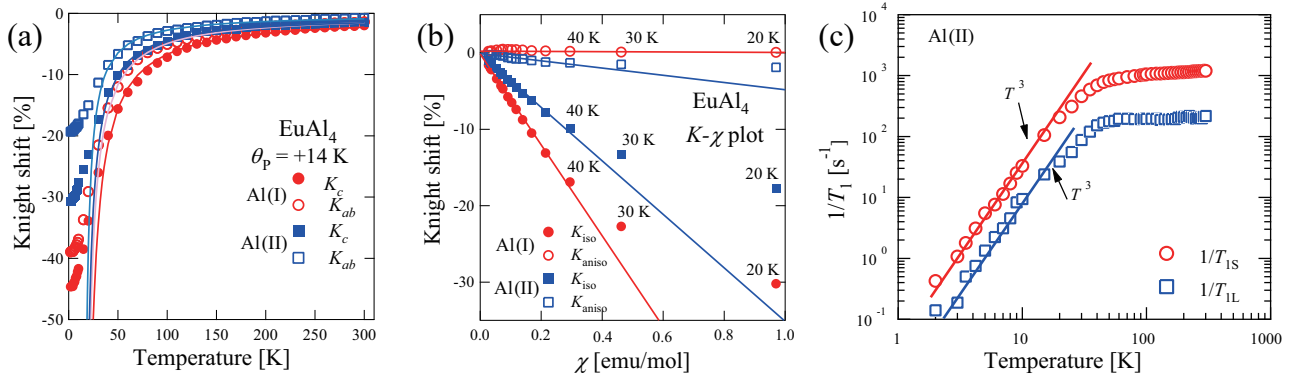


**Figure 31.** (a) Temperature dependence of the  $^{27}\text{Al}$  Knight shifts  $K_{\text{iso}}$  and  $K_{\text{aniso}}$  at the Al(I) and Al(II) sites in  $\text{EuAl}_4$ . (b)  $K$ - $\chi$  plots of  $^{27}\text{Al}$  Knight shifts. The resulting hyperfine fields  $H_{\text{iso}}^{\text{hf}}$  and  $H_{\text{aniso}}^{\text{hf}}$  are  $-3.23$  and  $-0.16$   $\text{kOe}/\mu_B$  at Al(I) site, and  $-1.82$  and  $-0.264$   $\text{kOe}/\mu_B$  at Al(II) site. (c) Temperature dependence of  $1/T_1$  of  $^{27}\text{Al}$  NMR in  $\text{EuAl}_4$  for the Al(II) sites [Al(I) sites show a similar behavior]. Figures were reproduced from Ref. [144].

way, i.e.,  $\delta\rho(r) \sim A_0 \cos(2k_F r)/r^3$ . The oscillation period is determined by the Fermi surface of the host material (here, by the Fermi wave vector  $k_F$ ), whereas the decay rate with distance  $r$  depends on the dimensionality of the host material (here,  $1/r^3$  for 3D materials). The oscillations themselves arise because only electrons within a limited range of wavelengths near the Fermi level can be scattered, thus producing a ripple-like modulation in the electronic density. As we show below, the RKKY effects are clearly reflected in the Knight shift and are so important as to overshadow a possible CDW order. The latter could still be successfully tracked from the quadrupole effects in the isostructural nonmagnetic  $\text{SrAl}_4$  compound.

The pioneering  $^{27}\text{Al}$  NMR study by van Diepen *et al.* on  $\text{EuAl}_4$  in powder form could detect only one broad resonance with a negative Knight shift [149]. Since  $\text{EuAl}_4$  is marginally stable and a proper annealing is problematic (due to the high vapor pressure of Eu), this hinted at lattice imperfections. Hence, the two expected resonance lines merged into one due to broadening from magnetic dipole and nuclear quadrupole interactions. In fact, recent studies by Niki *et al.* found two sets of resonances, including their quadrupole satellites (figure 30) [144]. The importance of the early studies (confirmed by the new ones) was to demonstrate the presence of RKKY effects via the nonequivalence of  $^{27}\text{Al}$  NMR lines. Here, the exchange interaction between the  $\text{Eu}^{2+}$  rare-earth spins and the Al conduction-electron spins, implies that the nonuniform oscillations of magnetism affect also the polarization of conduction electrons. In the absence of a polarizing rare-earth moment (i.e., for Pauli paramagnets), the different resonance lines would have the same Knight shift  $K_0$  and overlap, as indeed observed in the  $\text{La}_3\text{Al}_{11}$  case.

More in detail, the reported  $^{27}\text{Al}$  NMR spectra arise from the nuclear spin Hamiltonian:

$$\mathcal{H} = -\gamma_n \hbar \mathbf{I} \cdot \mathbf{H}_0 [1 + K(\theta)] + \frac{\hbar \nu_Q}{6} [3I_z^2 - I^2]. \quad (1)$$

Here, the first term represents the Zeeman interaction

between the nuclear magnetic moment  $\boldsymbol{\mu}_n = \gamma_n \hbar \mathbf{I}$  and the external magnetic field  $\mathbf{H}_0$ , where  $\gamma_n$  is the nuclear gyromagnetic ratio and  $\mathbf{I}$  is the nuclear spin. The internal magnetic field introduces the Knight shift term  $K(\theta)$ . The second term indicates the nuclear quadrupole interaction between the electric field gradient (EFG) and the nuclear quadrupole moment  $Q$ . For symmetry reasons, the EFG is along the main principal axis. Hence,  $V_{zz}$  is parallel to the  $c$ -axis and  $\nu_Q$ , the nuclear quadrupole frequency, is  $\nu_Q = 3eQV_{zz}/2I(2I-1)\hbar$ . Similarly, in the case of a tetragonal symmetry, the Knight shift is only a function of  $\theta$ , here corresponding to the angle between the external magnetic field and the  $c$ -axis. The calculated  $\nu_Q$  values of  $^{27}\text{Al}$  in  $\text{EuAl}_4$  are in good agreement with the measured ones, 0.865 and 0.409 MHz, assigned to the Al(I) and Al(II) sites and are almost independent of  $T$ .

The isotropic-  $K_{\text{iso}}$  and the anisotropic part  $K_{\text{aniso}}$  of the Knight shift for both Al sites measured at 6.5 T are summarized in figure 31(a) [144]. Upon decreasing the temperature, both shifts become strongly negative and follow a Curie-Weiss law with  $\theta_p = 14$  K. This is consistent with the magnetic susceptibility and reflects the FM state of  $\text{EuAl}_4$  above its metamagnetic transition at 2 T. Considering that the magnetic susceptibility  $\chi(T)$  in the PM state is isotropic, the Knight shift can be expressed as  $K = H_{\text{hf}} \chi(T)/N \mu_B$ , where  $H_{\text{hf}}$  is the hyperfine field,  $N$  is the Avogadro's number, and  $\mu_B$  the Bohr magneton. The  $K$ - $\chi$  plots for  $K_{\text{iso}}$  and  $K_{\text{aniso}}$  for both Al sites are shown in figure 31(b). From the relevant slopes one obtains the hyperfine field values reported in the figure caption.

The  $^{27}\text{Al}$  NMR spin-lattice relaxation times  $T_1$  reflect both the magnetic- and the nuclear quadrupole interactions. The latter arise because of the spin-5/2 Al nucleus and the tetragonal symmetry of  $\text{EuAl}_4$ . The recovery of nuclear magnetization for the central transition can be analyzed by means of standard expressions [150], slightly modified because  $T_1$  is distributed. In this case, the two components of the

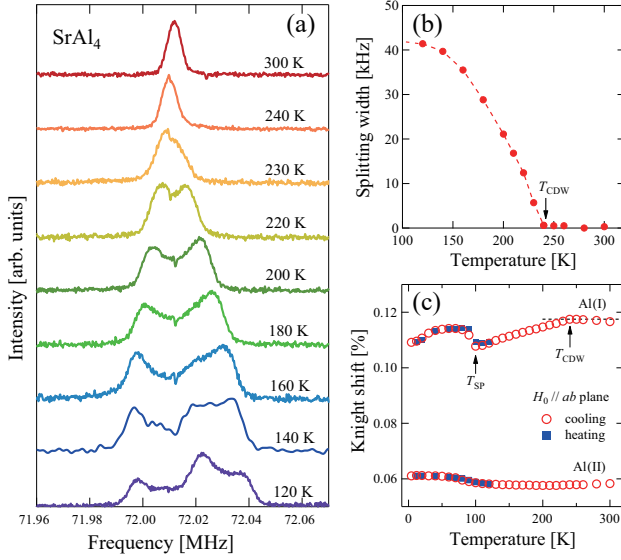


**Figure 32.** (a) Temperature dependence of the first low-frequency satellite line of the  $^{27}\text{Al}$  NMR spectrum for the Al(II) site in a single crystal of  $\text{SrAl}_4$ . (b) Splitting between peaks vs temperature for the data shown in panel (a). The disappearance of splitting corresponds to  $T_{\text{CDW}}$ . (c) Knight shift vs temperature for the Al(I) and Al(II) sites. In the first case, the core polarization of  $d$ -electrons dominates the shifts, here reflected in the clear changes at  $T_{\text{CDW}}$  and  $T_{\text{SP}}$  (see text for details). Figures were reproduced from Ref. [151].

relaxation, a short one  $1/T_{1\text{S}}$  and a long one  $1/T_{1\text{L}}$ , are shown in figure 31(c). Due to the fast fluctuation of the  $f$ -electron spins in the PM state, the relaxation rate is almost constant close to 300 K, but it gradually decreases with decreasing temperature because of the slowdown of fluctuations. Below 20 K,  $1/T_1$  is almost proportional to  $T^3$ , a behavior attributed to the excitation of the  $f$ -electron spins in the FM state (where the NMR measurements, here at 6.5 T, were performed). Note that, no change in the  $^{27}\text{Al}$  NMR relaxation due to the CDW around 140 K could be detected, most likely because of its masking by the fast relaxation due to the large magnetic moments of  $f$ -electron spins.

To investigate the physical properties of the CDW and the structural phase (SP) transitions in  $\text{EuAl}_4$ ,  $^{27}\text{Al}$  NMR measurements were performed in the isostructural nonmagnetic  $\text{SrAl}_4$  compound [151]. By applying the magnetic field perpendicular to the  $c$ -axis one obtains a 10-peak NMR dataset, comprising five lines for each of the two Al sites. Because of the CDW and SP transitions (at 243 and 100 K, respectively), the well resolved sharp spectra at 300 K become complex at 4 K. The evolution of the  $^{27}\text{Al}$  NMR lines with temperature can be followed by monitoring the first satellite of the Al(II) site. Below  $T_{\text{CDW}}$ , the single resonance line splits into a double-horned shape [figure 32(a)], reflecting the modulation of the electrical quadrupole interaction by the incommensurate CDW charge distribution. The temperature dependence of the spectral splitting, here corresponding to the CDW

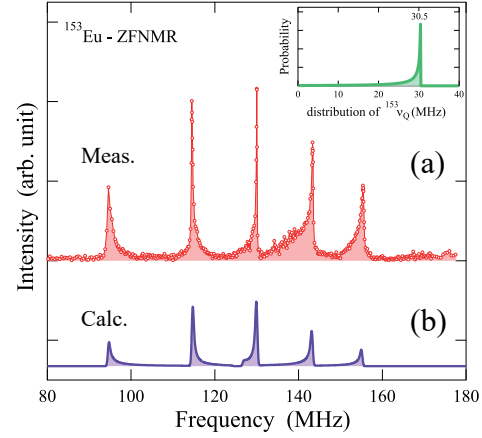


**Figure 33.** (a)  $^{153}\text{Eu}$  zero-field NMR spectrum at  $T = 4.2$  K. (b) Calculated spectrum for  $H_{\text{int}}^{\text{Eu}} \perp V_{zz}^{\text{Eu}}$  assuming a log-normal distribution of  $^{153}\nu_Q$  frequencies, as shown in the inset. The five peaks reflect the  $I = 5/2$   $^{153}\text{Eu}$  nucleus. Figure was reproduced from Ref. [152].

amplitude, is summarized in figure 32(b). The splitting develops rapidly below  $T_{\text{CDW}}$ , to become constant around 140 K. Further spectral changes were observed below 120 K, preliminary to the  $T_{\text{SP}}$  transition at 100 K, with the simple incommensurate CDW above  $T_{\text{SP}}$  changing into a different type of charge modulation below it.

The temperature dependence of the  $^{27}\text{Al}$  NMR Knight shifts for both Al sites in  $\text{SrAl}_4$  is summarized in figure 32(c). In the Al(I) case, while above  $T_{\text{CDW}}$  the Knight shift is almost constant, it decreases monotonously below  $T_{\text{CDW}}$ , to show a step-like anomaly at  $T_{\text{SP}}$ . The Knight shift for the Al(II) site remains almost constant from room temperature to  $T_{\text{SP}}$ , to increase smoothly below it. The dependency of shift with temperature for the site Al(I) can be attributed to the core polarization of the  $d$ -electrons, while its mostly constant value for the site Al(II) is compatible with a contribution from the  $s$ -electrons. Such attribution is reflected also in the  $^{27}\text{Al}$  NMR spin-lattice relaxation times  $T_1$  (not shown), where the relaxation vs temperature for each site follows closely that of the shifts.

Since the relaxation time of the rare-earth nuclei (especially in the fast fluctuating PM phase) is too short to detect an NMR signal, the only possibility to observe these nuclei is in the magnetically ordered state. For instance, the zero-field  $^{153}\text{Eu}$  NMR signal could be observed in the AFM state of  $\text{EuGa}_4$  [152]. In this case, a large internal field is transferred to the nuclei from the adjacent magnetic moments, producing a Zeeman splitting of the nuclear spin states, thus giving rise to an NMR signal even in a zero magnetic field. The hyperfine interaction Hamiltonian is again given by equation (1), where  $H_0$  is replaced by  $H_{\text{int}}$ . If  $H_{\text{int}} \parallel V_{zz}$  and the Zeeman interaction is larger than the nuclear quadrupole interaction, the five  $^{153}\text{Eu}$  peaks are equidistant. On the other hand, if  $H_{\text{int}} \perp V_{zz}$ , the peak separations

become inequivalent, consistent with the observed  $^{153}\text{Eu}$  NMR spectrum (figure 33), indicating ordered magnetic moments lying in the  $ab$ -plane [see figure 20(c)]. This result is in good agreement with those of magnetic susceptibility and neutron diffraction experiments (see details in sections 3 and 4).

In  $\text{EuGa}_4$ , calculations based on the exact diagonalization of the nuclear-spin Hamiltonian provide an internal field at the Eu nucleus  $H_{\text{int}}^{\text{Eu}} = 27.08$  T and  $^{153}\nu_Q = 30.5$  MHz [152]. The very large field at the Eu nucleus suggests an  $f$ -electron-derived magnetic state. Analogous results were found also for  $^{69,71}\text{Ga}$  NMR, where the three-peak spectra reflect the  $I = 3/2$  of both Ga isotopes. In this case, the internal field is  $H_{\text{int}}^{\text{Ga}} = 3.03$  T and  $^{69}\nu_Q(^{71}\nu_Q) = 5.08(3.21)$  MHz [152]. Finally, the temperature dependence of the internal field, which in AFM materials is proportional to the sublattice magnetization, can be explained by a Brillouin function with  $J = S = 7/2$ , here reflecting the magnetic moment of the  $\text{Eu}^{2+} 4f^7$  ions.

Recently, zero-field  $^{153}\text{Eu}$ -NMR studies were performed also in the AFM state of  $\text{EuAl}_4$  [154]. Unlike in  $\text{EuGa}_4$ , whose Eu NMR spectra consists of five resonance lines (a main line and two satellites on each side), the  $^{153}\text{Eu}$  spectra of  $\text{EuAl}_4$  show 10 lines, reflecting the presence of two kinds of  $\text{Eu}^{2+}$  magnetic moments, oriented either along the  $c$ -axis or perpendicular to it. Since the signal intensities of the  $^{153}\text{Eu}$  ZF-spectra produced by the two orientations are comparable, similar numbers of magnetic moments belong to each orientation. The internal magnetic field at the  $^{153}\text{Eu}$  nucleus is  $H_{\text{int}}^{\text{Eu}} = 28.41$  T and  $^{153}\nu_Q = 27.0$  MHz for magnetic moments parallel to the  $c$ -axis, and  $H_{\text{int}}^{\text{Eu}} = 28.11$  T and  $^{153}\nu_Q = 27.6$  MHz for those perpendicular to the  $c$ -axis [154]. Thus, also the amplitudes and NQR frequencies of the magnetic moments lying along the two directions are almost the same.

Finally, we recall that electron spin resonance (ESR) measurements in  $\text{EuAl}_4$  were performed already in the 1970's [155, 156]. These studies provide a  $g$  value of 2.000(5) between 77 and 300 K and a room temperature linewidth of 55(2) mT. Below 40 K (corresponding to about  $2 T_N$ ), the ESR line moves down in frequency and broadens up to 150 mT. Both effects are compatible with materials that order antiferromagnetically, for which the resonant field is expected to shift by a factor of  $(2H_E H_A)^{1/2}$ , where  $H_E$  is the exchange field and  $H_A$  the anisotropy field, if  $H_E \gg H_A$ . This shift is so large that, below the Néel temperature, the resonance drops outside the microwave frequency range and no signal is observed. The line shape remains asymmetric over the entire temperature range, a behavior attributed to the fact that  $\text{EuAl}_4$  undergoes a metamagnetic transition just above the resonant field.

## 7. Optical spectroscopy

As discussed in sections 3 and 4, the magnetic order can be easily tuned in  $\text{EuAl}_4$ . Here, a weak magnetic field ( $< 2$  T) can rotate the  $\text{Eu}^{2+}$  spins, leading to a series of non-coplanar spin textures (including skyrmions) and the corresponding topological Hall effect [47, 48]. These phenomena are unusual, since most of the non-coplanar spin textures occur in materials with a noncentrosymmetric crystal structure (due to the presence of DMIs [157]), while  $\text{EuAl}_4$  has a centrosymmetric tetragonal structure. By contrast, the magnetic order in  $\text{EuGa}_4$  is quite robust. It undergoes only one AFM transition at low temperature, and magnetic fields up to 7 T cannot rotate the spin at 2 K [111]. The two compounds exhibit the same crystal structure and share similar band structures. While  $\text{EuAl}_4$  undergoes a CDW transition around 145 K (see section 2),  $\text{EuGa}_4$  behaves as a simple metal in the PM state. The magnetism of the rare-earth metallic compounds is mostly dominated by the local moments of  $4f$  electrons. Nevertheless, the charge excitations, including itinerant carriers and local excitations, play a key role in mediating the magnetic interactions. Thus, understanding the effects of CDW order on the band structures provides important clues on the mechanisms behind the complex magnetism of  $\text{EuAl}_4$ .

Optical spectroscopy represents one of the most powerful tools for investigating the charge excitations in solids [158], able to provide information on electronic gaps and band reconstructions. Recently, Yang *et al.* conducted a comparative study of  $\text{EuAl}_4$  vs.  $\text{EuGa}_4$ , to elucidate the effects of CDW order on the electronic band structures by means of optical spectroscopy and first-principles calculations [153]. The reflectivities of  $\text{EuAl}_4$  and  $\text{EuGa}_4$  were measured from 10 meV to 3 eV, at temperatures below and above  $T_{\text{CDW}}$  [figures 34(a)-(b)]. Based on the Kramers-Kronig relation, the optical conductivity  $\sigma_1(\omega)$  of both compounds was calculated [figures 34(c)-(d)]. Optical conductivity is proportional to the joint density of states [158]. Peaks centered at zero frequency represent the intraband response (Drude peak), while the Lorentz peaks, centered at finite frequencies, come from the interband excitations. Below  $T_{\text{CDW}}$ , the intraband response of  $\text{EuAl}_4$  is greatly suppressed. The two interband absorptions, emerging close to 0.1 and 0.4 eV, indicate the opening of a CDW gap at the Fermi surface and an enhanced local excitation at 0.4 eV [shown by red- and green arrows in figures 34(a)-(e)]. In  $\text{EuAl}_4$ , the residual intraband response below  $T_{\text{CDW}}$  confirms the partial gap opening at the Fermi surface. A spectral weight analysis of the optical conductivity indicates that, below the CDW transition, part of the itinerant carriers become localized [figure 34(f)]. By contrast, the above features are absent in the optical conductivity of  $\text{EuGa}_4$ .

When entering the AFM state, the  $\text{Eu}^{2+}$  moments



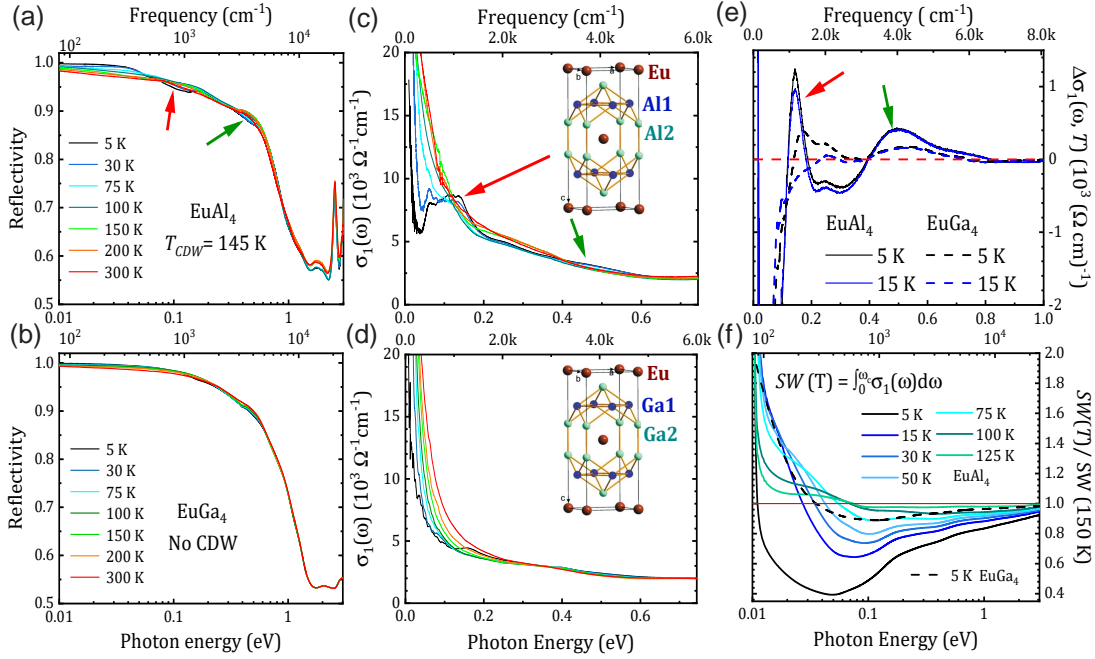


**Figure 34.** Optical spectroscopy of  $\text{EuAl}_4$  and  $\text{EuGa}_4$ . Temperature-dependent reflectivity of (a)  $\text{EuAl}_4$  and (b)  $\text{EuGa}_4$  with the light polarized in the  $ab$ -plane. Temperature evolution of the real part  $\sigma_1(\omega; T)$  of the optical-conductivity spectra of  $\text{EuAl}_4$  (c) and  $\text{EuGa}_4$  (d) below  $6000 \text{ cm}^{-1}$  ( $0.74 \text{ eV}$ ). Insets display the lattice structures of  $\text{EuAl}_4$  and  $\text{EuGa}_4$ , with the two inequivalent Al/Ga atoms. (e) Difference spectra of  $\sigma_1(\omega)$  below the CDW order calculated via  $\Delta\sigma_1(\omega, T) = \sigma_1(\omega, T) - \sigma_1(\omega, 150 \text{ K})$  for  $\text{EuAl}_4$  (solid lines) and  $\text{EuGa}_4$  (dashed lines), respectively. (f) The normalized integrated spectral weight ( $SW$ ) of  $\text{EuAl}_4$  as a function of the cutoff frequency  $\omega_c$  at  $T < T_{\text{CDW}}$ . Figures were reproduced from Ref. [153].

in  $\text{EuAl}_4$  can be tuned by an external magnetic field. For instance, at  $8 \text{ K}$ , the absorption around  $0.4 \text{ eV}$  is steadily enhanced and starts to saturate at  $H > 3 \text{ T}$ , where the  $\text{Eu}^{2+}$  moments are polarized (figure 35). To understand the origin of absorption at  $0.4 \text{ eV}$ , Yang *et al.* calculated the band structure and the optical conductivity of  $\text{EuAl}_4$  (figure 35). The resulting optical conductivities in the PM- and in the polarized FM state ( $\text{Eu}^{2+}$  moments aligned along the  $c$ -axis) are in good agreement with the experimental data [figure 35(e)]. A slight difference in the energy scale was attributed to the electron correlation, which was not included in the first-principle calculations. Considering the energy size and the possible excitations near the Fermi level, the absorption at  $0.1 \text{ eV}$  can be ascribed to the excitations between the linear bands near the Fermi level [orange arrows in figures 35(c)-(d) and orange segment in figure 35(e)], while the absorption at  $0.4 \text{ eV}$  arises mainly from the excitations between the  $\text{Eu-5d-}$  and  $\text{Al-4p}$  bands [green arrows in figures 35(c)-(d) and green segment figure 35(e)]. The increased absorption at  $0.4 \text{ eV}$  in a magnetic field could be ascribed to the Zeeman splitting from the aligned local moments.

By combining optical spectroscopy with first-principle calculations, Yang *et al.* found that the CDW order in  $\text{EuAl}_4$  leads to a partial deformation of the Fermi surface, while simultaneously amplifying local excitation around  $0.4 \text{ eV}$ . In rare-earth metallic systems, the magnetic interactions are mainly mediated by itinerant carriers through the

RKKY interactions. In the CDW ordered state, since part of the itinerant carriers are localized, the AFM interactions are frustrated. Moreover, below  $T_{\text{CDW}}$ , the excitations between the  $\text{Eu-5d-}$  and  $\text{Al-3p}$  orbitals are enhanced. A previous study of  $\text{Eu}$  monochalcogenides pointed out that the hybridization between  $\text{Eu-5d}$  and  $p$  orbitals is essential to the magnetic interactions, which can be either AFM or FM [159, 160]. In  $\text{EuAl}_4$ , recent  $\mu\text{SR}$  and NMR studies reveal robust magnetic fluctuations even in the magnetically ordered state [50, 161], while they are absent in  $\text{EuGa}_4$ . In  $\text{SrAl}_4$ , recent optical investigations also reveal an enhanced absorption around  $0.4 \text{ eV}$  along with an amplified FM response below the CDW transition [72]. Since  $\text{EuAl}_4$  and  $\text{SrAl}_4$  share similar band structures, in both cases the amplified  $p$ - $d$  hybridization can promote FM interactions [figure 35(f)]. Therefore, Yang *et al.* proposed that the CDW order in  $\text{EuAl}_4$  could suppress the AFM interactions, but promote the FM ones. Since such interactions compete with each other, when they become of comparable intensity, it may result in a magnetic instability and lead to a variety of magnetic orders. At the same time, in  $\text{EuGa}_4$ , there is no CDW order at ambient pressure. Hence, its AFM order is relatively robust. This is also demonstrated by doping studies in  $\text{Eu}(\text{Al}_{1-x}\text{Ga}_x)_4$ . When the CDW order is suppressed upon Ga-doping, less magnetic transitions are found [89].

Moreover, since the CDW gap is partially opened on the Fermi surface, the AFM interactions mediated by the

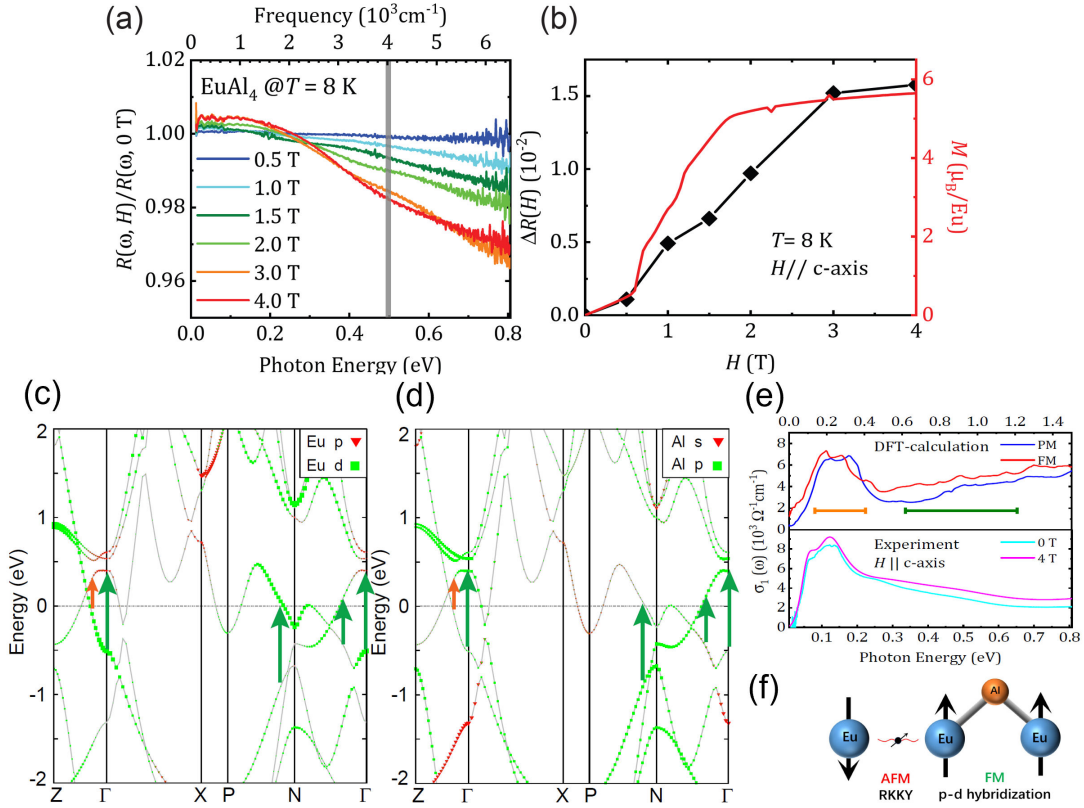


**Figure 35.** Magneto-optical response and first-principle calculations of  $\text{EuAl}_4$ . (a) Normalized magneto-optical reflectivity spectra  $R(\omega, H)$  measured at 8 K in a magnetic field up to 4 T, applied along the  $c$ -axis. (b) Comparison between the field-dependent reflectivity change  $\Delta R(H) = [1 - R(H)/R(0T)]$  at 0.4 eV [indicated by the gray bar in panel (a)] and the magnetization at  $T = 8$  K. Band structure of  $\text{EuAl}_4$  in the PM state (without considering the CDW order), with the contributions of the Eu-5d and Al-3p orbitals shown in panels (c) and (d), respectively. The upper- and lower panels in (e) show the calculated and the measured interband optical conductivities. Blue and red lines in the upper panel correspond to the absorption in the PM- and FM state (where the  $\text{Eu}^{2+}$  moments align along the  $c$ -axis). The turquoise and pink lines in the lower panel are conductivities measured at 8 K in 0 and 8 T. Orange and green segments represent the interband transitions, denoted by same-colour arrows in panels (c) and (d). (f) Schematic plot of the magnetic interactions in  $\text{EuAl}_4$ . Figures reproduced from Ref. [153].

itinerant electrons are anisotropic. The incommensurate lattice distortion below  $T_{\text{CDW}}$  breaks the inversion symmetry [105, 162], which may split the degenerate Dirac bands into Weyl bands [163, 164]. In such an anisotropic environment, itinerant electrons from the Weyl bands can mediate the anisotropic magnetic interactions that facilitate the formation of the chiral spin textures [48, 104, 165]. Further experimental investigations are needed to validate this hypothesis.

## 8. Angle-resolved photoemission spectroscopy and quantum oscillations

As mentioned in section 3, transport studies reveal topological features in both the real- and momentum space of the  $\text{Eu}(\text{Al},\text{Ga})_4$  system. In this section, we briefly review the theoretical and experimental work in the search for topological features in the electronic band structure (i.e., momentum space) that allowed the identification of Weyl nodal rings (NR) in the spin-polarized (i.e., field-in-

duced FM) state of  $\text{EuGa}_4$ , which also provided a tentative explanation for the large MR in this regime [73].

Density-functional theory (DFT) suggests that the electronic band structures of square-lattice compounds—to which  $\text{EuAl}_4$  and  $\text{EuGa}_4$  belong—feature diamond-shaped NRs in the mirror-invariant plane [figure 36(a)]. When ferromagnetism is introduced to account for the spin-polarized (SP) state, the lifting of spin degeneracy promotes four spinful NRs to emerge from the single spinless NR at zero field, each NR now being twofold degenerate. After considering the spin-orbit coupling (SOC), only a subset of these spinful NRs protected by mirror symmetry survive, while the others are gapped out. In the PM state of  $\text{EuGa}_4$ , the electronic bands show multiple crossings [figure 36(b)]. Among them, most of those on the mirror invariant planes, at  $k_x = 0$  and  $k_z = 2\pi/c$ , exhibit NR geometry in the three-dimensional (3D)  $k$ -space. Upon entering the SP state, two sets of spin-split bands form. After further introducing the SOC and setting the magnetization along the  $c$ -axis (i.e.,  $m \parallel c$ ), in

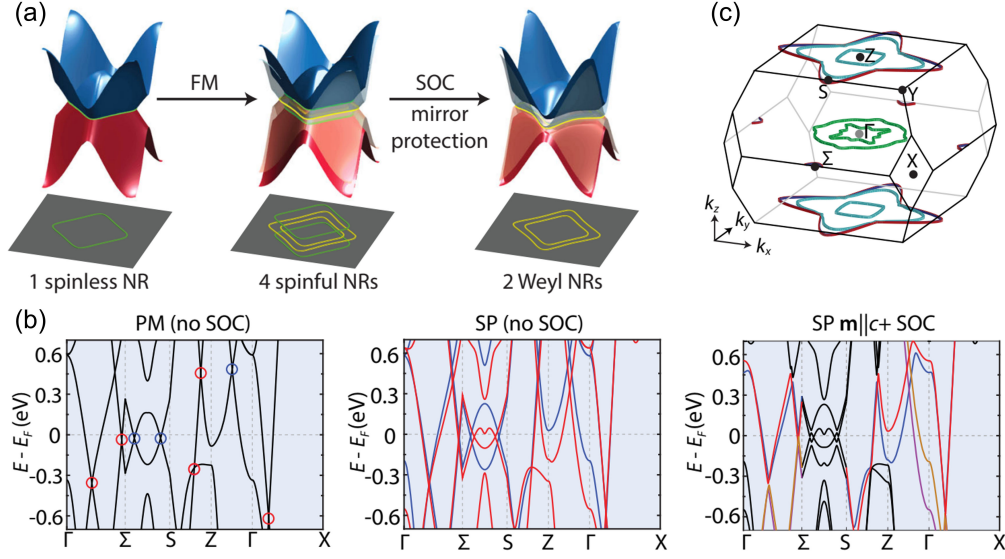


**Figure 36.** Calculated electronic band structures for  $\text{EuGa}_4$ . (a) The mechanism of formation of Weyl node rings in a square lattice. (b) Band structures of  $\text{EuGa}_4$  in the PM state without SOC, SP phase without SOC, and SP phase with magnetic moment along  $c$  axis and with SOC, respectively. (c) 3D view of the Weyl NRs. Three pairs of NRs are shown in green, cyan, and red/blue, respectively. Figures were reproduced from Ref. [73].

this case perpendicular to the mirror plane, only a subset of the crossings are retained, forming the Weyl NRs. These calculated Weyl NRs can be categorized into three pairs, colored green, cyan, and red/blue in the Brillouin zone [figure 36(c)]. The red/blue pair of NRs are expected to sit very close to the Fermi energy  $E_F$ , with a small energy variation, although they span the whole Brillouin zone at the  $k_z = 2\pi/c$  planes.

Lei *et al.* performed angle-resolved photoemission spectroscopy measurements to identify the spinless NR states in the PM state of  $\text{EuGa}_4$ , which indeed confirmed the predicted spinless NRs [figure 37] [73]. Three groups of Fermi-surface (FS) pockets derived from the NR bands, labeled  $\alpha$ ,  $\beta$ , and  $\gamma$ , are summarized in figure 37(a). The FS cross-section measured at 25 K (PM state), with a photon energy roughly corresponding to the  $k_z = 0$  plane, is shown in figure 37(b). The inner- and outer portions of the  $\beta$  pocket manifest themselves as two concentric diamond rings centered around  $\Gamma$  (red dashed curves), while the outward warping geometry of the  $\beta$  pocket along  $k_z$  renders the intensity finite even outside the outer diamond (up to the yellow boundary) [figure 37(b)]. The NR2, with the overlaid orange lines showing its DFT calculated structure, has its node very close to  $E_F$  [figure 37(c)]. The suppressed spectral weight near  $E_F$  points to the existence of a small SOC-induced gap. The fact that the node of NR2 sits close to  $E_F$  along both cuts (path 1 and path 2) indicates the low dispersion of NR2 along the ring. These observations are consistent with the theoretical predictions for the PM state of  $\text{EuGa}_4$ .

Quantum-oscillation measurements provide more quantitative information about the band splitting and the

energy of the Weyl NR states. In the SP phase, there are also three groups of FS pockets, whose shapes are similar to those in the PM state, albeit they now appear in pairs due to the band splitting. The Shubnikov-de Haas oscillations, with the magnetic field rotating from the  $c$ - to the  $a$ -axis, are shown in figure 38(a), while the field-angle dependence of the corresponding frequencies is summarized in figure 38(b). At high frequencies, for  $H \parallel c$  (i.e.,  $\theta = 0^\circ$ ), four pairs of QO frequencies, labeled as  $\beta_{\text{in}}$ ,  $\beta_{\text{out}}$ ,  $\alpha_{\text{neck}}$ , and  $\alpha_{\text{belly}}$  can be identified. The two closely-lying frequencies are attributed to the spin-split bands. The field-angle dependence of the frequencies is consistent with the expected evolution of the extremal orbits on the  $\alpha$  and  $\beta$  FS pockets [figure 38(c)]. Specifically, upon increasing the field angle  $\theta$ , the  $\alpha$  frequencies merge at  $\theta \sim 20^\circ$ , while the  $\beta$  frequencies increase first, and then show a sudden drop at  $\theta \sim 30^\circ$ . The  $\alpha$  frequencies at small  $\theta$  can be attributed to slight corrugations of the  $\alpha$  pockets along the vertical axis, while the  $\beta_{\text{in}}$  and  $\beta_{\text{out}}$  frequencies are associated with the inner and outer cross-sectional areas of the torus-shaped  $\beta$  pockets. The sudden drop of the  $\beta$  frequencies with increasing  $\theta$  beyond a critical value corresponds to a change of the extremal cross-section from the in-and-out to the sideways pair [figure 38(c)]. The energy of the bands that give rise to the  $\beta_{\text{in}}$  oscillations shows an excellent match with the calculated value, while the calculated energies for the  $\beta_{\text{out}}$ ,  $\alpha_{\text{neck}}$ , and  $\alpha_{\text{belly}}$  oscillations are slightly off, allowing quantitative corrections to the calculated band structures.

The  $\gamma$  pockets are composed of a series of side-by-side electron and hole pockets along the red/blue Weyl NRs. The smallness of these pockets, ascribed

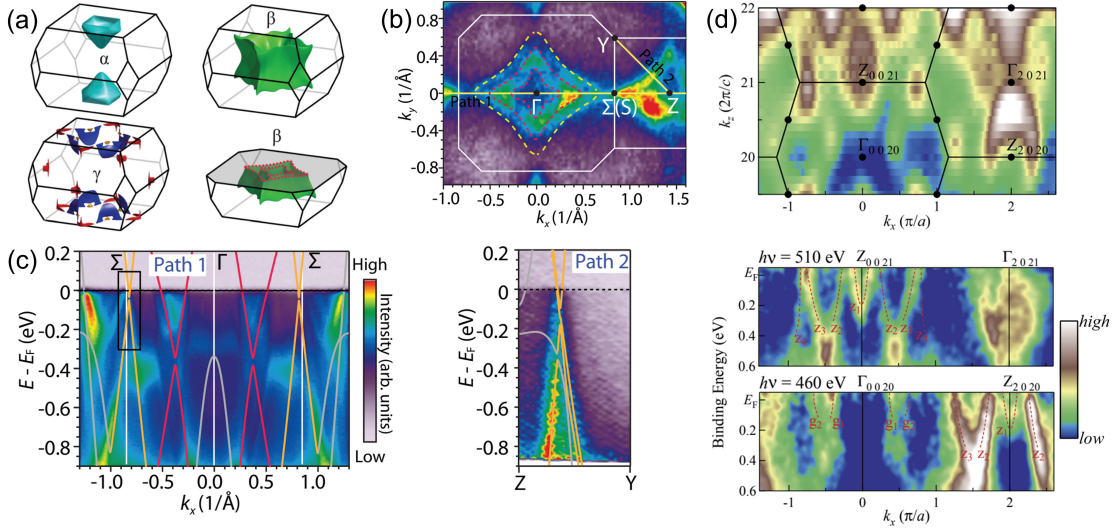


**Figure 37.** Electronic structure of  $\text{EuGa}_4$  in the PM phase measured by ARPES. (a) Three groups of FS pockets:  $\alpha$ ,  $\beta$ , and  $\gamma$ , based on DFT calculations. (b) Fermi surfaces with  $h\nu = 118$  eV at  $T = 25$  K. Two high-symmetry  $k$ -paths (yellow lines) are indicated for band dispersion analysis. Solid lines represent the calculated band structures. Red and orange lines indicate the bands that form the NR1 and NR2, respectively. (c) Band dispersion along path 1 and path 2 with  $h\nu = 120$  eV. (d) Fermi surface mappings and band structures of  $\text{EuAl}_4$  in the vicinity of  $E_F$ . Figures were reproduced from Ref. [73, 78].

to the closeness of the energy of the nodes to  $E_F$ , guarantees the low frequencies of QOs [figure 38(a)]. Of the four obtained frequency components,  $\gamma_1$  to  $\gamma_4$ ,  $\gamma_4$  is identified as the signature of the blue pocket [see inset in figure 38(b)]. The overall  $\theta$  dependence of  $\gamma_4$ —remaining nearly constant with increasing  $\theta$  and gradually bifurcating into two branches, and eventually merging into one observable frequency—is consistent with the DFT calculations. From the temperature-dependent QO amplitude, the effective masses of the  $\gamma_4$ ,  $\gamma_3$ , and  $\gamma_2$  components are estimated to be  $0.7m_e$ , where  $m_e$  is the free-electron mass, much higher than those of typical nonmagnetic topological semimetals, implying a sizable electronic correlation in  $\text{EuGa}_4$ . Furthermore, the corresponding quantum mobilities are estimated to be  $\sim 10^3 \text{ cm}^2/\text{Vs}$ , the highest in all known magnetic topological semimetals.

We also briefly mention that, prior to the work discussed above, the electronic structures of  $\text{EuAl}_4$  and  $\text{EuGa}_4$  were investigated by Nakamura *et al.* and Kobata *et al.* using QO and ARPES [75, 78, 79], with the aim to address the nesting conditions for the CDW order. The main results regarding  $\text{EuAl}_4$  are shown in figure 37(d) and 38(d). The spectra show a considerable dependence along the  $k_z$  direction, suggesting that the Fermi surfaces of  $\text{EuAl}_4$  have three-dimensional shapes [78]. Some dispersive features exist in the vicinity of  $E_F$ , but their details are not well resolved in the present ARPES spectra. Moreover, the Fermi surface of  $\text{EuAl}_4$  exhibits ellipsoidal features, which are completely different from those of  $\text{EuGa}_4$  [see figure 38(d)] [75]. In  $\text{EuGa}_4$ , the Fermi

surfaces determined by QO consist of a small ellipsoidal hole FS and a compensated cube-like electron FS, with a vacant space in the center. These Fermi surfaces were argued to favor a CDW order, although the CDW order appears in  $\text{EuGa}_4$  only under pressure. By contrast, the CDW order is present at ambient pressure in  $\text{EuAl}_4$ , the cube-like FS is absent at low temperatures due to FS reconstruction. It is worth mentioning that the effective masses obtained from QO measurements in these works are also in the order of tenths of the free-electron mass. The electronic structure of  $\text{EuAl}_4$  in the vicinity of  $E_F$  was determined by ARPES to be very similar to that of its nonmagnetic counterpart  $\text{SrAl}_4$ . The 3D nature of the electronic structure of  $\text{EuAl}_4$  was argued to disprove a simple FS nesting scenario as the origin of the CDW order.

## 9. Summary and outlook

In this review we discussed recent experimental investigations on  $\text{BaAl}_4$ -type  $\text{Eu}(\text{Al},\text{Ga})_4$  topological antiferromagnets.  $\text{Eu}(\text{Al},\text{Ga})_4$  compounds represent one of the rare classes, which exhibit exotic physical properties originating from both real- and momentum-space topological aspects. The electron- and charge orders coexist and compete, resulting in exotic and rich physical properties, e.g., superconductivity, topological Hall effect, giant MR, magnetic skyrmions, Weyl nodal rings, etc. Despite the numerous efforts aimed at understanding their origin, there are still some interesting open questions.

$\text{SrAl}_4$  undergoes a CDW and a structural phase transition at  $T_{\text{CDW}} \sim 243$  and  $T_S \sim 90$  K, respectively.

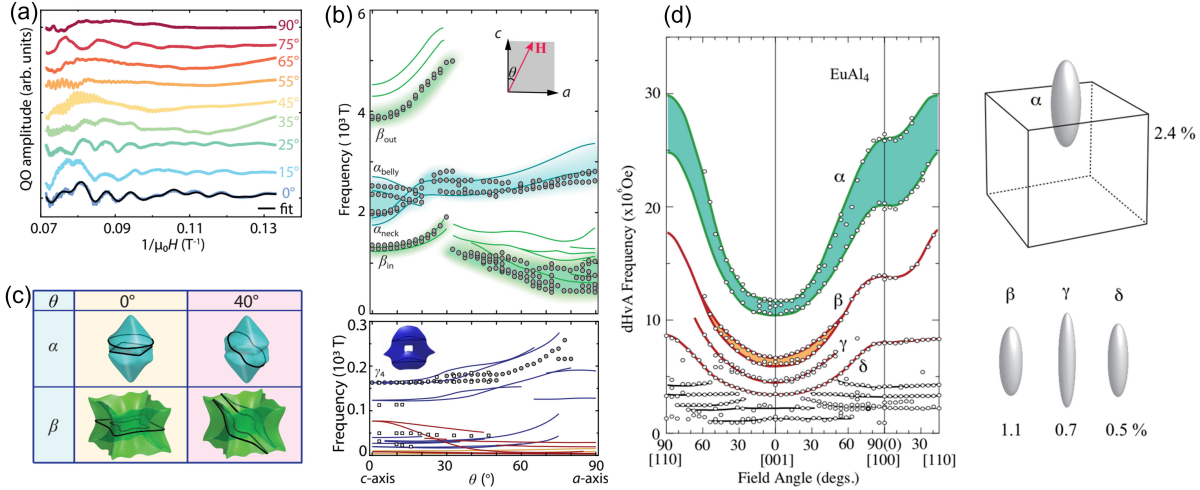


**Figure 38.** Fermi-surface geometry of  $\text{EuGa}_4$  in the SP phase built from QO measurements. (a) A series of QO curves with  $\theta$  ranging from  $0^\circ$  to  $90^\circ$ . The solid line is a Lifshitz–Kosevich fit. (b) Angle-dependent QO frequencies (circles) above and below 300 T. The cyan and green lines in the upper panel are theoretical predictions for the  $\alpha$  and  $\beta$  pockets, respectively. The red, blue, and orange lines in the lower panel represent the theoretical prediction for the  $\gamma$  pockets. The inset in the lower panel illustrates the extremal cyclotron orbits associated with the measured  $\gamma_4$  frequency at  $\theta = 0^\circ$ . (c) Illustration of the extremal orbits (black lines) for the  $\alpha$  and  $\beta$  pockets with  $\theta = 0^\circ$  and  $40^\circ$ . (d) Angular dependence of the QO frequency in  $\text{EuAl}_4$  and the corresponding Fermi surfaces. Figures were reproduced from Ref. [73, 75].

Both transitions are suppressed upon substituting Al with Si, and SC emerges below 3 K in  $\text{SrAl}_{4-x}\text{Si}_x$  ( $x \geq 1.5$ ). Although such superconductors have been investigated by magnetic-susceptibility and heat-capacity measurements, their properties at a microscopic level, in particular, the superconducting order parameter, require further investigation. Besides the CDW transition at  $T_{\text{CDW}} \sim 142$  K,  $\text{EuAl}_4$  exhibits multiple AFM orders below  $T_{\text{N}} \sim 15.6$  K, and undergoes a series of metamagnetic transitions in the AFM state. By applying pressure, the CDW order is linearly suppressed in both  $\text{SrAl}_4$  and  $\text{EuAl}_4$ , but the SC is absent near the critical pressure. Moreover, the substitution of Al with Ga also suppresses the CDW order in  $\text{Eu}(\text{Al}_{1-x}\text{Ga}_x)_4$ , but the AFM order remains robust against chemical pressure. These observations suggest that the charge- and AFM order compete with SC, and that carrier doping might be one of the keys to introduce SC in the  $\text{BaAl}_4$ -type materials. Electronic band-structure calculations of the electron-phonon coupling and the density of states could be useful to address this issue. In view of this,  $\text{Eu}_{1-x}\text{Ba}_x\text{Al}_4$  and  $\text{Eu}_{1-x}\text{Ba}_x\text{Ga}_4$  represent ideal systems to investigate the competing electronic orders and the quantum critical phenomena, and to search for possible unconventional SC. Furthermore, from the topological point of view, the non-trivial band topology of  $\text{BaAl}_4$  and  $\text{Eu}(\text{Al},\text{Ga})_4$  suggests that the  $\text{BaAl}_4$ -type materials also represent one of the ideal candidates to search for topological SC.

In  $\text{EuAl}_4$ , the observed topological Hall effect is attributed to the formation of a skyrmion lattice in an applied magnetic field along the  $c$ -axis ( $H \parallel c$ ), as confirmed by SANS measurements. Similar to  $\text{EuAl}_4$ ,

also  $\text{Eu}(\text{Al}_{1-x}\text{Ga}_x)_4$  ( $0.1 \leq x \leq 0.5$ ) and  $\text{EuGa}_4$  single crystals exhibit topological Hall resistivity  $\rho_{\text{xy}}^{\text{THE}}$  in a field range whose extension depends on Ga content. Though the same mechanism is expected to account for the THE in these crystals, the topological spin textures and their evolution with Ga content are not yet known. According to the Hall resistivity measured in an applied magnetic field perpendicular to the  $c$ -axis ( $H \parallel ab$ ) (section 3), the signature of topological contribution is clearly visible in  $\rho_{\text{xy}}(H)$ . However, due to significant multiband effects, it is rather difficult to isolate the  $\rho_{\text{xy}}^{\text{THE}}$  term. As an alternative approach, it could be interesting to check if the topological spin textures also form in an applied magnetic field perpendicular to the  $c$ -axis. Currently, neither neutron- nor resonant x-ray scattering studies with  $H \parallel ab$  are available. The magnitude of  $\rho_{\text{xy}}^{\text{THE}}$  shows a clear dependence on the Ga content, and is almost twice larger in  $\text{EuAl}_4$  than in  $\text{EuGa}_4$ . The  $\rho_{\text{xy}}^{\text{THE}}$  is believed to be determined mostly by the spin polarization, the Hall coefficient, and skyrmion density. Hall-resistivity measurements reveal comparable Hall coefficients in both  $\text{EuAl}_4$  and  $\text{EuGa}_4$ . Considering that both compounds share similar electronic band structures, the spin polarization should be comparable as well. Therefore, the difference in  $\rho_{\text{xy}}^{\text{THE}}$  should most likely come from a different skyrmion density. To confirm this, further investigations in determining the skyrmion lattice in  $\text{Eu}(\text{Al}_{1-x}\text{Ga}_x)_4$  are crucial. For instance, one can use real-space imaging techniques, including the Lorentz transmission electron microscopy, or the magnetic force microscopy to estimate the skyrmion density.

According to recent REXS and CD XSMS studies

(section 4), magnetic helix structures form in both phase-III ( $T_{\text{N}2} < T < T_{\text{N}3}$ ) and phase-IV ( $T < T_{\text{N}4}$ ) in a zero-field condition. However, the chirality of the spin helix is reversed in these phases. In magnetic materials, the observed THE is mostly related to a Berry-phase accumulation in real space due to chiral spin textures. When passing through chiral spin textures, charge carriers pick up an additional Berry phase and experience a local emergent magnetic field  $B_{\text{eff}}$  that is proportional to the scalar spin chirality. As a consequence, the sign of  $\rho_{\text{xy}}^{\text{THE}}$  is determined by  $B_{\text{eff}}$  and, thus, by the spin chirality. In principle, the reversal of spin chirality in  $\text{EuAl}_4$  would lead to a sign change in  $\rho_{\text{xy}}^{\text{THE}}(H)$ . Yet, according to Hall-resistivity measurements, the  $\rho_{\text{xy}}^{\text{THE}}$  of  $\text{EuAl}_4$  is always positive (section 3) in the studied temperature- and field range, for both  $H \parallel ab$  and  $H \parallel c$ . Such an observation might suggest that the external magnetic field can define the spin chirality of the magnetic helix structure in  $\text{EuAl}_4$ . It could be interesting to extend the REXS measurements to higher magnetic fields and check the spin chirality. Considering an  $\text{EuGa}_4$  single crystal, if  $\rho_{\text{xy}}^{\text{THE}}$  can be isolated from the measured  $\rho_{\text{xy}}(H)$  for  $H \parallel ab$ , its sign should be opposite to that of  $\rho_{\text{xy}}^{\text{THE}}$  for  $H \parallel c$ . Therefore, the identification of spin textures in  $\text{EuGa}_4$  in an applied magnetic field (currently still missing) is also highly desirable.

The synchrotron x-ray diffraction and optical spectroscopy reveal a sizable coupling among the lattice, magnetic order, and charge order in  $\text{Eu}(\text{Al,Ga})_4$ . It undergoes a tetragonal-to-orthorhombic distortion at  $T_{\text{N}3} \sim 12.6$  K, where the magnetic structure of  $\text{EuAl}_4$  changes significantly, from a SDW to a helix structure. At  $T < T_{\text{N}3}$ , the unit cell is compressed and elongated along the  $a$ - and  $b$ -axis, respectively. As a consequence, the magnetic modulation vectors are parallel to the elongated  $b$ -axis, implying sizable magnetostriction and magnetovolume effects in  $\text{EuAl}_4$ , confirmed by field-dependent thermal-expansion measurements. The skyrmion phases, too, are found to possess an orthorhombic structural distortion within the  $ab$  plane. On the other hand, the incommensurate wave vector of CDW order  $\mathbf{q}_{\text{CDW}} = (0,0,\delta)$ , appears below  $T_{\text{CDW}} = 145$  K. The  $\delta$  value decreases monotonically with decreasing temperature, from  $T_{\text{CDW}}$  to  $T_{\text{N}}$ . Since it exhibits distinct anomalies at  $T_{\text{N}s}$ , this implies an interplay between the magnetic- and charge order in  $\text{EuAl}_4$ . The REXS data also reveal that, in  $\text{EuAl}_2\text{Ga}_2$ , the intensity of the CDW order is significantly reduced below  $T_{\text{N}1}$ . Thus, the formation of the AFM order suppresses the CDW order, demonstrating a strong interplay and competition between these electronic orders in  $\text{Eu}(\text{Al,Ga})_4$ . Optical spectroscopy found that the CDW gap is partially opened on the Fermi surface, the AFM interactions mediated by the itinerant electrons should be anisotropic. In such an anisotropic environment, it is possible for itinerant electrons from the Weyl bands to mediate the anisotropic magnetic interactions that facilitate the formation of the

chiral spin textures. All these observations imply couplings between the lattice-, charge-, and magnetic orders in the  $\text{Eu}(\text{Al,Ga})_4$  family. However, the evolution of topological spin textures with structural distortion or charge order is not yet well understood, requiring further investigations.

To conclude, recent experimental and theoretical studies of the  $\text{Eu}(\text{Al,Ga})_4$  family, establish it as a suitable platform to explore the interplay between the lattice-, charge-, and spin degrees of freedom, and the associated emergent phenomena. Such interplay seems to underlie the structural and electronic instabilities occurring in this family of compounds and yields a rich variety of topological spin textures, as well as the potential to control the skyrmion phases and topological transport properties by uniaxial stress or pressure, epitaxial strain, electric and magnetic fields. These numerous appealing possibilities are open to future investigation.

## 10. Acknowledgements

We thank Junzhang Ma and Sailong Ju for fruitful discussions. This work was supported by the National Natural Science foundation of China (NSFC) (Grant Nos. 12374105, 12274125, 12174103, 11874150, and 12350710785), the Natural Science Foundation of Shanghai (Grant Nos. 21ZR1420500 and 21JC1402300), the Natural Science Foundation of Chongqing (Grant No.2022NSCQ-MSX1468), and the Fundamental Research Funds for the Central Universities. This work was also financially supported by the Schweizerische Nationalfonds zur Förderung der Wissenschaftlichen Forschung (SNF) (Grant Nos. 200021\_188706 and 206021\_139082).

## 11. References

- [1] Yan B and Zhang S C 2012 *Rep. Prog. Phys.* **75** 096501
- [2] Lv B Q, Qian T and Ding H 2021 *Rev. Mod. Phys.* **93**(2) 025002
- [3] Bernevig B A, Felser C and Beidenkopf H 2022 *Nature* **603** 41–51
- [4] Bonbien V, Zhuo F, Salimath A, Ly O, Abbout A and Manchon A 2022 *J. Phys. D: Appl. Phys.* **55** 103002
- [5] Šmejkal L, MacDonald A H, Sinova J, Nakatsuji S and Jungwirth T 2022 *Nat. Rev. Mater.* **7** 482–496
- [6] Yan B and Felser C 2017 *Annu. Rev. Condens. Matter Phys.* **8** 337–354
- [7] Wang S, Lin B C, Wang A Q, Yu D P and Liao Z M 2017 *Adv. Phys. X* **2** 518–544
- [8] Armitage N P, Mele E J and Vishwanath A 2018 *Rev. Mod. Phys.* **90**(1) 015001
- [9] Liu D F, Liang A J, Liu E K, Xu Q N, Li Y W, Chen C, Pei D, Shi W J, Mo S K, Dudin P, Kim T, Cacho C, Li G, Sun Y, Yang L X, Liu Z K, Parkin S S P, Felser C and Chen Y L 2019 *Science* **365** 1282–1285
- [10] Ma J Z, Nie S M, Yi C J, Jandke J, Shang T, Yao M Y, Naamneh M, Yan L Q, Sun Y, Chikina A, Strocov V N, Medarde M, Song M, Xiong Y M, Xu G, Wulfthekel W, Mesot J, Reticcioli M, Franchini C, Mudry C, Müller M, Shi Y G, Qian T, Ding H and Shi M 2019 *Sci. Adv.* **5** eaaw4718
- [11] Xu Y, Das L, Ma J Z, Yi C J, Nie S M, Shi Y G, Tiwari A, Tsirkin S S, Neupert T, Medarde M, Shi M, Chang J and Shang T 2021 *Phys. Rev. Lett.* **126**(7) 076602

- [12] Suzuki T, Chisnell R, Devarakonda A, Liu Y T, Feng W, Xiao D, Lynn J and Checkelsky J 2016 *Nat. Phys.* **12** 1119–1123
- [13] Chen H, Niu Q and MacDonald A H 2014 *Phys. Rev. Lett.* **112**(1) 017205
- [14] Nakatsuji S, Kiyohara N and Higo T 2015 *Nature* **527** 212–215
- [15] Sinova J, Valenzuela S O, Wunderlich J, Back C H and Jungwirth T 2015 *Rev. Mod. Phys.* **87** 1213
- [16] Nagaosa N, Sinova J, Onoda S, MacDonald A H and Ong N P 2010 *Rev. Mod. Phys.* **82** 1539
- [17] Fert A, Reyren N and Cros V 2017 *Nat. Rev. Mater.* **2** 17031
- [18] Puphal P, Pomjakushin V, Kanazawa N, Ukleev V, Gawryluk D J, Ma J, Naamneh M, Plumb N C, Keller L, Cubitt R, Pomjakushina E and White J S 2020 *Phys. Rev. Lett.* **124** 017202
- [19] Ueda K, Yu T, Hirayama M, Kurokawa R, Nakajima T, Saito H, Kriener M, Hoshino M, Hashizume D, Arima T h, Arita R and Tokura Y 2023 *Nat. Commun.* **14** 6339
- [20] Fujishiro Y, Kanazawa N, Nakajima T, Yu X Z, Ohishi K, Kawamura Y, Kakurai K, Arima T, Mitamura H, Miyake A, Akiba K, Tokunaga M, Matsuo A, Kindo K, Koretsune T, Arita R and Tokura Y 2019 *Nat. Commun.* **10** 1059
- [21] Piva M M, Souza J C, Lombardi G A, Pakuszewski K R, Adriano C, Pagliuso P G and Nicklas M 2023 *Phys. Rev. Mater.* **7** 074204
- [22] Sun Z L, Peng K L, Cui J H, Zhu C S, Zhuo W Z, Wang Z Y and Chen X H 2021 *Phys. Rev. B* **103** 085116
- [23] Ohtsuki T, Tian Z, Endo A, Halim M, Katsumoto S, Kohama Y, Kindo K, Lippmaa M and Nakatsuji S 2019 *Proc. Natl. Acad. Sci.* **116** 8803–8808
- [24] Fert A, Cros V and Sampaio J a 2013 *Nat. Nanotechnol.* **8** 152–156
- [25] Nagaosa N and Tokura Y 2013 *Nat. Nanotechnol.* **8** 899
- [26] Mühlbauer S, Binz B, Jonietz F, Pfleiderer C, Rosch A, Neubauer A, Georgii R and Böni P 2009 *Science* **323** 915
- [27] Yu X Z, Kanazawa N, Onose Y, Kimoto K, Zhang W Z, Ishiwata S, Matsui Y and Tokura Y 2011 *Nat. Mater.* **10** 106
- [28] Yu X Z, Onose Y, Kanazawa N, Park J H, Han J H, Matsui Y, Nagaosa N and Tokura Y 2010 *Nature* **465** 901
- [29] Seki S, Yu X Z, Ishiwata S and Tokura Y 2012 *Science* **336** 198
- [30] Kézsmárki I, Bordács S, Milde P, Neuber E, Eng L M, White J S, Rønnow H M, Dewhurst C D, Mochizuki M, Yanai K, Nakamura H, Ehlers D, Tsurkan V and Loidl A 2015 *Nat. Mater.* **14** 1116
- [31] Tokunaga Y, Yu X Z, White J S, Rønnow H M, Morikawa D, Taguchi Y and Tokura Y 2015 *Nat. Commun.* **6** 7638
- [32] Kurumaji T, Nakajima T, Hirschberger M, Kikkawa A, Yamasaki Y, Sagayama H, Nakao H, Taguchi Y, Arima T h and Tokura Y 2019 *Science* **365** 914
- [33] Hirschberger M, Nakajima T, Gao S, Peng L, Kikkawa A, Kurumaji T, Kriener M, Yamasaki Y, Sagayama H, Nakao H, Ohishi K, Kakurai K, Taguchi Y, Yu X, Arima T and Tokura Y 2019 *Nat. Commun.* **10** 5831
- [34] Khanh N D, Nakajima T, Yu X, Gao S, Shibata K, Hirschberger M, Yamasaki Y, Sagayama H, Nakao H, Peng L, Nakajima K, Takagi R, Arima T, Tokura Y and Seki S 2020 *Nat. Nanotechnol.* **15** 444
- [35] Li H, Ding B, Chen J, Li Z, Hou Z, Liu E, Zhang H, Xi X, Wu G and Wang W 2019 *Appl. Phys. Lett.* **114** 192408
- [36] Batista C D, Lin S Z, Hayami S and Kamiya Y 2016 *Rep. Prog. Phys.* **79** 084504
- [37] Heinze S, von Bergmann K, Menzel M, Brede J, Kubetzka A, Wiesendanger R, Bihlmayer G and Blügel S 2011 *Nat. Phys.* **7** 713–718
- [38] Ozawa R, Hayami S and Motome Y 2017 *Phys. Rev. Lett.* **118**(14) 147205
- [39] Ukleev V, Karube K, Derlet P M, Wang C N, Luetkens H, Morikawa D, Kikkawa A, Mangin-Thro L, Wildes A R, Yamasaki Y, Yokoyama Y, Yu L, Piamonteze C, Jaouen N, Tokunaga Y, Rønnow H M, Arima T, Tokura Y, Taguchi Y and White J S 2021 *npj Quantum Mater.* **6** 40
- [40] Göbel B, Mertig I and Tretiakov O A 2021 *Physics Reports* **895** 1–28
- [41] Kanazawa N, Nii Y, Zhang X X, Mishchenko A S, De Philippis G, Kagawa F, Iwasa Y, Nagaosa N and Tokura Y 2016 *Nat. Commun.* **7** 11622
- [42] Göbel B, Akosa C A, Tataro G and Mertig I 2020 *Phys. Rev. Research* **2** 013315
- [43] Vistoli L, Wang W, Sander A, Zhu Q, Casals B, Cicheler R, Barthélémy A, Fusil S, Herranz G, Valencia S, Abrudan R, Weschke E, Nakazawa K, Kohno H, Santamaria J, Wu W, Garcia V and Bibes M 2019 *Nat. Phys.* **15** 67
- [44] Singh D, Fujishiro Y, Hayami S, Moody S H, Nomoto T, Baral P R, Ukleev V, Cubitt R, Steinke N J, Gawryluk D J, Pomjakushina E, Ōnuki Y, Arita R, Tokura Y, Kanazawa N and White J S 2023 *Nature Communications* **14** 8050
- [45] Wu M, Yang R, Zhu X, Ren Y, Qian A, Xie Y, Yue C, Nie Y, Yuan X, Wang N, Tu D, Li D, Han Y, Wang Z, Dai Y, Zheng G, Zhou J, Ning W, Qiu X and Tian M 2023 Surface skyrmions and dual topological Hall effect in antiferromagnetic topological insulator  $\text{EuCd}_2\text{As}_2$  arXiv:2311.15835 [cond-mat]
- [46] Chakrabarty D, Jamaluddin S, Manna S K and Nayak A K 2022 *Commun. Phys.* **5** 189
- [47] Shang T, Xu Y, Gawryluk D J, Ma J Z, Shiroka T, Shi M and Pomjakushina E 2021 *Phys. Rev. B* **103** L020405
- [48] Takagi R, Matsuyama N, Ukleev V, Yu L, White J S, Francoual S, Mardegan J R L, Hayami S, Saito H, Kaneko K, Ohishi K, Ōnuki Y, Arima T h, Tokura Y, Nakajima T and Seki S 2022 *Nat. Commun.* **13** 1472
- [49] Paddison J A M, Rai B K, May A F, Calder S, Stone M B, Frontzek M D and Christianson A D 2022 *Phys. Rev. Lett.* **129**(13) 137202
- [50] Zhu X Y, Zhang H, Gawryluk D J, Zhen Z X, Yu B C, Ju S L, Xie W, Jiang D M, Cheng W J, Xu Y, Shi M, Pomjakushina E, Zhan Q F, Shiroka T and Shang T 2022 *Phys. Rev. B* **105**(1) 014423
- [51] Yu X Z, Tokunaga Y, Kaneko Y, Zhang W Z, Kimoto K, Matsui Y, Taguchi Y and Tokura Y 2014 *Nat. Commun.* **5** 3198
- [52] Onoda M, Tataro G and Nagaosa N 2004 *J. Phys. Soc. Jpn.* **73** 2624
- [53] Liang T, Gibson Q, Ali M N, Liu M, Cava R J and Ong N P 2015 *Nat. Mater.* **14** 280
- [54] Liang T, Lin J, Gibson Q, Gao T, Hirschberger M, Liu M, Cava R J and Ong N P 2017 *Phys. Rev. Lett.* **118** 136601
- [55] Liang T, Lin J, Gibson Q, Kushwaha S, Liu M, Wang W, Xiong H, Sobota J A, Hashimoto M, Kirchmann P S, Shen Z X, Cava R J and Ong N P 2018 *Nat. Phys.* **14** 451
- [56] Ikhlas M, Tomita T, Koretsune T, Suzuki M T, Nishio-Hamane D, Arita R, Otani Y and Nakatsuji S 2017 *Nat. Phys.* **13** 1085
- [57] Nayak A K, Fischer J E, Sun Y, Yan B, Karel J, Komarek A C, Shekhar C, Kumar N, Schnelle W, Kübler J, Felser C and Parkin S S P 2016 *Sci. Adv.* **2** e1501870
- [58] Cagliaris F, Wuttke C, Sykora S, Süß V, Shekhar C, Felser C, Büchner B and Hess C 2018 *Phys. Rev. B* **98** 201107(R)
- [59] Watzman S J, McCormick T M, Shekhar C, Wu S C, Sun Y, Prakash A, Felser C, Trivedi N and Heremans J P 2018 *Phys. Rev. B* **97** 161404(R)
- [60] Šmejkal L, Sinova J and Jungwirth T 2022 *Phys. Rev. X* **12**(4) 040501
- [61] Mazin I (The PRX Editors) 2022 *Phys. Rev. X* **12**(4) 040002
- [62] Gonzalez Betancourt R D, Zubáč J, Gonzalez-Hernandez R, Geishendorf K, Šobán Z, Springholz G, Olejník K, Šmejkal L, Sinova J, Jungwirth T, Goennenwein S T B, Thomas A, Reichlová H, Šelezný J and Kriegner D 2023 *Phys. Rev. Lett.* **130** 036702
- [63] Feng Z, Zhou X, Šmejkal L, Wu L, Zhu Z, Guo H, González-Hernández R, Wang X, Yan H, Qin P, Zhang X, Wu H, Chen H, Meng Z, Liu L, Xia Z, Sinova J, Jungwirth T and Liu Z 2022 *Nat. Electron.* **5** 735–743
- [64] Neubauer A, Pfleiderer C, Binz B, Rosch A, Ritz R, Niklowitz P G and Böni P 2009 *Phys. Rev. Lett.* **102** 186602
- [65] Raju M, Yagil A, Soumyanarayanan A, Tan A K C, Almoalem A, Ma F, Auslaender O M and Panagopoulos C 2019 *Nat. Commun.* **10** 696
- [66] Grenz J, Köhler A, Schwarz A and Wiesendanger R 2017 *Phys. Rev. Lett.* **119**(4) 047205

- [67] Woo S, Litzius K, Krüger B, Im M Y, Caretta L, Richter K, Mann M, Krone A, Reeve R M, Weigand M, Agrawal P, Lemesh I, Mawass M A, Fischer P, Kläui M and Beach G S D 2016 *Nat. Mater.* **15** 501–506
- [68] Soumyanarayanan A, Raju M, Gonzalez Oyarce A L, Tan A K C, Im M Y, Petrović A, Ho P, Khoo K H, Tran M, Gan C K, Ernult F and Panagopoulos C 2017 *Nat. Mater.* **16** 898–904
- [69] Chen G, Ma T, N'Diaye A T, Kwon H, Won C, Wu Y and Schmid A K 2013 *Nat. Commun.* **4** 2671
- [70] Romming N, Hanneken C, Menzel M, Bickel J E, Wolter B, Von Bergmann K, Kubetzka A and Wiesendanger R 2013 *Science* **341** 636–639
- [71] Wang K, Mori R, Wang Z, Wang L, Ma J H S, Latzke D W, Graf D E, Denlinger J D, Campbell D, Bernevig B A, Lanzara A and Paglione J 2021 *npj Quantum Mater.* **6** 28
- [72] Nakamura A, Uejo T, Harima H, Araki S, Kobayashi T C, Nakashima M, Amako Y, Hedo M, Nakama T and Ōnuki Y 2016 *J. Alloys Compd.* **654** 290
- [73] Lei S, Allen K, Huang J, Moya J M, Wu T C, Casas B, Zhang Y, Oh J S, Hashimoto M, Lu D, Denlinger J, Jozwiak C, Bostwick A, Rotenberg E, Balicas L, Birgeneau R, Foster M S, Yi M, Sun Y and Morosan E 2023 *Nat. Commun.* **14** 5812
- [74] Araki S, Ikeda Y, Kobayashi T C, Nakamura S, Hiranaka Y, Hedo M, Nakama T and Ōnuki Y 2014 *J. Phys. Soc. Jpn.* **83** 015001
- [75] Nakamura A, Hiranaka Y, Hedo M, Nakama T, Miura Y, Tsutsumi H, Mori A, Ishida K, Mitamura K, Hirose Y, Sugiyama K, Honda F, Takeuchi T, Matsuda T D, Yamamoto E, Haga Y and Ōnuki Y 2014 *JPS Conf. Proc.* **3** 011012
- [76] Nakamura A, Uejo T, Honda F, Takeuchi T, Harima H, Yamamoto E, Haga Y, Matsubayashi K, Uwatoko Y, Hedo M, Nakama T and Ōnuki Y 2015 *J. Phys. Soc. Jpn.* **84** 124711
- [77] Shimomura S, Murao H, Tsutsui S, Nakao H, Nakamura A, Hedo M, Nakama T and Ōnuki Y 2019 *J. Phys. Soc. Jpn.* **88** 014602
- [78] Kobata M, Fujimori S, Takeda Y, Okane T, Saitoh Y, Kobayashi K, Yamagami H, Nakamura A, Hedo M, Nakama T and Ōnuki Y 2016 *J. Phys. Soc. Jpn.* **85** 094703
- [79] Nakamura A, Hiranaka Y, Hedo M, Nakama T, Miura Y, Tsutsumi H, Mori A, Ishida K, Mitamura K, Hirose Y, Sugiyama K, Honda F, Settai R, Takeuchi T, Hagiwara M, D Matsuda T, Yamamoto E, Haga Y, Matsubayashi K, Uwatoko Y, Harima H and Ōnuki Y 2013 *J. Phys. Soc. Jpn.* **82** 104703
- [80] Zhang J and Bobev S 2013 *J. Solid State Chem.* **205** 21–28
- [81] Bruzzone G 1965 *Acta Cryst.* **18** 1081–1082
- [82] Bruzzone G and Merlo F 1975 *J. less-common met.* **39** 1–6
- [83] Zogg H and Schwellinger P 1979 *J. Mater. Sci.* **14** 1923–1932
- [84] De Mooij D B and Buschow K H J 1985 *J. less-common met.* **109** 117–122
- [85] Tobash P H, Yamasaki Y and Bobev S 2005 *Acta Cryst.* **E61** i174–i176
- [86] Zevalkink A, Bobnar M, Schwarz U and Grin Y 2017 *Chem. Mater.* **29** 1236–1244
- [87] Miller G J, Li F and Franzen H F 1993 *J. Am. Chem. Soc.* **115** 3739–3745
- [88] Verbovetskyy Y, Kaczorowski D and Gonçalves A 2011 *Intermetallics* **19** 613–620
- [89] Stavinoha M, Cooley J A, Minasian S G, McQueen T M, Kauzlarich S M, Huang C L and Morosan E 2018 *Phys. Rev. B* **97** 195146
- [90] Tobash P H and Bobev S 2006 *J. Alloys Compd.* **418** 58–62
- [91] Grytsiv A, Kaczorowski D, Leithe-Jasper A, Rogl P, Godart C, Potel M and Noël H 2002 *J. Solid State Chem.* **163** 37–43
- [92] Dhar S, Paulose P, Kulkarni R, Manfrinetti P, Pani M and Parodi N 2009 *Solid State Commun.* **149** 68–72
- [93] Schobinger-Papamantellos P and Hulliger F 1989 *J. less-common met.* **146** 327–335
- [94] Lai Y, Chan J Y and Baumbach R E 2022 *Sci. Adv.* **8** eabp8264
- [95] Pfeleiderer C 2009 *Rev. Mod. Phys.* **81** 1551–1624
- [96] Brando M, Belitz D, Grosche F and Kirkpatrick T 2016 *Rev. Mod. Phys.* **88** 025006
- [97] Löhneysen H V, Rosch A, Vojta M and Wölfle P 2007 *Rev. Mod. Phys.* **79** 1015–1075
- [98] Stewart G R 2011 *Rev. Mod. Phys.* **83** 1589–1652
- [99] Shatruk M 2019 *J. Solid State Chem.* **272** 198–209
- [100] Szytuła A and Leciejewicz J 1989 *Magnetic properties of ternary intermetallic compounds of the  $\text{RT}_2\text{X}_2$  type* vol 12 (Elsevier)
- [101] Yi E, Zheng D F, Pan F, Zhang H, Wang B, Chen B, Wu D, Liang H, Mei Z X, Wu H, Yang S A, Cheng P, Wang M and Shen B 2023 *Phys. Rev. B* **107** 035142
- [102] Wang Z, Rogers J D, Yao X, Nichols R, Atay K, Xu B, Franklin J, Sochnikov I, Ryan P J, Haskel D and Tafti F 2021 *Adv. Mater.* **33** 2005755
- [103] Ramakrishnan S, Kotla S R, Pi H, Maity B B, Chen J, Bao J K, Guo Z, Kado M, Agarwal H, Eisele C, Nohara M, Noohinejad L, Weng H, Ramakrishnan S, Thamizhavel A and van Smaalen S 2023 *arXiv:2309.08959*
- [104] Kaneko K, Kawasaki T, Nakamura A, Munakata K, Nakao A, Hanashima T, Kiyonagi R, Ohhara T, Hedo M, Nakama T and Ōnuki Y 2021 *J. Phys. Soc. Jpn.* **90** 064704
- [105] Ramakrishnan S, Kotla S R, Rekis T, Bao J K, Eisele C, Noohinejad L, Tolkiehn M, Paulmann C, Singh B, Verma R, Bag B, Kulkarni R, Thamizhavel A, Singh B, Ramakrishnan S and Van Smaalen S 2022 *IUCrJ* **9** 378–385
- [106] Korshunov A N, Sukhanov A S, Gebel S, Pavlovskii M S, Andriushin N D, Gao Y, Moya J M, Morosan E and Rahn M C 2024 Phonon softening and atomic modulations in  $\text{EuAl}_4$  *arXiv:2402.15397 [cond-mat]*
- [107] Grüner G 2018 *Density Waves in Solids* 1st ed (CRC Press)
- [108] Johannes M D and Mazin I I 2008 *Phys. Rev. B* **77**(16) 165135
- [109] Zhu X, Cao Y, Zhang J, Plummer E W and Guo J 2015 *Proceedings of the National Academy of Sciences* **112** 2367–2371
- [110] Zhu X, Guo J, Zhang J and Plummer E W 2017 *Advances in Physics: X* **2** 622–640
- [111] Zhang H, Zhu X Y, Xu Y, Gawryluk D J, Xie W, Ju S L, Shi M, Shiroka T, Zhan Q F, Pomjakushina E and Shang T 2022 *J. Phys. Condens. Matter* **34** 034005
- [112] Moya J M, Huang J, Lei S, Allen K, Gao Y, Sun Y, Yi M and Morosan E 2023 *Phys. Rev. B* **108**(6) 064436
- [113] Meier W R, Torres J R, Hermann R P, Zhao J, Lavina B, Sales B C and May A F 2022 *Phys. Rev. B* **106**(9) 094421
- [114] Leahy I A, Lin Y P, Siegfried P E, Treglia A C, Song J C W, Nandkishore R M and Lee M 2018 *Proc. Natl. Acad. Sci. U.S.A.* **115** 10570 and the references therein
- [115] Gayles J, Freimuth F, Schena T, Lani G, Mavropoulos P, Duine R A, Blügel S, Sinova J and Mokrousov Y 2015 *Phys. Rev. Lett.* **115** 036602
- [116] Kanazawa N, Onose Y, Arima T, Okuyama D, Ohoyama K, Wakimoto S, Kakurai K, Ishiwata S and Tokura Y 2011 *Phys. Rev. Lett.* **106** 156603
- [117] Franz C, Freimuth F, Bauer A, Ritz R, Schnarr C, Duvinage C, Adams T, Blügel S, Rosch A, Mokrousov Y and Pfeleiderer C 2014 *Phys. Rev. Lett.* **112** 186601
- [118] Schulz T, Ritz R, Bauer A, Halder M, Wagner M, Franz C, Pfeleiderer C, Everschor K, Garst M and Rosch A 2012 *Nat. Phys.* **8** 301
- [119] Qin Q, Liu L, Lin W, Shu X, Xie Q, Lim Z, Li C, He S, Chow G M and Chen J 2019 *Adv. Mater.* **31** 1807008
- [120] Matsuno J, Ogawa N, Yasuda K, Kagawa F, Koshibae W, Nagaosa N, Tokura Y and Kawasaki M 2016 *Sci. Adv.* **2** e1600304
- [121] Liu E, Sun Y, Kumar N, Muechler L, Sun A, Jiao L, Yang S Y, Liu D, Liang A, Xu Q, Kroder J, Süß, Borrmann H, Shekhar C, Wang Z, Xi C, Wang W, Schnelle W, Wirth S, Chen Y, Goennenwein S T B and Felser C 2018 *Nat. Phys.* **14** 1125
- [122] Manna K, Muechler L, Kao T H, Stinshoff R, Zhang Y, Gooth J, Kumar N, Kreiner G, Koepernik K, Car R, Kübler J, Fecher G H, Shekhar C, Sun Y and Felser C 2018 *Phys. Rev. X* **8**(4) 041045
- [123] Hayami S 2022 *J. Phys. Soc. Jpn.* **91** 023705
- [124] Lux F R, Freimuth F, Blügel S and Mokrousov Y 2020 *Phys. Rev. Lett.* **124**(9) 096602
- [125] Moya J M, Lei S, Clements E M, Kengle C S, Sun S, Allen K, Li Q, Peng Y Y, Husain A A, Mitrano M, Krogstad M J, Osborn R, Puthirath A B, Chi S, Debeer-Schmitt L, Gaudet J, Abbamonte P, Lynn J W and Morosan E 2022 *Phys. Rev. Mater.* **6** 074201



- [126] Kawasaki T, Kaneko K, Nakamura A, Aso N, Hedo M, Nakama T, Ohhara T, Kiyonagi R, Oikawa K, Tamura I, Nakao A, Munakata K, Hanashima T and Ōnuki Y 2016 *J. Phys. Soc. Jpn.* **85** 114711
- [127] Wang S, Luo Q, Luo X, Ma S, Chen C, Gao F, Lv B, Zhong R, Ren W and Zhong Z 2023 *J. Alloys Compd.* **968** 171977
- [128] Vibhakara M, Khalyavin D D, Orlandi F, Moya J M, Lei S, Morosan E and Bombardi A 2024 Spontaneous spin chirality reversal and competing phases in the topological magnet  $\text{EuAl}_4$  arXiv:2403.10159 [cond-mat]
- [129] Miao H, Bouaziz J, Fabbris G, Meier W R, Yang F Z, Li H X, Nelson C, Vescovo E, Zhang S, Christianson A D, Lee H N, Zhang Y, Batista C D and Blügel S 2024 *Phys. Rev. X* **14**(1) 011053
- [130] Gen M, Takagi R, Watanabe Y, Kitou S, Sagayama H, Matsuyama N, Kohama Y, Ikeda A, Ōnuki Y, Kurumaji T, Arima T h and Seki S 2023 *Phys. Rev. B* **107**(2) L020410
- [131] Vibhakara M, Khalyavin D D, Moya J M, Manuel P, Orlandi F, Lei S, Morosan E and Bombardi A 2023 *Phys. Rev. B* **108**(10) L100404
- [132] Lee S L, Kilcoyne S H and Cywinski R (eds) 1999 *Muon Science: Muons in Physics, Chemistry and Materials* (Bristol: IOP Publishing)
- [133] Yaouanc A and de Réotier P D 2011 *Muon Spin Rotation, Relaxation, and Resonance: Applications to Condensed Matter* (Oxford: Oxford University Press)
- [134] Blundell S J, De Renzi R, Lancaster T and Pratt F L (eds) 2021 *Muon Spectroscopy: An Introduction* (Oxford: Oxford University Press)
- [135] Amato A and Morenzoni E 2024 *Introduction to Muon Spin Spectroscopy: Applications to Solid State and Material Sciences* (Cham: Springer)
- [136] Amato A 1997 *Rev. Mod. Phys.* **69**(4) 1119–1180
- [137] Blundell S J 1999 *Contemp. Physics* **40**(3) 175–192
- [138] Nuccio L, Schulz L and Drew A J 2014 *J. Phys. D: Appl. Phys.* **47** 473001
- [139] Hillier A D, Blundell S J, McKenzie I, Umegaki I, Shu L, Wright J A, Prokscha T, Bert F, Shimomura K, Berlie A, Alberto H and Watanabe I 2022 *Nat. Rev. Methods Primers* **2** 4
- [140] Fujita M, Suzuki K M, Asano S, Okabe H, Koda A, Kadono R and Watanabe I 2020 *Phys. Rev. B* **102**(4) 045116
- [141] Franke K J A, Huddart B M, Hicken T J, Xiao F, Blundell S J, Pratt F L, Crisanti M, Barker J A T, Clark S J, Stefancic A, Hatnean M C, Balakrishnan G and Lancaster T 2018 *Phys. Rev. B* **98** 054428
- [142] Hicken T J, Wilson M N, Franke K J A, Huddart B M, Hawkhead Z, Gomilšek M, Clark S J, Pratt F L, Stefancic A, Hall A E, Ciomaga Hatnean M, Balakrishnan G and Lancaster T 2021 *Phys. Rev. B* **103** 024428
- [143] Huddart B M, Hernández-Melián A, Wood G D A, Mayoh D A, Gomilšek M, Guguchia Z, Wang C, Blundell S J, Balakrishnan G and Lancaster T 2024 Field-orientation-dependent magnetic phases in  $\text{GdRu}_2\text{Si}_2$  probed with muon-spin spectroscopy arXiv:2403.09431 [cond-mat]
- [144] Niki H, Nakamura S, Higa N, Kuroshima H, Toji T, Yogi M, Nakamura A, Hedo M, Nakama T, Ōnuki Y and Harima H 2015 *J. Phys.: Conf. Ser.* **592**(1) 012030
- [145] Ruderman M A and Kittel C 1954 *Phys. Rev.* **96**(1) 99–102
- [146] Kasuya T 1956 *Prog. Theor. Phys.* **16**(1) 45–57
- [147] Yosida K 1957 *Phys. Rev.* **106**(5) 893–898
- [148] Villain J, Lavagna M and Bruno P 2016 *C. R. Physique* **17**(3) 276–290
- [149] Van Diepen A M, Buschow K H J and De Wijn H W 1969 *J. Chem. Phys.* **51**(12) 5259–5263
- [150] Narath A 1967 *Phys. Rev.* **162**(2) 320–332
- [151] Niki H, Higa N, Kuroshima H, Toji T, Morishima M, Minei M, Yogi M, Nakamura A, Hedo M, Nakama T, Ōnuki Y and Harima H 2015 *Phys. Procedia* **75** 763–770
- [152] Yogi M, Nakamura S, Higa N, Niki H, Hirose Y, Ōnuki Y and Harima H 2013 *J. Phys. Soc. Jpn.* **82**(10) 103701
- [153] Yang R, Le C C, Zhu P, Wang Z W, Shang T, Dai Y M, Hu J P and Dressel M 2024 *Phys. Rev. B* **109** L041113
- [154] Niki H, Nakamura S, Higa N, Yogi M, Nakamura A, Niki K, Maehira T, Hedo M, Nakama T and Ōnuki Y 2020 *JPS Conf. Proc.* **29** 012007
- [155] Wernick J H, Williams H J and Gossard A C 1967 *J. Phys. Chem. Solids* **28**(2) 271–273
- [156] Taylor R H and Coles B R 1975 *J. Phys. F: Met. Phys.* **5**(1) 121–142
- [157] He Q L, Hughes T L, Armitage N P, Tokura Y and Wang K L 2022 *Nat. Mater.* **21** 15–23
- [158] Dressel M and Grüner G 2002 *Electrodynamics of Solids: Optical Properties of Electrons in Matter* (Cambridge: Cambridge University Press)
- [159] Altman A B, Pemmaraju C D, Alayoglu S, Arnold J, Bauer E D, Booth C H, Fisk Z, Pacold J I, Prendergast D, Shuh D K, Tyliczszak T, Wang J and Minasian S G 2018 *Phys. Rev. B* **97** 045110
- [160] Wan X, Dong J and Savrasov S Y 2011 *Phys. Rev. B* **83** 205201
- [161] Niki H, Nakamura S, Higa N, Kuroshima H, Toji T, Yogi M, Nakamura A, Hedo M, Nakama T, Ōnuki Y and Harima H 2015 *J. Phys.: Conf. Ser.* **592** 012030
- [162] Ni H, Meier W R, Miao H, May A J, Sales B C, Zuo J m and Chi M 2023 Real-space Visualization of Charge Density Wave Induced Local Inversion-Symmetry Breaking in a Skyrmion Magnet arXiv:2311.17682 [cond-mat]
- [163] Ma J, Wang H, Nie S, Yi C, Xu Y, Li H, Jandke J, Wulfnegel W, Huang Y, West D, Richard P, Chikina A, Strocov V N, Mesot J, Weng H, Zhang S, Shi Y, Qian T, Shi M and Ding H 2020 *Adv. Mater.* **32** e1907565
- [164] Wang L L, Nepal N K and Canfield P C 2023 arXiv:2306.15068
- [165] Gaudet J, Yang H Y, Baidya S, Lu B, Xu G, Zhao Y, Rodriguez-Rivera J A, Hoffmann C M, Graf D E, Torchinsky D H, Nikolić P, Vanderbilt D, Tafti F and Broholm C L 2021 *Nat. Mater.* **20** 1650–1656